UC Santa Barbara

UC Santa Barbara Electronic Theses and Dissertations

Title

Hydrodynamics on Smooth 2-Manifolds with Spherical Topology

Permalink

https://escholarship.org/uc/item/13m2m21j

Author

Gross, Ben Jeffrey

Publication Date

2019

Peer reviewed|Thesis/dissertation

eScholarship.org Powered by the California Digital Library
University of California

UNIVERSITY OF CALIFORNIA
Santa Barbara

Hydrodynamics on Smooth 2-Manifolds with Spherical Topology

A Dissertation submitted in partial satisfaction
of the requirements for the degree of

Doctor of Philosophy

in

Mathematics

by

Ben Jeffrey Gross

Committee in Charge:

Professor Paul J. Atzberger, Chair

Professor Kenneth Millett

Professor Mihai Putinar

Professor Otger Campàs

June 2019

The Dissertation of
Ben Jeffrey Gross is approved:

Professor Kenneth Millett

Professor Mihai Putinar

Professor Otger Campàs

Professor Paul J. Atzberger, Committee Chairperson

June 2019

Hydrodynamics on Smooth 2-Manifolds with Spherical Topology

Copyright © 2019

by

Ben Jeffrey Gross

To my parents, who impressed upon me both the value of education, and the importance of constantly learning new things ...

Acknowledgements

I would like to thank all of my friends and family who have been supportive of me throughout the years.

Also I would like to thank my advisor Paul J. Atzberger, for always being patient, generous with his time and knowledge, and his encouragement throughout.

Additionally I would like to thank Nat Trask and Paul Kuberry for all the help they provided me with the Compadre code and getting up to speed on GMLS.

I would also like to acknowledge the financial support that I have received through Paul J. Atzberger's research grants, and from the Kozato family.

Curriculum Vitae

Ben Jeffrey Gross

EDUCATION

Ph.D. Mathematics	University of California, Santa Barbara • Advisor: Paul J. Atzberger	2019
M.A. Mathematics	University of California, Santa Barbara	2015
B.S. Mathematics	Harvey Mudd College	2013

PUBLICATIONS

- *Meshfree Methods on Manifolds for Hydrodynamic Flows on Curved Surfaces: A Generalized Moving Least-Squares (GMLS) Approach*, B. J. Gross, N. Trask, P. Kuberry, and P. J. Atzberger, arXiv:1905.10469, May 2019.

- *Hydrodynamic flows on curved surfaces: Spectral numerical methods for radial manifold shapes*. B. J. Gross and P. J. Atzberger. Journal of Computational Physics, Volume 371, Pages 663-689. October, 2018.

- *Spectral Numerical Exterior Calculus Methods for Differential Equations on Radial Manifolds*. Atzberger, P. J. and Gross, B. Journal of Scientific Computing, Online, doi.org/10.1007/s10915-017-0617-2. December, 2017.

- *Stochastic Service Systems, Random Interval Graphs and Search Algorithms*. Eschenfeldt, P., Gross, B., and Pippenger, N. Random Structures & Algorithms, Volume 45, Issue 3, pp. 421–442. October, 2014.

- *Automated Cell Detection and Morphometry on Growth Plate Images of Mouse Bone*. Ascenzi, M., Du, X., Harding, J. , Beylerian, E. , de Silva, B., Gross, B., Kastein, H., Wang, W., Lyons, K. and Schaeffer, H. Applied Mathematics, Volume 5, Issue 18, pp. 2866-2880. October, 2014.

MINI-SYMPOSIA ORGANIZED

- Machine Learning Approaches for the Sciences and Engineering,
  Society for Industrial and Applied Mathematics (SIAM),
  Conference on Computational Science and Engineering,
  Spokane, WA — February 2019

- Mathematical Challenges in Interfacial Phenomena in Cell Biology,
  Society for Industrial and Applied Mathematics (SIAM),
  Conference on the Life Sciences,
  Minneapolis, MN — August 2018

TALKS & POSTERS PRESENTED

- Meshless Methods for Manifolds: GMLS Approximations of Hydrodynamic Responses in Curved Fluid Interfaces
  Approximation Theory 16
  Nashville, TN — May 2019

- Meshless Methods for Manifolds: Hydrodynamics of Curved Fluid Interfaces and Related Applications
  So Cal Fluids XIII
  UC Santa Barbara — April 2019

- Meshless Methods for Manifolds: Hydrodynamics of Curved Fluid Interfaces and Related Applications
  Society of Industrial and Applied Mathematics (SIAM)
  Conference on Computational Science and Engineering
  Spokane, WA — March 2019

- Fluctuating hydrodynamics for curved fluid interfaces: An Extended Saffman-Delbruck approach for drift-diffusion dynamics of particle inclusions
  American Physical Society (APS)
  71^{st} Annual Meeting of the Division of Fluid Dynamics (DFD)
  Atlanta, GA — November 2018

- Fluctuating Hydrodynamics for Biological Membranes: Role of Curvature in Drift-Diffusion Dynamics
  Society for Industrial and Applied Mathematics (SIAM)
  Conference on the Life Sciences

Minneapolis, MN August 2018

- Protein Transport in Curved Lipid Bilayer Membranes: An Extended Saffman-Delbruck Approach Incorporating Hydrodynamics in Curved Fluid Interfaces, World Congress on Computational Mechanics, New York City, July 2018.

- Fluctuating Hydrodynamic Approaches for Protein Transport in Curved Lipid Bilayer Membranes, Southern California Applied Mathematics Symposium (SOCAMS), UC Santa Barbara, April 2018

- Hydrodynamic flows within curved fluid interfaces: Role of Curvature in the Drift Diffusion Dynamics of Particle Inclusions, So Cal Fluids XII, University of Southern California, April 2018

- Protein Transport in Curved Lipid Bilayer Membranes: An Extended Saffman-Delbruck Approach Incorporating Hydrodynamics in Curvatured Fluid Interfaces
  American Physical Society (APS)
  March Meeting
  Los Angeles, CA March 2018

- Numerical Solutions to Stokes Equations on 2-Manifolds, Society for Industrial and Applied Mathematics (SIAM) Talk Series, UC Santa Barbara, 2017

- Numerical Exterior Calculus Methods for Hydrodynamics Within Curved Fluid Interfaces, Society for Industrial and Applied Mathematics (SIAM) Conference on Applied and Industrial Geometry, Pittsburgh, PA, July 2017

- Particle Dynamics Within Curved Fluid Interfaces and Membranes
  So Cal Fluids XI
  UC San Diego April 2017

- Fluctuating Hydrodynamic Methods for Manifolds: Particle Dynamics Within Curved Fluid Interfaced and Membranes
  Society of Industrial and Applied Mathematics (SIAM)
  Conference on Computational Science and Engineering
  Atlanta, GA February 2017

- Numerical Exterior Calculus Approaches for Hydrodynamics on Curved Surfaces
  Society for Industrial and Applied Mathematics (SIAM)

Conference on the Life Sciences
Boston, MA — July 2016

TEACHING & GRADING

Teaching Assistant at UCSB

- Math 4B, Ordinary Differential Equations — Fall 2015
- Math 104A, Introduction Into Numerical Analysis — Winter 2019
- Math 104B, Numerical Analysis — Spring 2019

Grader at Harvey Mudd College

- Math 55, Discrete Mathematics — Fall 2010
- Math 55, Discrete Mathematics — Spring 2011
- Math 157, Intermediate Probability — Fall 2011
- Math 165, Numerical Analysis — Fall 2012

Abstract

Hydrodynamics on Smooth 2-Manifolds with Spherical Topology

Ben Jeffrey Gross

The investigation of soft materials poses many important challenges having implications for application areas that range from the design of better materials for use in engineering practice to gaining further insights into the functioning of biological organisms. In soft materials there is often an interplay between direct microstructure-level interactions and fluctuations in yielding observed bulk macroscopic material properties. As part of these interactions geometry and hydrodynamic interactions often play a central role. We shall investigate interfacial phenomena associated with soft materials, particularly relevant to the study of lipid bilayer membranes. We shall address the problem of how to formulate and numerically approximate continuum mechanics on 2-manifolds in the case of non-trivial geometries having spherical topology. We shall be particularly interested in developing methods for investigating the case of hydrodynamic flow responses on curved surfaces. We shall present results for an initial model assuming that we have smooth, star-shaped (radial) membrane geometry. We show how spectral methods of approximation can be developed based on use of spherical harmonics expansions, Lebedev quadrature. We use these approaches to investigate how hydrodynamic flow responses depend on the surface geometry. We

find that the surface curvature can significantly effect dissipation rates and augment flow responses. We then develop more general methods for the case of any smooth geometry having spherical topology using numerical approaches based on Generalized Moving Least Squares (GMLS). We use these to further investigate hydrodynamic flows in this setting. We conclude by briefly discussing our current work to extend these numerical approaches to even more general smooth compact manifolds without the need for spherical topology.

Contents

List of Figures **xiv**

1 Introduction **1**
1.1 Problem Motivation 1
1.2 Overview (What we do) 6

2 Using Exterior Calculus Operators to Formulate the Stokes Problem **12**
2.1 Vector and Exterior Calculus on Riemannian Manifolds 13
2.2 Formulating Vector Operators as Exterior Calculus Operators . . 17
2.3 Expressing Exterior Calculus Operators on 2-Manifolds 21
2.4 Continuum Mechanics and Conservation Laws on Manifolds . . . 24
2.5 A Covariant Stokes Equation 30
2.6 Recasting Our Stokes Equation Using the Hodge Decomposition . 33

3 Discretizing Exterior Calculus Operators on Radial Manifolds **37**
3.1 Radial Manifold Differential Geometry 39
3.2 Hyperinterpolation on Radial Manifolds 42
3.2.1 Spherical Harmonic Basis 42
3.2.2 Lebedev Quadratures 44
3.2.3 Hyperinterpolation 46
3.3 Computing Exterior Calculus Operators 48
3.3.1 Computing the Exterior Derivative 48
3.3.2 Computing the Hodge Star 51
3.4 Convergence of our Exterior Calculus Operators 52
3.4.1 Convergence of the Hodge Star 53
3.4.2 Convergence of the Exterior Derivative 55

4 Implementing a Spectrally Accurate Stokes Solver on Radial Manifolds 58
4.1 Inducing an Inner-Product on Radial Manifolds 59
4.2 Validating Our Quadratures on Radial Manifolds 64
4.3 Creating a Stiffness Matrix for the Weak Stokes Equation 68
4.4 Validating Spectral Convergence of our Stokes Solver on Radial Manifolds 75

5 Stokes Responses Under Varying Geometries 81
5.1 Experiments of Stokes Responses on Radial Manifolds 82
5.2 Variational Formulation of Stokes Equation 84
5.3 Dissipation of Stokes Flows Under Varying Geometries 88
5.4 The Role of Rigid-Body Rotations in Stokes Responses 91
5.5 Implications of Our Experiments 97

6 Generalized Moving Least Squares for Discretizing Surface PDEs 99
6.1 Generalized Moving Least Squares (GMLS) 99
6.2 GMLS Reconstruction of Geometries from Point Clouds 104
6.3 Monge Gauge Differential Geometry 109
6.4 GMLS Approximations of Surface Operators 111
6.4.1 GMLS Reconstructions of Our Manifold Geometries 112
6.4.2 GMLS Approximations of Geometry-Dependent Operators 115

7 Convergence of our GMLS Methods 119
7.0.1 Manifold Point Cloud Refinements Used 122
7.1 Optimizing The Stokes Equation for GMLS 123
7.1.1 Biharmonic Formulation of the Hydrodynamics 123
7.1.2 Split Formulation of the Hydrodynamics 124
7.2 Convergence of Surface Operators in GMLS 125
7.2.1 Convergence of Curl Operators in GMLS 131
7.3 Convergence of GMLS Stokes Solvers on Spherical Topologies . . 133

8 Conclusion 142

Bibliography 144

List of Figures

1.1 Radial Manifolds: A radial manifold is defined as a surface where each point can be connected by a line segment to the origin without intersecting the surface. Shown are three radial manifolds which for discussions we refer to interchangeably as the (i) Sphere / Manifold A, (ii) Dimple / Manifold B, and (iii) Fountain / Manifold C. The manifolds are generated (in spherical coordinates) by the radial functions (i) $r(\theta, \phi) = 1.0$, (ii) $r(\theta, \phi) = 1 + r_0 \sin(3\phi)\cos(\theta)$ with $r_0 = 0.4$, and (iii) $r(\theta, \phi) = 1 + r_0 \sin(7\phi)\cos(\theta)$ with $r_0 = 0.4$. The differential geometry of radial manifolds is derived in Section 3.1. 7

2.1 Continuum Mechanics for Manifolds. We consider continuum mechanics formulated within general curved spaces having non-euclidean metric. At each point of the manifold the tangent space $T\mathcal{M}_{\mathbf{x}}$ consists of all vectors tangent to the manifold when thought of as an embedding. The cotangent space $T^*\mathcal{M}_{\mathbf{x}}$ consists of all linear functionals of the tangent vectors giving a dual space. Elements of these spaces are isomorphic and can be related by the musical isomorphisms $\flat : T\mathcal{M}_{\mathbf{x}} \to T^*\mathcal{M}_{\mathbf{x}}$ and $\sharp : T\mathcal{M}_{\mathbf{x}} \to T^*\mathcal{M}_{\mathbf{x}}$ see discussion in Section 2.1. 13

3.1 Lebedev Quadrature. Shown are the sample points of the Lebedev quadrature in the case of 302 nodes. The Lebedev nodes distribute nearly uniformly over the surface and are invariant under the rotations corresponding to octahedral symmetry [1, 2]. 38

3.2 Node Distribution of the Gauss-Legendre Quadrature Compared to Lebedev Quadrature. We consider the Gauss-Legendre quadrature with 5886 nodes with a comparable Lebedev quadrature having 5810 nodes (113^{th} order of accuracy) [2]. We see that the Gauss-Legendre quadrature has dense clustering of points along latitudinal rings when approaching the north and south poles. We see that while the Lebedev quadrature has some clustering around a few points, these are less dense and overall exhibits sampling with a greater level of symmetry over the sphere. 45
3.3 Convergence of the numerical Hodge star operator $\overline{\star}$ for 0-forms. We show for Manifold B how the relative error of $\overline{\star} f$ in approximating $\star f$ as the number of Lebedev nodes increases. The 0-form is $f = \exp(z)/(3-y)$. We investigate how the manifold geometry influences convergence by varying the amplitude r_0 in the range $[0.0, 0.4]$ for Manifold B. The amplitude $r_0 = 0.0$ corresponds to a sphere and $r_0 = 0.4$ to the final shape of Manifold B shown in Figure 1.1. We remark that all plots are log-log where for each data point for clarity we have labelled along the log x-axis the specific number of quadrature points. 54
3.4 Convergence of the numerical Hodge star operator $\overline{\star}$ for 1-forms. We show for Manifold B the relative error of $\overline{\star}\alpha$ in approximating $\star\alpha$ as the number of Lebedev nodes increases. The 1-form is $\alpha = \sqrt{|g|}\exp(z)d\theta + \sqrt{|g|}\exp(z)d\phi$. We investigate how the manifold geometry influences convergence by varying the amplitude r_0 in the range $[0.0, 0.4]$ for Manifold B. The amplitude $r_0 = 0.0$ corresponds to a sphere and $r_0 = 0.4$ to the final shape of Manifold B shown in Figure 1.1. 55
3.5 Convergence of the numerical exterior derivative operator $\overline{\mathbf{d}}$ for 0-forms. We show for Manifold B the relative error of $\overline{\mathbf{d}} f$ in approximating $\mathbf{d}f$ as the number of Lebedev nodes increases. The 0-form is $f = \exp(z)$. We investigate how the manifold geometry influences convergence by varying the amplitude r_0 in the range $[0.0, 0.4]$ for Manifold B. The amplitude $r_0 = 0.0$ corresponds to a sphere and $r_0 = 0.4$ to the final shape of Manifold B shown in Figure 1.1. 56

3.6 Convergence of the numerical exterior derivative operator $\overline{\mathbf{d}}$ for 1-forms. We show for Manifold B the relative error of $\overline{\mathbf{d}}\alpha$ in approximating $\mathbf{d}\alpha$ as the number of Lebedev nodes increases. The 1-form is $\alpha = |g|\exp(z)d\theta + |g|\exp(z)d\phi$. We investigate how the manifold geometry influences convergence by varying the amplitude r_0 in the range $[0.0, 0.4]$ for Manifold B. The amplitude $r_0 = 0.0$ corresponds to a sphere and $r_0 = 0.4$ to the final shape of Manifold B shown in Figure 1.1. 57

4.1 Lebedev Quadrature with 5810 nodes. We show on the left the Lebedev quadratures for integration of functions on a sphere of unit radius. The Lebedev quadrature integrates exactly all spherical harmonics up to the 131^{st} order [2]. The mapping of the sphere to the manifold on the right induces a new quadrature weighted by the local manifold metric. While the induced quadrature is no longer exact for spherical harmonics on the surface it still exhibits a high level of accuracy. We show by the colors the Gaussian curvature K on the surfaces over the range -7 to 7. . . 60

4.2 Quadrature on Radial Manifolds. For ellipsoids of oblate and prolate shapes we test the quadrature by integrating the Gaussian curvature over the manifold and compare the results with the predictions of the Gauss-Bonnet Theorem [3, 4]. We show the accuracy of the quadrature as the number of quadrature nodes Q increases and when varying the shape parameter r_0 of the ellipsoid, see equation 4.2.2 and equation 4.2.4. The case $r_0 = 0$ gives a sphere with the other r_0 values giving the shapes as shown in Figure 4.4. We show as insets the ellipsoids with $r_0 = 0.4$ and the Gaussian curvature distribution on the surface. 65

4.3 Quadrature on Radial Manifolds. We test our quadratures by integrating the Gaussian curvature on the manifold and comparing with the predictions of the Gauss-Bonnet Theorem [3, 4]. We show the relative errors as the number of quadrature points Q increases in the case of $r_0 = 0.3$ for the manifolds B and C given by equation 5.1.1. Since the Gaussian curvature is not known analytically in advance for these manifolds the test also validates the geometric approximations made in our numerical methods. . 67

4.4 Hydrodynamic Flow on Ellipsoids. We show on the left the ellipsoid shapes in the oblate and prolate cases from equation 4.2.2 and 4.2.2 as r_0 is varied. We use these shapes for computing hydrodynamic flows driven by the surface force density in equation 4.4.1 corresponding to the vector potential of equation 4.4.2. We investigate the accuracy of the hydrodynamics solver as the number of spherical harmonics increases and the shape is varied. We show on the right the hydrodynamics flows corresponding to equation 4.4.2 in the case of the oblate and prolate when $r_0 = 0.4$. 77

4.5 Convergence of the Stokes Flow for Oblate Ellipsoids. We show the relative errors of the L^2-norm of the potential, H^1-norm of the potential, and L^2-norm of the velocity. The results show how the error behaves as we increase the number of quadrature nodes Q and number of spherical harmonics. We use spherical harmonics up to degree $\lfloor L/2 \rfloor$ where L is the largest exact order of the corresponding Lebedev quadrature with Q nodes. We also show how convergence depends on the shape as r_0 is varied. We find in each case super-algebraic convergence of the hydrodynamic solver. For additional discussions can also see [5]. 78

4.6 Convergence of the Stokes Flow for Prolate Ellipsoids. We show the relative errors of the L^2-norm of the potential, H^1-norm of the potential, and L^2-norm of the velocity. The results show how the error behaves as we increase the number of quadrature nodes Q and number of spherical harmonics. We use spherical harmonics up to degree $\lfloor L/2 \rfloor$ where L is the largest exact order of the corresponding Lebedev quadrature with Q nodes. We also show how convergence depends on the shape as r_0 is varied. We find in each case super-algebraic convergence of the hydrodynamic solver. For additional discussions can also see [5]. 79

5.1 Radial Manifold Shapes. We consider hydrodynamic flows on manifolds with shapes ranging from the sphere to the more complicated geometries generated by equation 5.1.1. We show with colors the Gaussian curvature of the shapes. We take Manifold A to be a sphere of radius $R = 1.0$. We show Manifold B with $r_0 = 0.4$ and Manifold C with $r_0 = 0.4$ in equation 5.1.1. 83

5.2 Structure of the hydrodynamic flow. We consider the case of three particles immersed within an interface of spherical shape and subjected to force. We generate a force density on the surface using the extended immersed boundary method for manifolds we introduced in [6]. The particles are configured at the locations $\mathbf{x}_1 = (-1, 0, 0)$, $\mathbf{x}_2 = (1, 0, 0)$, $\mathbf{x}_3 = (0, -1, 0)$, and each subjected to the force $\mathbf{F} = (0, 0, 1)$. We show in the left panel the immersed boundary approach for fluid-particle coupling on manifolds [6] and range of spreading around each particle used to obtain a force density on the surface. We show in the right panel the hydrodynamic flow response. The flow exhibits two two vortices and global recirculation of the fluid. We visualize the streamlines of the hydrodynamics flows using Line Integral Convolution (LIC) [7]. Hydrodynamic results are for the case with $\mu = 0.1$,$\gamma = 0.1$ and $Q = 5810$ [8]. 87

5.3 Structure of the Hydrodynamic Flow. We show for Manifold B and C the hydrodynamic flow responses for a localized unit force applied in the tangential direction to particles on the surface at the push-forward of the locations discussed in Figure 5.2. We visualize the streamlines using Line Integral Convolution (LIC) [7]. The flow responses exhibit eight critical points corresponding to six vortices and four saddle points. The vortices are marked with red points and the saddle points with cyan points. We sketch approximate separatrices for each of the saddle points. For these surfaces the hydrodynamic flows appear to exhibit structures that favor more localized recirculation of the fluid relative to the responses seen for the sphere in Figure 5.2 [8]. 90

5.4 Topological Transitions in the Flow Structure. As the shapes of the manifolds deviate more from the sphere the velocity field of the hydrodynamic flow undergoes a topological transition with the creation of new vortices and saddle-points. The topological structures appear to correspond with the flow reorganizing to recirculate fluid in a more localized manner relative to the global recirculation seen on the sphere. This is especially pronounced in the elongated geometries that form for the Manifold C shapes. We show configurations for Manifold B and Manifold C when $r_0 = 0.0, 0.15, 0.25, 0.4$ in equation 5.1.1. We quantify the Rayleigh-Dissipation associated with each of these flows in Figure 5.5. 93

5.5 Rayleigh-Dissipation Rates of Hydrodynamic Flows. Hydrodynamic flows $\mathbf{v}$ on surfaces are obtained by solving the Stokes equations 2.5.3 as r_0 is varied. We take $\mu_m = 0.1$ and $\gamma = 0.1$ for the manifolds in Figure 5.1. RD rates for $\mathbf{v}$ are shown as solid curves. For comparison we consider the rates obtained from the velocity field $\hat{\mathbf{v}}$ of flow on the sphere (case $r_0 = 0$) obtained by the pushed-forward $\tilde{\mathbf{v}} = \phi_* \hat{\mathbf{v}}$ to the manifold shape with given r_0. RD rates for $\tilde{\mathbf{v}}$ are shown as dotted curves. We find that as the geometry deviates from the sphere the rates for the Stokes flow on the manifold become significantly smaller than the push-forward flow fields from the sphere. We find the two cases begin to diverge significantly in the regime where the velocity field transitions topologically with the addition of new vortices and saddle-point stagnation points as in Figure 5.3. This transition occurs for Manifold B around $r_0^* = 0.105$ and for Manifold C around $r_0^* = 0.085$ (vertical dashed line). These results indicate some of the ways that surface geometry can contribute to dissipation rates and hydrodynamic flow responses [8]. 94

5.6 Counter-Rotated Hydrodynamic Flows. We consider the case of three particles configured at the locations $\mathbf{x}_1 = (-1, 0, 0)$, $\mathbf{x}_2 = (1, 0, 0)$, $\mathbf{x}_3 = (0, -1, 0)$ embedded within an interface and subjected to force $\mathbf{F} = (0, 0, 1)$ for the sphere and tangent for the other manifolds. We use our extended immersed boundary method for manifolds we introduced in [6]. In the left panel, we show the hydrodynamic responses for $\mu = 0.1$,$\gamma = 0.1$ and $Q = 5810$. In the middle panel, we show the rotational field that best counters the rigid-body rotation of the fluid interface. In the right panel, we have combining the velocity fields to arrive at a counter-rotated velocity field that would be observed in the moving reference frame. We visualize the streamlines of the hydrodynamics flows using Line Integral Convolution (LIC) [7]. 96

6.1 GMLS Approximation of Target Functionals. In the Generalized Moving Least Squares (GMLS) approach a collection of scattered data samples of the function values u is approximated by multiple local reconstructions. This is done by building an ϵ-graph between the points within an ϵ-neighborhood around a base point $\tilde{\mathbf{x}}$ (shown on the left). A function space $\mathbb{V}_h$ is used to reconstruct u by finding the best fitting function $p^* \in \mathbb{V}_h$ that matches the values of the sampling functionals $\{\lambda_j\}$ in the optimization problem given in equation 6.1.4 (shown on the right). For approximating a target functional τ acting on u at the base point $\tilde{\mathbf{x}}$, we obtain the approximating GMLS functional τ^h by evaluating the target functional on the reconstruction space at p^*. In this manner we can obtain approximations to general functionals acting on u [9]. . 102

6.2 GMLS Surface Reconstruction and Local Parameterization. For a manifold represented as a point set, we use a GMLS approach to obtain local patches and coordinate charts for parameterizing the surface. At a given base point $\tilde{\mathbf{x}}$ we collect all neighbors within an ϵ-ball and perform Principle Component Analysis (PCA) to determine a local tangent plane and normal for the surface. We parameterize the surface locally using $(\xi^1, \xi^2, q(\xi^1, \xi^2))$, where we obtain $q(\xi^1, \xi^2)$ by performing a GMLS reconstruction of the surface [9]. 106

6.3 Point Set Representations of Manifolds. Manifold A is an ellipsoid defined by the equation $x^2/a^2 + y^2/b^2 + z^2 = s_0^2$ with $a = 1.2, b = 1.2, s_0^2 = 1$. Manifold B is a radial manifold defined in spherical coordinates by $(\theta, \phi, r(\theta, \phi)$ where $r(\theta, \phi) = 1 + r_0 \sin(3\phi)\cos(\theta)$ with $r_0 = 0.1$. Manifold C is a radial manifold defined in spherical coordinates by $(\theta, \phi, r(\theta, \phi)$ where $r(\theta, \phi) = 1 + r_0 \sin(7\phi)\cos(\theta)$ with $r_0 = 0.1$. Manifold D is a torus defined by the equation $(s_1^2 - \sqrt{x^2 + y^2})^2 + z^2 = s_2^2$ with $s_1^2 = 0.7, s_2^2 = 0.3$. Each of the manifolds shown are represented by quasi-uniform point sets with approximately $n = 10^4$ samples. For quasi-uniform sampling we expect the fill-distance h to scale as $h \sim 1/\sqrt{n}$. When reporting our results, we use throughout the notation $\bar{h}^{-1} = \sqrt{n}$. We discuss further details of the point sampling of the manifolds in Section 7.0.1. 112

6.4 GMLS Estimate of the Gaussian Curvature vs Point Set Resolution. We show on log-log scale the convergence of the GMLS-based estimation of Gaussian Curvature as the number of sample points is increased. The $\bar{h}^{-1} = \sqrt{n}$, where n is the number of points. Manifold B and Manifold C present the greatest challenge given localized regions of particularly large Gaussian Curvatures, see Figure 6.5. We find the accuracy is 5^{th}-order in agreement with the suggestive prediction $m+1-k$ similar to equation 6.1.9, where in our GMLS approximation $m = 6, k = 2$, see Table 6.1. 114

6.5 Gaussian Curvature from GMLS Estimation. We use a GMLS reconstruction approach to estimate the Gaussian Curvature of each of the manifolds using Equation 6.3.10. Shown are results for the case of a quasi-uniform sampling of the surface with approximately $n = 10^4$ samples for each manifold. We show the L^2-error of the GMLS approximation of the Gaussian curvature and convergence rate in Figure 6.4. 115

7.1 Approach for Computing Numerically the Surface Hydrodynamic Flows. For a given body force density or stresses $\mathbf{b}$ acting on the surface fluid we convert the fields to covariant form $\mathbf{b}^\flat$, shown in (i),(ii). To handle incompressibile flows, we convert all fields to a divergence-free gauge using the generalized surface curl $-\star\mathbf{d}\mathbf{b}^\flat$, shown in (iii). We solve for the vector potential Φ of the surface hydrodynamic flow using equations 7.1.1 or 7.1.2 and our GMLS collocation methods for the differential operators, shown in (iv). We construct the covariant form of the velocity field of the hydrodynamic flow response using the generalized surface curl $\mathbf{v}^\flat$, shown in (v). We obtain our final results by converting the covariant form $\mathbf{v}^\flat$ to the velocity field by $\mathbf{v} = \left(\mathbf{v}^\flat\right)^\sharp$. This yields the surface hydrodynamic flow shown in (vi) [9]. 120

7.2 GMLS Approximation of Operators vs Resolution. We show log-log plot of the L^2-error of the GMLS approximation of the surface operators with $m_1 = m_2 = 6$. We find in each case our GMLS numerical methods converge with a high order of accuracy in $\bar{h}$ as reported in Table 7.2– 7.4 [9]. 127

7.3 GMLS Approximation of Operators vs Resolution. We show log-log plot of the L^2-error of the GMLS approximation of the surface operators with $m_1 = m_2 = 6$. We find in each case our GMLS numerical methods converge with a high order of accuracy in $\bar{h}$ as reported in Table 7.2– 7.4 [9]. 128

7.4 Surface Hydrodynamic Flows on Manifolds A–D. For a given force density, shown in (i), we use our GMLS solver to compute numerically the surface hydrodynamic flow responses, shown in (ii)–(iv), on each of the manifolds, defined in Section 6.4.1. Manifold $A - D$ solutions were computed at a resolution with number of sample points $n_A = 38,486, n_B = 147,634, n_C = 127,346$, and $n_D = 118,942$ [9]. 134
7.5 Convergence of GMLS Solvers for the Hydrodynamic Velocity Field. We use the GMLS methods with $m_1 = m_2 = m$ polynomial orders for approximating the surface geometry and surface velocity field $\mathbf{v}$. We study convergence for the GMLS solver when using the biharmonic formulation in equation 7.1.1 verses when using the split formulation in equation 7.1.2 [9]. 136

Chapter 1

Introduction

We develop high-order numerical methods for a continuum mechanics formulation of hydrodynamic flows within two-dimensional curved fluid interfaces.

1.1 Problem Motivation

Hydrodynamics within curved geometries play an important role in diverse physical systems including the thin films of soap bubbles [10, 11, 12, 13], lipid bilayer membranes [14, 15, 6, 16, 17] and recent interface-embedded colloidal systems [18, 19, 20, 21, 22, 21]. Similar hydrodynamic and related curvature mediated phenomena also plays an important role in physiology such as in the cornea of the eye with its tear film [23], transport of surfactants in lung alveoli [24, 25] or in cell mechanics [26, 27, 17]. Each of these systems involve potential interactions between the curvature of the interface and hydrodynamic flows. We investigate these types of flows by formulating continuum mechanics equations for hydrodynamics using variational principles and the exterior calculus of differential

geometry [28]. This provides an abstraction that is helpful in generalizing many of the techniques of fluid mechanics to the manifold setting while avoiding many of the tedious coordinate-based calculations of tensor calculus. The exterior calculus formulation also provides a coordinate-invariant set of equations, more readily providing insights into the roles played by the geometry in the hydrodynamics than alternative tensor calculus approaches [29, 30, 31].

There has been a significant amount of experimental and theoretical work developing approaches for investigating hydrodynamics within curved fluid interfaces [32, 33, 34, 35]. Experimental work includes single particle tracking of inclusions to determine information about interfacial viscosity and diffusivities [15, 36]. Even the formulation of the correct continuum mechanics equations presents some significant challenges in the manifold setting [28]. For instance in a two-dimensional curved fluid sheet the equations must account for the distinct components of linear momentum correctly. The concept of momentum is not an intrinsic field of the manifold and must be interpreted with respect to the ambient physical space [28]. For instance, when considering non-relativistic mechanics in an inertial reference frame with coordinates x, y, z, the x-component of momentum is a conserved quantity distinct from the y and z-components of momentum. An early derivation using coordinate-based tensor calculus in the ambient space was given for hydrodynamics within a curved two-dimensional fluid interface in Scriven [35]. This was based on the more general shell theories

developed in [37, 38]. Many subsequent derivations have been performed using tensor calculus for related fluid-elastic interfaces motivated by applications. This includes derivation of equations for surface rheology [39, 40, 41], investigation of red-blood cells [42], surface transport in capsules and surfactants on bubbles [32, 12], and investigations of the mechanics, diffusion, and fluctuations associated with curved lipid bilayer membranes [43, 44, 45, 46, 47, 48, 49, 6, 50]. Recent works by Marsden et al. [28, 31, 51] develop the continuum mechanics in the more general setting when both the reference body and ambient space are treated as general manifolds as the basis for rigorous foundations for elasticity [28, 31]. In this work, some of the challenges associated with momentum and stress with reference to ambient space can be further abstracted in calculations by the use of covector-valued differential forms and a generalized mixed type of divergence operator [31, 51]. A particularly appealing way to derive the conservation laws for manifolds is through the use of variational principles based on the balance of energy and symmetries [28]. This has recently been pursued to derive elastic and hydrodynamic equations for lipid membranes in [52, 53, 50]. We briefly present related derivations based on the energy balance approach of [28, 51] to obtain our hydrodynamic equations.

There has been a lot of recent interest and work on developing computational methods for evaluating differential operators and for solving equations on curved surfaces [54, 55, 56, 57]. There has been a lot of recent interest in

numerical methods related to exterior calculus [58, 59, 60, 61]. This has been motivated in part by applications in computer graphics [56, 62, 63], electrodynamics [64], and interest in applications using shell theories for elasticity and hydrodynamics [53, 52, 65, 49, 17, 66, 67]. Many computational methods treat the geometry using a triangulated surface and build discrete operators to model their curvature and differential counter-parts [68, 69, 70, 71, 72, 73, 74]. Some early work in this direction includes [68, 69, 70, 71] and the Surface Evolver of Brakke [75]. More recently, discrete approaches such as the Discrete Exterior Calculus (DEC) [72, 76], Finite Element Exterior Calculus (FEEC) [77, 78] and Mimetic Methods (MM) [79] have been developed that aim to reproduce in the numerics analogous properties of the differential operators related to the geometric and topological structure of the manifold [79, 72, 76, 73, 77, 78, 58]. In these discrete exterior calculus approaches an effort is made to introduce approximations for fundamental operators such as the exterior derivative $\mathbf{d}$ and Hodge star $\star$ operators that on the discrete level preserve inherent geometric relations [59, 77, 61]. These operators can then be composed to perform geometric processing tasks or approximate differential equations. For manifolds represented by discrete symplicial complexes this includes preserving the adjoint conditions between the exterior derivative, boundary operator, and co-differentials to create a discrete analogue of the de Rham complex and related theory [80, 3, 81]. This has been used to obtain models of surface Laplacians and results like discrete

Hodge decompositions [79, 77, 78, 56]. For finite elements these properties can be shown to be essential for discretizing problems in elasticity and fluid mechanics to obtain well-posed approximations with stable numerical methods [79, 77, 78]. In the DEC approach to formulating numerical methods for PDEs on manifolds, the methods obtained are similar to finite differences [72, 58]. This work has allowed for impressive results including schemes that are exactly conservative for quantities such as mass and vorticity [82, 55]. Deriving operators preserving geometric structure is non-trivial and current numerical methods for spherical topologies are typically first or second order accurate [82, 55]. Recent methods have been developed in the setting of tensor product basis that are spectrally accurate in [83].

We also mention there are many meshfree approaches for solving PDEs. These may be characterized broadly by the underlying discretization; this includes Radial Basis Functions (RBFs) [84], Smooth Particle Hydrodynamics (SPH) [85], and approaches Generalized Finite Difference/Moving Least Squares/Reproducing Kernel Particle Method (GFD/MLS/RKPM) [86]. While the majority of meshfree literature targets solution of PDEs in $\mathbb{R}^d$, significant recent work has focused on the manifold setting [87, 88, 89, 90, 91]. In the last decade, substantial work has been done to use RBFs to solve shallow-water equations on the sphere [92]. The meshfree setting is attractive particularly for building semi-Lagrangian schemes of interest in atmosphere science [93, 94, 92]. In these

schemes the discretizations are typically cast in strong form resembling a collocated finite difference method, and thus often have difficulty obtaining stable solutions for flow problems. While predictive simulations have been obtained, they typically rely upon the introduction of an artificial hyper-viscosity to obtain stable results [95, 93, 96]. While SPH approaches offer attractive structure-preserving properties, particularly in conserving invariants of Lagrangian transport, it is in general not possible to simultaneously obtain conservation principles and a consistent discretization [97]. MLS/RKPM/GFD approaches provide a compelling alternative by addressing accuracy issues through the explicit construction of approximations with polynomial reproduction properties and an accompanying rigorous approximation theory [98, 99], but lack a stability theory. There have been several examples of successful discretization of scalar surface PDEs [100, 101]. In Generalized Moving Least Squares (GMLS) this approach is extended to enable the recovery of arbitrary linear bounded target functionals from scattered data [98, 102].

1.2 Overview (What we do)

This thesis can be divided into three parts. We first derive our hydrodynamics in the langauge of exterior calculus in Chapter 2. Then, we implement a hydrodynamic solver (in python) for manifolds with radial geometries, as described in

Chapters 3-5. Finally, we use GMLS to extend our results to manifolds with Spherical Topologies (using the Compadre package) GMLS, in Chapters 6-7.

In Chapter 2 we introduce the basic operators of exterior calculus, and use these to formulate conservation laws of continuum mechanics in the manifold setting. We expand many of the operators from exterior calculus in the 2-dimensional manifolds, allowing us to view the actions of these operators in a coordinate-free way. We formulate our hydrodynamic equations for curved fluid interfaces, making use of the relations in the exterior calculus such as the Hodge decomposition and adjoint conditions on exterior derivatives and co-differentials.

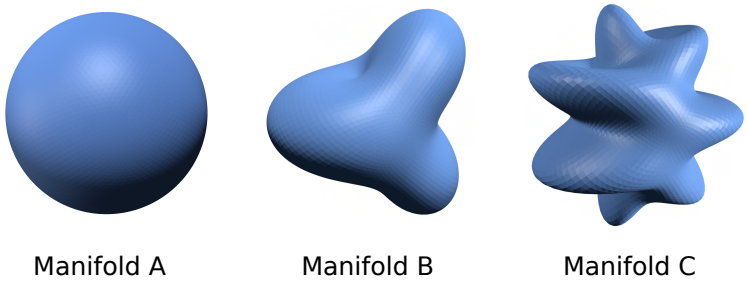

Figure 1.1: Radial Manifolds: A radial manifold is defined as a surface where each point can be connected by a line segment to the origin without intersecting the surface. Shown are three radial manifolds which for discussions we refer to interchangeably as the (i) Sphere / Manifold A, (ii) Dimple / Manifold B, and (iii) Fountain / Manifold C. The manifolds are generated (in spherical coordinates) by the radial functions (i) $r(\theta, \phi) = 1.0$, (ii) $r(\theta, \phi) = 1 + r_0 \sin(3\phi)\cos(\theta)$ with $r_0 = 0.4$, and (iii) $r(\theta, \phi) = 1 + r_0 \sin(7\phi)\cos(\theta)$ with $r_0 = 0.4$. The differential geometry of radial manifolds is derived in Section 3.1.

In Chapter 3 we use an L^2-projection to spherical harmonics (using Lebedev quadratures) to approximate the exterior derivative operator $\mathbf{d}$ and Hodge star operator $\star$ on radial manifolds, ie. smooth manifolds that occupy a star-shaped domain in $\mathbb{R}^3$. Using derivations of the differential geometry for general radial manifolds, such as those in Figure 1.1, we can discretize these exterior calculus operators. We show that our methods provide spectrally accurate approximations for these operators. While our numerical methods do not seek to preserve exactly the geometric and topological relations between our approximate exterior operators, we have from the spectral representation that these relations hold for our expansions to a high level of accuracy, via hyperinterpolation.

In Chapter 4 we demonstrate spectrally accurate methods for solving hydrodynamic flows on curved surfaces having general radial manifold shape based on a weak exterior calculus formulation of the hydrodynamic equations. Since Lebedev nodes were developed for quadratures on the sphere, we extend them to obtain quadratures for general radial manifolds by making use of a coordinate-independent change of measure formula derived using the Radon-Nikodym Theorem [103]. We mention that alternative formulations are also possible related to our approach in terms of discrete triangulations provided appropriate transport theorems and quadrature are developed over the mesh. We test the accuracy of our quadrature scheme for general radial manifolds by integrating the Gaussian curvature over the surface. From the Gauss-Bonnet Theorem this should give the

Euler characteristic for the spherical topology and independent of the detailed geometric shape [4, 3]. We then provide convergence results for our hydrodynamics solver in a few special cases with known hydrodynamics solutions showing the solver's accuracy.

In Chapter 5 we demonstrate our numerical methods for a few example manifolds by investigating hydrodynamic flow responses and the role of surface geometry. As a baseline, we first consider hydrodynamic flows driven by particles configured on a sphere and subjected to force. We investigate for equivalent forcing how these hydrodynamic flow responses change when the particles are on a surface having a more complicated geometry. We find as the geometry has more heterogeneous curvatures the structure of the hydrodynamic flow fields are observed to change significantly. In some cases this appears to correspond to a topological transformation of the stream-lines of the flow. The fluid flow is observed to result in a transition from a more global recirculation of fluid to a much more localized recirculation of fluid and can result in the creation of new singularities (stagnation points) that take the form of new vortices and saddle points. We use our numerical methods to report on the Rayleigh-Dissipation associated with these hydrodynamic flow responses. We find that these quantitative and topological changes may play a role in mitigating dissipation within the fluid for certain geometries. We mention that related to our findings some work on fluid

dissipation in the case of perturbations from a flat sheet, such as in a planar soap film, were recently investigated in [104].

In Chapter 6 we introduce meshfree methods based on a Generalized Moving Least Squares (GMLS) approach. The manifold is represented as a collection of points embedded in an ambient space. At each point we consider a function space generated by a local basis of shapes. In our case, we use multivariant polynomials of finite degree. We extract geometric information to high-order by fitting a local function from this space to the neighborhood of points [105, 106, 107, 108]. To represent scalar and vector fields on the surface we take a similar approach.

In Chapter 7 we again present the Stokes problem in exterior calculus form, slightly reformulating these equations for maximum compatibility with GMLS. We illustrate how GMLS is able to accurately handle the disretization of exterior calculus operators [88]. Finally, we implement this Stokes scheme in the Compadre toolkit [109], an open-source high-performance Trilinos library supporting meshfree discretization at scale. In this context we show through numerical experiment that the scheme is able to obtain high-order convergence to manufactured solutions without the need for numerical stabilization.

In summary, our methods and results show some of the rich ways that surface geometry can impact hydrodynamic flow responses within curved fluid interfaces. The development of the GMLS and exterior calculus tools presented in this manuscript constitutes a foundational work which may be used in the future

to handle a wide range of problems involving flow on deforming manifolds and investifating phenomena in curved fluid interfaces. To do this, we must first establish how exterior calculus operators may be handled in the GMLS framework. With this goal in mind, we first summarize the GMLS method in the context of surface PDEs.

Chapter 2

Using Exterior Calculus Operators to Formulate the Stokes Problem

The exterior calculus allows for a covariant formulation of the equations avoiding the need to explicitly express the metric tensor and components. This reveals more readily and intuitively in many cases the roles played by geometry. The exterior calculus will ultimately simplify many of our calculations in fluid mechanics by providing an analogue to often employed vector calculus techniques used in the Euclidean case. We briefly review for exterior calculus the basic definitions and relations we shall make use of in our calculations. For a more comprehensive and detailed discussion see [80, 3].

2.1 Vector and Exterior Calculus on Riemannian Manifolds

We consider smooth n-dimensional closed Riemann manifolds $\mathcal{M}$ with metric $\mathbf{g}$. We have from the Whitney Embedding Theorem [80, 110] that we can always express such manifolds as an embedding in a space $\mathbb{R}^N$ provided N is sufficiently large. We consider the embedding map $\boldsymbol{\sigma} = \boldsymbol{\sigma}(\mathbf{x}) : \mathbb{R}^n \to \mathbb{R}^N$ associated with a chart having coordinates x^i. Note tht Einstein summation conventions are used throughout. We adopt the usual convention of indexing contravariant tensors with superscripts and covariant tensors with subscripts [80, 111].

The tangent space at location $\mathbf{x}$ consists of the span of the vectors $\partial\boldsymbol{\sigma}/\partial_{x^i} \in \mathbb{R}^N$. We denote the tangent space by $T\mathcal{M}_\mathbf{x} = \text{span}\,\{\partial_{x^i}\}$ with the usual notation

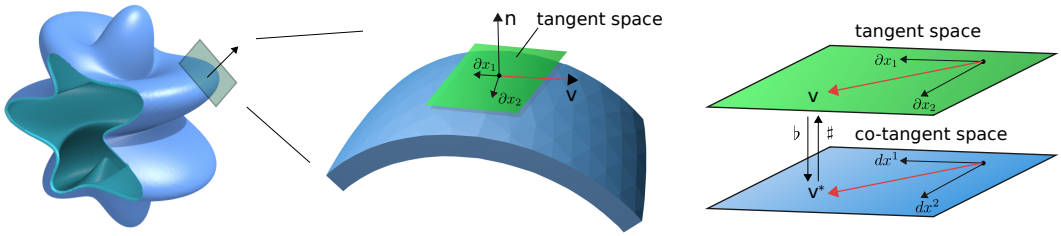

Figure 2.1: Continuum Mechanics for Manifolds. We consider continuum mechanics formulated within general curved spaces having non-euclidean metric. At each point of the manifold the tangent space $T\mathcal{M}_\mathbf{x}$ consists of all vectors tangent to the manifold when thought of as an embedding. The cotangent space $T^*\mathcal{M}_\mathbf{x}$ consists of all linear functionals of the tangent vectors giving a dual space. Elements of these spaces are isomorphic and can be related by the musical isomorphisms $\flat : T\mathcal{M}_\mathbf{x} \to T^*\mathcal{M}_\mathbf{x}$ and $\sharp : T\mathcal{M}_\mathbf{x} \to T^*\mathcal{M}_\mathbf{x}$ see discussion in Section 2.1.

for the basis vectors $\partial_{x^i} := \partial\boldsymbol{\sigma}/\partial_{x^i} = \boldsymbol{\sigma}_{x^i}$ [80]. The co-tangent space corresponds to the dual $T^*\mathcal{M}_{\mathbf{x}}$ of the tangent space consisting of all linear functionals acting on vectors in $T\mathcal{M}_{\mathbf{x}}$. The linear functional corresponding to vector $\mathbf{u} = u^i\partial_{x^i}$ is denoted by $\mathbf{u}^*$ having the action on a vector $\mathbf{v} = v^i\partial_{x^i}$ given by $\mathbf{u}^*[\mathbf{v}] = u^i g_{ij} v^j$ where $g_{ij} = \boldsymbol{\sigma}_{x^i} \cdot \boldsymbol{\sigma}_{x^j} = \langle \partial_{x^i}, \partial_{x^j} \rangle$ is the metric tensor. We can use as a basis for the co-tangent space $\mathbf{dx}^i$ which denotes the linear functional having the action $\mathbf{dx}^i[\partial_{x^j}] = \delta^i_j$ where δ^i_j is the Kronecker δ-function which is one if $i = j$ and otherwise zero. This allows for representing a general linear functional of the co-tangent space as $\mathbf{u}^* = u_i \mathbf{d}x^i$. With these conventions we can define isomorphisms between the tangent and co-tangent spaces $\flat : T\mathcal{M}_{\mathbf{x}} \to T^*\mathcal{M}_{\mathbf{x}}$ and $\sharp : T^*\mathcal{M}_{\mathbf{x}} \to T\mathcal{M}_{\mathbf{x}}$. These correspond to the relationships between the representations $\mathbf{u} = u^i\partial_{x^i}$ and $\mathbf{u}^* = u_i\mathbf{d}x^i$ with $\mathbf{u}^\flat = \mathbf{u}^*$ and $[\mathbf{u}^*]^\sharp = \mathbf{u}$. In terms of coordinates these maps give $[\mathbf{u}^\flat]_i = u_i = g_{ij}u^i$ and $[\mathbf{u}^\sharp]^i = u^i = g^{ij}u_j$. The g_{ij} are the components of the metric tensor and g^{ij} are components of the inverse metric tensor. The $\sharp$ and $\flat$ are often referred to as the musical isomorphisms since this helps remember how they correspond in coordinates to lowering and raising the indices [80]. This illustrated in Figure 2.1.

We can also define functionals that take multiple vectors as input. We define k-forms $\boldsymbol{\alpha}(\mathbf{u}_1, \ldots, \mathbf{u}_k)$ as functionals that are linear and have the anti-symmetric property $\boldsymbol{\alpha}(\mathbf{u}_{\sigma(1)}, \ldots, \mathbf{u}_{\sigma(k)}) = \text{sign}(\sigma)\boldsymbol{\alpha}(\mathbf{u}_1, \ldots, \mathbf{u}_k)$. We can combine k-forms $\boldsymbol{\alpha}$

and ℓ-forms $\boldsymbol{\beta}$ to obtain $(k+\ell)$-forms using the wedge product $\wedge$ defined as

$$\boldsymbol{\alpha} \wedge \boldsymbol{\beta} = \frac{1}{k!\ell!} \sum_{\sigma \in \mathbb{P}_{k+\ell}} \text{sign}(\sigma) \boldsymbol{\alpha}(\mathbf{u}_{\sigma(1)}, \ldots, \boldsymbol{u}_{\sigma(k)}) \boldsymbol{\beta}(\mathbf{u}_{\sigma(k+1)}, \ldots, \boldsymbol{u}_{\sigma(k+\ell)}). \quad (2.1.1)$$

The $\mathbb{P}_{k+\ell}$ is the permutation group on $k+\ell$ elements. This has the useful property that $\boldsymbol{\alpha} \wedge \boldsymbol{\beta} = (-1)^{k\ell} \boldsymbol{\beta} \wedge \boldsymbol{\alpha}$. This allows us to construct from the 1-forms $\boldsymbol{\alpha}$, $\boldsymbol{\beta}$ the differential forms that can be integrated over a two-dimensional surface as $\boldsymbol{\lambda} = \boldsymbol{\alpha} \wedge \boldsymbol{\beta}$ or more generally n-dimensional surfaces as $\boldsymbol{\lambda} = \boldsymbol{\alpha}^{(1)} \wedge \cdots \wedge \boldsymbol{\alpha}^{(n)}$. We define the exterior derivative $\mathbf{d}$ acting on a k-form $\boldsymbol{\alpha} = \alpha_{i_1,\ldots,i_k} \mathbf{dx}^{i_1} \wedge \cdots \mathbf{dx}^{i_k}$ as the resulting $(k+1)$-form

$$\mathbf{d}\boldsymbol{\alpha} = \frac{1}{k!} \frac{\partial}{\partial x^j} \alpha_{i_1,\ldots,i_k} \mathbf{dx}^j \wedge \mathbf{dx}^{i_1} \wedge \cdots \mathbf{dx}^{i_k}. \quad (2.1.2)$$

Here we have taken that the k-form to be $\alpha = (1/k!)\, \alpha_{i_1 \ldots i_k} \mathbf{dx}^{i_1} \wedge \cdots \wedge \mathbf{dx}^{i_k}$, where $\wedge$ denotes the wedge product [111, 80]. Since we are using the Einstein summation conventions, all permutations of the indices can arise and hence the factor of $1/k!$. For notational convenience and to make expressions more compact we will sometimes adsorb this factor implicity into $\alpha_{i_1 \ldots i_k}$.

When integrating over the manifold it is useful to define an L^2-inner-product on differential forms. We use the volume n-form of the manifold ω to define the manifold L^2-inner-product

$$\langle \boldsymbol{\alpha}, \boldsymbol{\beta} \rangle_{\mathcal{M}} = \int_{\mathcal{M}} \langle \boldsymbol{\alpha}, \boldsymbol{\beta} \rangle_g \, \omega. \quad (2.1.3)$$

By using the isomorphisms $\sharp$ and $\flat$ between the co-tangent and tangent space we have that the local metric inner-product on differential forms is equal to the

local metric inner-product on the isomorphic vector fields $\langle \boldsymbol{\alpha}, \boldsymbol{\beta} \rangle_g = \langle \boldsymbol{\alpha}^\sharp, \boldsymbol{\beta}^\sharp \rangle_g$. As a consequence, the L^2-inner-product on differential forms is consistent with the L^2-inner-product defined on the isomorphic vector fields

$$\langle \boldsymbol{\alpha}, \boldsymbol{\beta} \rangle_{\mathcal{M}} = \langle \boldsymbol{\alpha}^\sharp, \boldsymbol{\beta}^\sharp \rangle_{\mathcal{M}} . \tag{2.1.4}$$

This is useful allowing us to perform calculations in either representation as convenient. We define the Hodge star $\star$ as the operator that for any k-form $\boldsymbol{\gamma}$ and $\boldsymbol{\lambda}$ gives

$$\int_{\mathcal{M}} \boldsymbol{\gamma} \wedge \star \boldsymbol{\lambda} = \int_{\mathcal{M}} \langle \boldsymbol{\gamma}, \boldsymbol{\lambda} \rangle_g \omega = \langle \boldsymbol{\gamma}, \boldsymbol{\lambda} \rangle_{\mathcal{M}}. \tag{2.1.5}$$

where ω is the volume n-form of the closed manifold. In coordinates we can express the Hodge star $\star \boldsymbol{\alpha}$ as the $(n-k)$-form

$$\star \boldsymbol{\alpha} = \frac{\sqrt{|g|}}{(n-k)!k!} \alpha^{i_1,\ldots,i_k} \epsilon_{i_1,\ldots,i_k,j_1,\ldots,j_{n-k}} \mathbf{d}x^{j_1} \wedge \cdots \wedge \mathbf{d}x^{j_{n-k}}. \tag{2.1.6}$$

The $\epsilon_{\ell_1,\ldots,\ell_n}$ denotes the Levi-Civita tensor which gives the sign of the permutation of the indices $\ell_1, \ldots, \ell_n$ and is otherwise zero. When working with differential forms the Hodge star gives the analogue for differential forms of taking the orthogonal complement of a vector subspace [80].

For smooth orientable n-dimensional manifolds the Hodge star satisfies a number of useful identities that we shall use in our derivations. The first is that $\star \star \boldsymbol{\eta} = (-1)^{k(n-k)} \boldsymbol{\eta}$ where $\boldsymbol{\eta}$ is a k-form. If we have $\boldsymbol{\gamma} = \star \boldsymbol{\eta}$ then we can use two applications of the Hodge-star to determine that the inverse is again a Hodge

star operator multiplied by a sign so that $\boldsymbol{\eta} = \star^{-1}\boldsymbol{\gamma} = (-1)^{k(n-k)} \star \boldsymbol{\gamma}$. From these relations we have the useful identity that

$$\langle \boldsymbol{\gamma}, \boldsymbol{\lambda} \rangle_{\mathcal{M}} = \langle \star\boldsymbol{\gamma}, \star\boldsymbol{\lambda} \rangle_{\mathcal{M}}. \tag{2.1.7}$$

Furthermore, we have the adjoint relationship

$$\langle \star\boldsymbol{\gamma}, \boldsymbol{\lambda} \rangle_{\mathcal{M}} = (-1)^{k(n-k)} \langle \boldsymbol{\gamma}, \star\boldsymbol{\lambda} \rangle_{\mathcal{M}}. \tag{2.1.8}$$

In other words, the adjoint operator to the Hodge star is $\star^T = (-1)^{k(n-k)}\star$. It is often useful to work with the adjoint of the exterior derivative $\boldsymbol{\delta} = \mathbf{d}^T$ where the co-differential operator is defined as $\boldsymbol{\delta} = (-1)^{n(k-1)+1} \star \mathbf{d} \star$. With these definitions it follows that the exterior derivative $\mathbf{d}$ and codifferential $\boldsymbol{\delta}$ satisfy

$$\langle \boldsymbol{\delta}\boldsymbol{\alpha}, \boldsymbol{\beta} \rangle_{\mathcal{M}} = \langle \boldsymbol{\alpha}, \mathbf{d}\boldsymbol{\beta} \rangle_{\mathcal{M}}. \tag{2.1.9}$$

These summarize a few relationships and identities in exterior calculus that we shall make use of in our subsequent calculations.

2.2 Formulating Vector Operators as Exterior Calculus Operators

With these conventions we can generalize many of the operators that arise in vector calculus in the context of surfaces as

$$\operatorname{grad}_{\mathcal{M}}(f) = [\mathbf{d}f]^{\sharp}, \qquad \operatorname{div}_{\mathcal{M}}(\mathbf{F}) = -(-\star\,\mathbf{d}\star\,\mathbf{F}^{\flat}) = -\boldsymbol{\delta}\mathbf{F}^{\flat}, \tag{2.2.1}$$

$$\operatorname{curl}_{\mathcal{M}}(\mathbf{F}) = \left[-\star\,\mathbf{d}\mathbf{F}^{\flat}\right]^{\sharp}.$$

The f is a function (0-form) and $\mathbf{F}$ is a 1-form.

It is also natural to consider common vector calculus differential operators such as the Laplacian. It is important to note that on manifolds there are a few different operators that share many of the features with the Laplacian of vector calculus. This requires care when formulating conservation laws or considering constitutive models. A few generalizations and related operators of the Laplacian include

$$\Delta^H(\mathbf{F}) = \left[(\boldsymbol{\delta}\mathbf{d} + \mathbf{d}\boldsymbol{\delta})\,\mathbf{F}^\flat\right]^\sharp, \quad \Delta^S(\mathbf{F}) \tag{2.2.2}$$

$$= \left[-\boldsymbol{\delta}\mathbf{d}\mathbf{F}^\flat\right]^\sharp, \quad \Delta^R f = -\Delta^H f = -(-\star\,\mathbf{d}\star)\mathbf{d}f = -\boldsymbol{\delta}\mathbf{d}f.$$

The $\Delta^R = \mathrm{div}(\mathrm{grad}(\cdot))$ denotes the rough-Laplacian given by the generalization of the divergence applied to the gradient as in vector calculus. For vector fields, $\Delta^H(\mathbf{F})$ denotes the Hodge-de Rham Laplacian, which has similarities as taking the curl of the curl [80]. In fact, in the case that $\mathrm{div}(\mathbf{F}) = -\boldsymbol{\delta}\mathbf{F}^\flat = 0$ we have $-\Delta^H(\mathbf{F}) = \Delta^S(\mathbf{F}) = \left[-\boldsymbol{\delta}\mathbf{d}\mathbf{F}^\flat\right]^\sharp$. We remark by conventions adopted in differential geometry the Hodge-de Rham Laplacian has the opposite sign when reduced in the Euclidean case for comparison to the Laplacian of vector calculus. As a consequence, while the Laplacian is a negative semi-definite operator, in contrast the Hodge-de Rham Laplacian is a positive semi-definite operator. These conventions are important to consider when formulating physical models and numerical calculations utilizing operators and results from differential geometry.

When working with mechanical systems involving manifolds embedded within an ambient space and when working with coordinates it is useful to summarize briefly a few definitions and results from differential geometry. A more detailed discussion can be found in [28, 80]. When working in coordinates in an embedding space, the Christoffel symbols Γ^c_{ab} of the manifold can be viewed as serving to represent the rate-of-change of the tangent space basis vectors $\mathbf{e}_a = \partial_{x^a}$ as $\frac{\partial \mathbf{e}_a}{\partial x^b} = \Gamma^c_{ab}\mathbf{e}_c$. A more geometrically intrinsic definition without reference to an embedding space can be given in terms of the metric as

$$\Gamma^c_{ab} = \frac{1}{2}g^{ck}\left(\frac{\partial g_{ak}}{\partial x^b} + \frac{\partial g_{kb}}{\partial x^a} - \frac{\partial g_{ab}}{\partial x^k}\right). \tag{2.2.3}$$

We can define a covariant derivative connecting tangent spaces as

$$\nabla_{\mathbf{v}}\mathbf{w} = \left(\frac{\partial w^c}{\partial x^b}v^b + \Gamma^c_{ab}v^a w^b\right)\mathbf{e}_c. \tag{2.2.4}$$

When $\mathbf{w} = w^a\mathbf{e}_a = w^a\partial_{x^a}$ we denote this in components as $w^c_{|b}$ so that $\nabla_{\mathbf{e}_b}\mathbf{w} = w^c_{|b}\mathbf{e}_c$. We can define a covariant divergence as $\overline{\mathrm{div}}(\mathbf{w}) = w^b_{|b}$. We often will consider motions $\phi_t : \mathcal{B} \to \mathcal{S}$ of a manifold with reference body $\mathcal{B}$ mapped to a configuration in an embedding space $\mathcal{S}$. We define the flow $\phi_{t,s}$ of a motion starting at time t and ending at time s as $\phi_{t,s} = \phi_s \circ \phi_t^{-1}$. The associated velocity of the flow is given by a velocity field $\mathbf{v}$ with $\mathbf{v}(\mathbf{x}) = \frac{d}{ds}(\phi_{t,s}\mathbf{x})\big|_{s=t}$. The Lie derivative of a tensor under the flow is defined as

$$L_{\mathbf{v}}\mathbf{t} = \frac{d}{ds}\left(\phi^*_{t,s}\mathbf{t}\right)\big|_{s=t}. \tag{2.2.5}$$

The $\phi^*_{t,s}$ is the pull-back [80]. In the case of the tensor $\mathbf{t}$ is a vector field $\mathbf{t} = \mathbf{w}$ we have that the Lie derivative generalizes the material derivative as

$$\frac{D\mathbf{w}}{Dt} := L_{\mathbf{v}}\mathbf{w} = \partial_t \mathbf{w} + \nabla_{\mathbf{v}}\mathbf{w}. \tag{2.2.6}$$

We emphasize that $\nabla_{\mathbf{v}}$ is now the covariant derivative of equation 2.2.4. We also discuss additional results and relations in our prior work [5]. A more detailed discussion of continuum mechanics and differential geometry also can be found in [28, 80].

Lastly, the exterior calculus provides generalizations of the Stokes Theorem and the Divergence Theorem to manifolds. These take the form respectively

$$\int_{\partial\Omega} \omega = \int_{\Omega} \mathbf{d}\omega, \qquad \int_{\partial\Omega} \star\omega = \int_{\Omega} \mathbf{d} \star \omega. \tag{2.2.7}$$

The ω is a k-form and Ω denotes a general smooth domain with smooth boundary $\partial\Omega$ within the manifold. When Ω is in two dimensions and ω is a 1-form, the integrals on the left-hand-side perform a type of line integral over the boundary contour $\partial\Omega$. For the Stokes Theorem the component of the vector field that is tangent to the contour is integrated. For the Divergence Theorem the Hodge star $\star$ ensures that only the component of the vector field that is normal to the contour is integrated. The right-hand side then integrates over the interior region of Ω. For the Stokes Theorem $\mathbf{d}\omega$ corresponds to a generalized representation of the curl operation. For the Divergence Theorem $\mathbf{d} \star \omega$ provides a representation of the divergence. We emphasize the sign of $\star\omega$ which was chosen in order to

represent fluxes with respect to outward normals using the 1-form ω. Additional applications of the Hodge star $\star$ and isomorphisms $\flat$, $\sharp$ can also be useful to make conversions that bring these expressions into closer agreement with the standard vector calculus interpretations and intuition. Notice the relation of these expressions when $\omega = \mathbf{F}^\flat$ to equation 2.2.1. A useful feature of equation 2.2.7 is that it also generalizes readily to higher dimensions and k-forms.

2.3 Expressing Exterior Calculus Operators on 2-Manifolds

By restricting ourselves to 2-manifolds, we can simplify many of the exterior calculus expressions we introduced in Einstein notation. We additionally make use of the fact that computing the inverse of a 2 x 2 matrix is simple to express. Once we compute these expressions for arbitrary 2-d coordinates, it is relatively simple to substitute the particular coordinates we use to parametrize our manifolds in our various solvers.

The scalar Laplace-Beltrami operator $\Delta_{LB} = -\boldsymbol{\delta}\mathbf{d}$ that acts on 0-forms can be expressed in coordinates as

$$\Delta_{LB} = \frac{1}{\sqrt{|g|}}\partial_i \left(g^{ij}\sqrt{|g|}\partial_j \right). \tag{2.3.1}$$

The g_{ij} denotes the metric tensor, g^{ij} the inverse metric tensor, and $|g|$ the determinant of the metric tensor. To decompose the Laplace-Beltrami operator

we find it useful to represent it as a combination of terms h_{ij}

$$h_{ij} = \left(\sqrt{|g|}g^{ij}\right)\partial_{ij} + \left(\partial_i\sqrt{|g|}g^{ij}\right)\partial_j. \tag{2.3.2}$$

We obtain $\Delta_{LB} = (1/\sqrt{|g|})\sum_{ij} h_{ij}$. The decomposition into h_{ij} is particularly helpful since this makes more transparent the terms which pose in practice the most challenges in numerical calculations.

To help elucidate these operator expressions we consider the coordinates $(x_1, x_2) = (\theta, \phi)$, so $\partial_1 = \partial_\theta$ and $\partial_2 = \partial_\phi$. This aligns with the Chart A coordinates for radial manifolds, described in Chapter 3, although these results hold for any smooth Riemanian 2-manifold.

This allows us to compute analytically many of the terms that arise involving the metric and exterior operators. Using that the manifolds are two dimensional with coordinates (θ, ϕ) we have from the formula for a two-by-two inverse matrix that

$$\sqrt{|g|}g^{ij} = \begin{cases} g_{\phi\phi}/\sqrt{|g|} & \text{if: } i = j = \theta \\ g_{\theta\theta}/\sqrt{|g|} & \text{if: } i = j = \phi \\ -g_{\theta\phi}/\sqrt{|g|} = -g_{\phi\theta}/\sqrt{|g|} & \text{if: } i \neq j. \end{cases} \tag{2.3.3}$$

In the radial manifold case, we can compute each of these terms in the expression in equation 2.3.3.

The exterior derivatives can be expressed for a 0-form f and 1-form $\boldsymbol{\alpha}$ as

$$\mathbf{d}f = (\partial_\theta f)\mathbf{d}\theta + (\partial_\phi f)\mathbf{d}\phi = f_\theta \mathbf{d}\theta + f_\phi \mathbf{d}\phi \tag{2.3.4}$$

$$\mathbf{d}\alpha = (\partial_\theta \alpha_\phi - \partial_\phi \alpha_\theta)\mathbf{d}\theta \wedge \mathbf{d}\phi. \tag{2.3.5}$$

The generalized curl on the radial manifold of a 0-form and 1-form can be expressed as

$$-\star\,\mathbf{d}f = \mathrm{curl}_{\mathcal{M}}(f) = \sqrt{|g|}(f_\theta g^{\theta\phi} + f_\phi g^{\phi\phi})\mathbf{d}\theta - \sqrt{|g|}(f_\theta g^{\theta\theta} + f_\phi g^{\phi\theta})\mathbf{d}\phi \tag{2.3.6}$$

$$-\star\,\mathbf{d}\alpha = \mathrm{curl}_{\mathcal{M}}(\boldsymbol{\alpha}) = \frac{\partial_\phi \alpha_\theta - \partial_\theta \alpha_\phi}{\sqrt{|g|}}. \tag{2.3.7}$$

In this notation we have taken the conventions that $f_j = \partial_{x^j} f$ and α_j such that $\boldsymbol{\alpha} = \alpha_j \mathbf{d}x^j$ where $j \in \{\theta, \phi\}$. The isomorphisms $\sharp$ and $\flat$ between vectors and co-vectors can be expressed explicitly as

$$\begin{aligned} \mathbf{v}^\flat &= (v^\theta \boldsymbol{\sigma}_\theta + v^\phi \boldsymbol{\sigma}_\phi)^\flat \\ &= v^\theta g_{\theta\theta}\mathbf{d}\theta + v^\theta g_{\theta\phi}\mathbf{d}\phi + v^\phi g_{\phi\theta}\mathbf{d}\theta + v^\phi g_{\phi\phi}\mathbf{d}\phi \\ &= (v^\theta g_{\theta\theta} + v^\phi g_{\phi\theta})\mathbf{d}\theta + (v^\theta g_{\theta\phi} + v^\phi g_{\phi\phi})\mathbf{d}\phi \end{aligned} \tag{2.3.8}$$

$$\begin{aligned} (\boldsymbol{\alpha})^\sharp &= (\alpha_\theta \mathbf{d}\theta + \alpha_\phi \mathbf{d}\phi)^\sharp \\ &= \alpha_\theta g^{\theta\theta}\boldsymbol{\sigma}_\theta + \alpha_\theta g^{\theta\phi}\boldsymbol{\sigma}_\phi + \alpha_\phi g^{\phi\theta}\boldsymbol{\sigma}_\theta + \alpha_\phi g^{\phi\phi}\boldsymbol{\sigma}_\phi \\ &= (\alpha_\theta g^{\theta\theta} + \alpha_\phi g^{\phi\theta})\boldsymbol{\sigma}_\theta + (\alpha_\theta g^{\theta\phi} + \alpha_\phi g^{\phi\phi})\boldsymbol{\sigma}_\phi \end{aligned} \tag{2.3.9}$$

We use the notational conventions here that for the embedding map $\boldsymbol{\sigma}$ we have $\boldsymbol{\sigma}_\theta = \partial_\theta$ and $\boldsymbol{\sigma}_\phi = \partial_\phi$. Combining the above equations we can express the

generalized curl as

$$\begin{aligned}(-\star\,\mathbf{d}f)^{\sharp} &= ([\sqrt{|g|}(f_\theta g^{\theta\phi}+f_\phi g^{\phi\phi})]g^{\theta\theta}+[-\sqrt{|g|}(f_\theta g^{\theta\theta}+f_\phi g^{\phi\theta})]g^{\phi\theta})\boldsymbol{\sigma}_\theta \\ &+ ([\sqrt{|g|}(f_\theta g^{\theta\phi}+f_\phi g^{\phi\phi})]g^{\theta\phi}+[-\sqrt{|g|}(f_\theta g^{\theta\theta}+f_\phi g^{\phi\theta})]g^{\phi\phi})\boldsymbol{\sigma}_\phi \\ &= \frac{f_\phi}{\sqrt{|g|}}\boldsymbol{\sigma}_\theta-\frac{f_\theta}{\sqrt{|g|}}\boldsymbol{\sigma}_\phi\end{aligned} \tag{2.3.10}$$

$$-\star\,\mathbf{d}\mathbf{v}^{\flat} = \frac{\partial_\phi(v^\theta g_{\theta\theta}+v^\phi g_{\phi\theta})-\partial_\theta(v^\theta g_{\theta\phi}+v^\phi g_{\phi\phi})}{\sqrt{|g|}}. \tag{2.3.11}$$

Additional details and discussions of these operators also can be found in and in [4, 80, 3].

2.4 Continuum Mechanics and Conservation Laws on Manifolds

We discuss briefly how we formulate continuum mechanics in the covariant form on curved surfaces and more general manifolds. We use the exterior calculus concepts discussed in Section 2.1 to derive hydrodynamic equations for curved fluid interfaces.

There are a few different ways that one can attempt to develop the equations of continuum mechanics in the setting of manifolds. One approach is to try to use the embedding space with local coordinates and a change of variables. This can become quite tedious and we shall try to avoid coordinate calculations

to the extent it is possible. By using an exterior calculus formulation of the hydrodynamics we can abstract away in our derivations and analysis many of the details related to intricacies of computing with specific coordinates and tensors in curved spaces. This allows us to generalize more readily many of the techniques employed in fluid mechanics to the manifold setting. This approach also helps in revealing geometric features of the equations and the continuum mechanics.

We instead use an approach related to the Green-Rivlin-Naghdi Theorem [112] which is based on the use of energy balance and invariance of physical laws under symmetries to derive the conservation equations for mass, momentum, and angular momentum [28, 31, 51]. We remark this approach also provides some insights into why these physical laws manifest in some ways differently in curved manifolds relative to the Euclidean case.

As a starting point we consider a generalization of the Reynold's transport theorem to the setting of a manifold. This allows us to express how an integral over a moving parcel of material transforms over time in the Eulerian reference frame. For a k-dimensional domain consider the k-form $\boldsymbol{\alpha}$. We have from properties of differential forms and the pull-back that

$$\frac{\partial}{\partial s}\int_{\phi_s(\mathcal{U})}\boldsymbol{\alpha}\;\Big|_{s=t} = \int_{\phi_s(\mathcal{U})}\frac{d}{ds}\left(\phi_{t,s}^*\boldsymbol{\alpha}\right)\;\Big|_{s=t} = \int_{\phi_t(\mathcal{U})} L_{\mathbf{v}}\boldsymbol{\alpha}. \tag{2.4.1}$$

The $\phi_{t,s}(\mathbf{x}) = \phi_s(\phi_t^{-1}(\mathbf{x}))$ denotes the change in configuration from time t to time $s > t$.

In the special case when $\boldsymbol{\alpha} = f dv$, where $dv = \omega$ is the volume differential form, we have the Lie derivative is $L_{\mathbf{v}} = \dot{f} + \operatorname{div}(f\mathbf{v})$ where $\dot{f} = \partial f/\partial t + \mathbf{v}[f]$ where for short we denote by $\mathbf{v}[f] = (\mathbf{d}f)[\mathbf{v}]$. We also emphasize that the divergence operator for a vector field on the manifold is now $\operatorname{div}(\mathbf{w}) = w^b_{|b}$ where in coordinates the $w^a_{|b}$ denotes the covariant derivative component corresponding to derivatives in the direction ∂_{x^b}. This gives the scalar transport theorem

$$\frac{\partial}{\partial t}\int_{\phi_t(\mathcal{U})} f dv = \int_{\phi_t(\mathcal{U})} \dot{f} + \operatorname{div}(f\mathbf{v}). \tag{2.4.2}$$

This can be further specialized in the case of a hypersurface where $\mathcal{U} \subset \mathcal{B}$ and $\dim \mathcal{S} = \dim \mathcal{B}+1$. In this case we have for $\phi_t(\mathcal{U}) \subset \mathcal{S}$ the surface-scalar transport theorem

$$\frac{\partial}{\partial t}\int_{\phi_t(\mathcal{U})} f dv = \int_{\phi_t(\mathcal{U})} \left(\dot{f} + f\left(\overline{\operatorname{div}}\left(\mathbf{v}_{\|}\right) + \mathbf{v}_n H\right)\right) dv. \tag{2.4.3}$$

The H denote the mean-curvature of the manifold describing the configuration of the surface [4]. The $\mathbf{v} = \mathbf{v}_{\|} + v_n\mathbf{n}$ where $\mathbf{v}_n = v_n\mathbf{n}$ gives the velocity component normal to the surface in the ambient space. Here the $\overline{\operatorname{div}}$ denotes the covariant divergence in the manifold describing the surface. In coordinates aligned with the surface this would be $\overline{\operatorname{div}(\mathbf{w})} = w^a_{|a}$ where now the indices a are restricted only over directions ∂_{x^a} corresponding to the components tangent to the surface. We again emphasize that mechanics requires use of some structure of the ambient physical space in order to make sense of physical quantities such as momentum of the surface [28]. We shall avoid in our derivation the need to integrate vector

fields over the manifold with explicit reference to the ambient space by considering how the mechanics arises from an energy balance principle. This involves the integration and use of transport theorems only for scalar fields. We can express the balance of energy for a mechanical system in the general manifold setting as

$$\frac{\partial}{\partial t}\int_{\phi_t(\mathcal{U})}\rho\left(e+\frac{1}{2}\left\langle \mathbf{v},\mathbf{v}\right\rangle\right)dv=\int_{\phi_t(\mathcal{U})}\rho\left\langle \bar{\mathbf{b}},\mathbf{v}\right\rangle dv+\int_{\partial\phi_t(\mathcal{U})}\left\langle \mathbf{t},\mathbf{v}\right\rangle . \tag{2.4.4}$$

The e denotes the energy density per unit mass, $\rho\mathbf{v}$ the momentum density, $\rho\bar{\mathbf{b}}$ the body force, and $\mathbf{t}=\boldsymbol{\sigma}[\mathbf{n}]$ the internal material traction stress vector. This describes the rate at which the total energy (potential + kinetic) is changing in the system as a consequence of mechanical work done by the body force and stresses. We point out that the structure of the ambient physical space is still playing a role but now is contained within the inner-products that appear in equation 2.4.4 given in equation 2.1.3.

We now use augmentations of the motion ϕ_t by diffeomorphisms ξ_t to obtain a new motion $\tilde{\phi}_t=\xi_t\circ\phi_t$. Since the mechanics associated with any steady translational motion should adhere to Galilean invariance [113], we have the new motion $\tilde{\phi}_t$ should satisfy the same energy balance as in equation 2.4.4. We can also consider how the energy principle transforms under other motions such as steady rotational motion which while non-inertial does preserve distances within the material. From these considerations, we consider how the energy transforms under the augmented motions $\tilde{\phi}_t$ with diffeomorphisms

$$\xi_t(\mathbf{x})=\mathbf{x}+(t-t_0)\mathbf{c}\quad\text{ or }\quad\xi_t(\mathbf{x})=\exp\left((t-t_0)\boldsymbol{\Omega}\right)\mathbf{x}. \tag{2.4.5}$$

The $\mathbf{c}$ is the steady translational velocity and $\mathbf{\Omega}$ is any anti-symmetric matrix giving the steady angular velocity when we express the rotation as $\mathbf{R}(t) = \exp\left((t - t_0)\mathbf{\Omega}\right)$.

Under the new motion $\tilde{\phi}_t$ in the translational case, we have again that equation 2.4.4 holds when we substitute in the quantities $\tilde{\phi}_t$, $\tilde{e}(x,t) = e(x,t)$, $\tilde{\rho}(x,t) = \rho(x,t)$, $\tilde{\mathbf{v}} = \mathbf{v} + \mathbf{c}$, $\tilde{\mathbf{b}} = \mathbf{b} + \mathbf{a}$, $\tilde{\mathbf{t}} = T\xi_t \mathbf{t}$. The $T\xi_t$ denotes the tangent map also equivalently the push-forward of ξ_t [80]. The $\mathbf{a} = \dot{\mathbf{v}} = \partial_t \mathbf{v} + \nabla_{\mathbf{v}} \mathbf{v}$ is the acceleration expressed in Eulerian reference frame with $\nabla_{\mathbf{v}}$ the covariant derivative of equation 2.2.4. We use the result of the surface-transport theorem given in equation 2.4.3 and subtract the original energy balance equation 2.4.4. At time $t = t_0$ we have that $\xi_{t_0} = \mathrm{id}$ and the terms of the energy balance remaining from the difference between the motions is

$$\int_{\phi_t(\mathcal{U})} \left(\dot{\rho} + \rho\left(\overline{\mathrm{div}}\left(\mathbf{v}_{\|}\right) + \mathbf{v}_n H\right)\right)\left(\langle \mathbf{v}, \mathbf{c}\rangle + \frac{1}{2}\langle \mathbf{c}, \mathbf{c}\rangle\right) dv \qquad (2.4.6)$$
$$= \int_{\phi_t(\mathcal{U})} \langle \rho(\mathbf{b} - \mathbf{a} + \overline{\mathrm{div}}(\boldsymbol{\sigma}), \mathbf{c}\rangle dv.$$

This must hold for all choices of $\mathbf{c}$. To obtain this expression we also used the divergence theorem so that the contributions of the stress vector $\mathbf{t}$ over the boundary $\partial\phi_t(\mathcal{U})$ can be expressed in terms of integration of the divergence of the stress $\boldsymbol{\sigma}$ over the volume. Since $\mathcal{U}$ is arbitrary and if we take $\mathbf{c} = q\tilde{\mathbf{c}}$, the equation 2.4.6 can be localized to a point-wise statement relating the integrands. We remark localization does require integrands to be sufficiently smooth which we shall assume throughout. By dividing both sides by q^2 and taking the limit

$q \to \infty$ we have that only the quadratic term $\frac{1}{2}\langle \tilde{\mathbf{c}}, \tilde{\mathbf{c}} \rangle$ persists with all other terms on both sides going to zero. This requires the multiplying factor of the quadratic term involving $\tilde{\mathbf{c}}$ to vanish since all the other terms are zero. This yields the equations for conservation of mass on the surface

$$\dot{\rho} + \rho \left(\overline{\operatorname{div}} \left(\mathbf{v}_{\|} \right) + \mathbf{v}_n H \right). \tag{2.4.7}$$

We can use this result to further simplify equation 2.4.6 to obtain

$$0 = \int_{\phi_t(\mathcal{U})} \langle \rho(\mathbf{b} - \mathbf{a} + \operatorname{div}(\boldsymbol{\sigma}), \mathbf{c} \rangle dv. \tag{2.4.8}$$

Since $\mathbf{c}$ and $\mathcal{U}$ are arbitrary this gives the equations for conservation of momentum on the surface

$$\rho \dot{\mathbf{v}} = \overline{\operatorname{div}} \left(\boldsymbol{\sigma} \right) + \rho \mathbf{b}. \tag{2.4.9}$$

We use here that $\mathbf{a} = \rho \dot{\mathbf{v}} = \rho(\partial_t \mathbf{v} + \nabla_{\mathbf{v}} \mathbf{v})$ gives the acceleration in the Eulerian reference frame with $\nabla_{\mathbf{v}}$ the covariant derivative of equation 2.2.4. We can similarly use the transformation under the rotational motions given by the second diffeomorphism in equation 2.4.5 to get the conservation of angular momentum. This has the important consequence that the stress tensor $\boldsymbol{\sigma}$ must be symmetric in the sense $\sigma^{ab} = \sigma^{ba}$.

These derivations help us to formulate the proper conservation equations of continuum mechanics in the manifold setting. Similar techniques have also be used to derive other equations useful in elasticity and in constitutive modeling

in [28, 31, 52, 51]. We can already see that conservation of mass has some interesting features quite distinct from the flat Euclidean setting, see equation 2.4.7. While the momentum equations appear to look superficially similar to the Euclidean setting, it is important to emphasize that the divergence operator $\overline{\text{div}}$ is based on covariant derivatives having in fact quite distinct behaviors from local curvature than the Euclidean setting. We shall see these results have a number of interesting consequences for constutitive laws, such as the proper form for modeling surface Newtonian fluids for a curved interface.

2.5 A Covariant Stokes Equation

We would like to formulate in a covariant manner the equations of hydrodynamics in the case of a fluid interface that is an incompressible Newtonian fluid [6]. Using our results from Section 2.4 we can express the conservation of mass and momentum as

$$\begin{cases} \rho\dot{\mathbf{v}} &= \overline{\text{div}}\,(\boldsymbol{\sigma}) + \rho\bar{\mathbf{b}} \\ \dot{\rho} + \rho\left(\overline{\text{div}}\,(\mathbf{v}_{\|}) + \mathbf{v}_n H\right) &= 0. \end{cases} \tag{2.5.1}$$

We focus here on the the steady-state hydrodynamics of incompressible Newtonian fluids within a curved surface of fixed shape. This corresponds to $\overline{\text{div}}\,(\mathbf{v}_{\|}) = 0$ and $\mathbf{v}_n = 0$. From equation 2.5.1, this yields that $\dot{\rho} = 0$ corresponding to a constant mass density $\rho = \rho_0$ within the interface. The steady-state hydrodynamics

corresponds to the case with $\rho\dot{\mathbf{v}} = 0$ reducing equation 2.5.1 to the conditions

$$\begin{cases} \overline{\mathrm{div}}\,(\boldsymbol{\sigma}) &= -\mathbf{b} \\ \overline{\mathrm{div}}\,(\mathbf{v}) &= 0. \end{cases} \tag{2.5.2}$$

In the notation, we take throughout $\mathbf{b} = \rho_0\bar{\mathbf{b}}$ and $\mathbf{v} = \mathbf{v}_{\|}$ since we shall consider only incompressible fluid flows where the velocity is tangent to the surface. For an incompressible Newtonian fluid the constitutive law should depend on the local rate of deformation $\mathbf{D}$ of the material as $\boldsymbol{\sigma} = \mu_m\mathbf{D} - p\mathcal{I}$. The p corresponds to the pressure which acts as a Lagrange multiplier imposing incompressibility. The μ_m corresponds to the dynamic shear viscosity of the interfacial fluid. The $\mathcal{I}$ is the metric associated identity operator. The rate-of-deformation tensor is $\mathbf{D} = \frac{1}{2}\partial\mathbf{C}/\partial t$ where $\mathbf{C}$ is the right-Cauchy-Green Tensor associated with the motion ϕ_t [28]. We can express the rate-of-deformation tensor in terms of the covariant derivative as $D_{ab} = v_{a|b} + v_{b|a}$. For a two-dimensional incompressible fluid having a velocity field that is always tangent to the curved surface, we have $\overline{\mathrm{div}}(\mathbf{D})^\flat = -\boldsymbol{\delta}\mathbf{d}\mathbf{v}^\flat + 2K\mathbf{v}^\flat$ [114, 6, 53]. We can further express the divergence in covariant form and exterior calculus operations as $\overline{\mathrm{div}}\,(\mathbf{v})^\flat = -\boldsymbol{\delta}\mathbf{v}^\flat$. From equation 2.2.1 we have $\overline{\mathrm{div}}(p\mathcal{I})^\flat = \mathbf{d}p$. This allows us to express the Stokes hydrodynamic equations in covariant form as

$$\begin{cases} \mu_m\left(-\boldsymbol{\delta}\mathbf{d}\mathbf{v}^\flat + 2K\mathbf{v}^\flat\right) - \gamma\mathbf{v}^\flat - \mathbf{d}p &= -\mathbf{b}^\flat \\ -\boldsymbol{\delta}\mathbf{v}^\flat &= 0. \end{cases} \tag{2.5.3}$$

We also added to this equation a phenomenological drag term $-\gamma\mathbf{v}^\flat$ which acts as a force density to model the coupling of the fluid flow on the surface to the

bulk three-dimensional surrounding fluid. This has been done in the context of interfaces such as flat lipid membranes in [115] and for bulk external flows for spherical geometry in [6]. Having some form of dissipative tractional stress is important with the surrounding bulk fluid since it provides a model of the physical processes necessary to surppress the otherwise well-known Stokes paradox that arises in purely two-dimensional fluid equations [116, 117]. Of course this model is only approximate and one could of course consider more sophisticated hydrodynamic coupling models [118, 119]. For specialized cases, such as flat interfaces or spherical geometry, the traction coupling with the bulk fluid flow can be worked out in detail analytically or through asymptotic approximations as done in [118, 119, 6, 120, 53]. In the more general setting, solution for the surrounding three-dimensional bulk flow is typically difficult to obtain analytically requiring instead development of separate numerical solvers. While incorporating such a solver into our approaches is conceptually relatively straight-forward, in practice it involves some significant investments for implementation and handling additional technical issues. Here we focus solely develping solvers for the surface part of the hydrodynamics.

2.6 Recasting Our Stokes Equation Using the Hodge Decomposition

We use a surface Hodge decomposition to derive a formulation of the hydrodynamics that handles the incompressibility constraint for the flow field. For a fluid within a general manifold we can express the Hodge decomposition using the exterior calculus as

$$\mathbf{v}^\flat = \mathbf{d}\psi + \boldsymbol{\delta}\phi + \mathbf{h}. \tag{2.6.1}$$

The ψ is a 0-form, ϕ is a 2-form, and $\mathbf{h}$ is a harmonic 1-form on the surface with respect to the Hodge Laplacian $\Delta_H \mathbf{h} = (\boldsymbol{\delta}\mathbf{d} + \mathbf{d}\boldsymbol{\delta})\,\mathbf{h} = 0$. The dimensionality of the null-space of the Hodge Laplacian depends on the topology of the manifold [81]. As a consequence, we have for different topologies that the richness of the harmonic differential forms $\mathbf{h}$ appearing in equation 2.6.1 will vary. Fortunately, in the case of spherical topology the surface admits only the trivial harmonic 1-forms $\mathbf{h} = \mathbf{0}$ making this manifold relatively easy to deal with in our physical descriptions. The incompressibility constraint when applied to equation 2.6.1 results in $\boldsymbol{\delta}\mathbf{v}^\flat = \boldsymbol{\delta}\mathbf{d}\psi = \Delta_H\psi = 0$ which for spherical topology requires $\psi = C$ and $\mathbf{d}\psi = 0$. Thus, for an incompressible hydrodynamic flow on manifolds with spherical topology our physical description must be of the form

$$\mathbf{v}^\flat = \boldsymbol{\delta}\phi + \mathbf{v}_0^\flat. \tag{2.6.2}$$

Here we have added a velocity $\mathbf{v}_0$ since this corresponds to the non-tangent contributions from rigid-body translational and rotational motions of the entire interface within the physical ambient space. This can arise physically when the surface force density has a non-zero total net force or torque. We take throughout the paper the simplification $\mathbf{v}_0 = 0$ so that the surface velocities should be viewed as accounting for the in-plane contributions of the interface motions. Of course the flow field in other reference frames can be recovered by adding the non-tangent $\mathbf{v}_0$ velocity field at each location on the surface.

Using the Hodge decomposition in equation 2.6.2, we see that ϕ is a 2-form on the two-dimensional surface. We find it convenient to express ϕ in terms of a 0-form using the Hodge star to obtain $\Phi = - \star \phi$. Using the identities of the Hodge star discussed in Section 2.1, we can express the hydrodynamic flow field as

$$\mathbf{v}^\flat = - \star \mathbf{d}\Phi. \tag{2.6.3}$$

This can be related to classical methods in fluid mechanics by viewing the operator $- \star \mathbf{d}$ as a type of curl operator that is now generalized to the manifold setting. The Φ serves the role of a vector potential for the flow [116, 117, 119]. The velocity field of the hydrodynamic flows $\mathbf{v}$ is recovered from the vector potential Φ as $\mathbf{v}^\flat = - \star \mathbf{d}\Phi$. We obtain the velocity field $\mathbf{v} = \mathbf{v}^\sharp = (- \star \mathbf{d}\Phi)^\sharp$ using equation 2.3.10. Similarly from the force density $\mathbf{b}$ acting on the fluid, we obtain the data $- \star \mathbf{d}\mathbf{b}^\flat$ for the vector potential formulation of the hydrodynamics in

equation 2.6.4 using equation 2.3.11. We substitute equation 2.6.3 into equation 2.5.3 and apply the generalized curl operator $\text{curl}_{\mathcal{M}} = -\star\mathbf{d}$ to both sides to express the fluid equations on the surface as

$$\mu_m\bar{\Delta}^2\Phi - \gamma\bar{\Delta}\Phi + 2\mu_m(-\star\,\mathbf{d}(K(-\star\,\mathbf{d})))\Phi \;\; = \;\; \star\mathbf{d}\mathbf{b}^\flat. \tag{2.6.4}$$

This provides a particularly convenient form for the fluid equations since it only involves a scalar field on the surface. We shall utilize primarily this form of the hydrodynamic equations in our numerical methods.

We mention here the importance of distinguishing between the operators when acting on the 0-forms Φ in equation 2.6.4 in contrast to the operators acting on 1-forms $\mathbf{v}^\flat$ in equation 2.5.3. In our notation here we use $\bar{\Delta} = -\boldsymbol{\delta}_1\mathbf{d}_0$ to obtain our surface Laplacian. The sign convention ensures our surface Laplacian is a negative semidefinite operator. This provides consistency with intuition that is often used in physical setting and agreement with the standard Laplacian of vector calculus encountered in the Euclidean case. This is in contrast with the Hodge-Laplacian $\Delta_H = \boldsymbol{\delta}\mathbf{d} + \mathbf{d}\boldsymbol{\delta}$ used in differential geometry which is positive semi-definite [81, 80]. Our sign conventions also ensure that our operator $\bar{\Delta}$ is in agreement with the Laplace-Beltrami operator on the surface. Further distinctions can also arise when interpreting $\mathbf{d}$ and $\boldsymbol{\delta}$ depending on the dimensionality of the manifold and the order k of the k-forms on which the operator acts [80]. We mention these distinctions since in our experience in practice these differences and the sign conventions can become a significant source of book-keeping

and confusion in modeling and in numerical methods. We have found it convenient when formulating our numerical methods and performing implementations to use the Hodge-Laplacian $\Delta_H = -\bar{\Delta} = \boldsymbol{\delta}_1 \mathbf{d}_0$ to avoid carrying around the sign. However, we have found it convenient in our physical analysis and discussions to use the negative semi-definite surface Laplacian $\bar{\Delta}$ as we have discussed for equation 2.6.4. Given these considerations, we shall primarily use $\bar{\Delta}$ throughout most of our discussions in this paper unless otherwise noted.

Chapter 3

Discretizing Exterior Calculus Operators on Radial Manifolds

We take an isogeometric approach based on the hyperinterpolation of spherical harmonics to represent the manifold geometry, differential forms, and related scalar and vector fields [121, 122, 123]. In hyperinterpolation, functions are oversampled to avoid many of the inherent issues associated with trying to design an optimal collection of nodes for Lagrange interpolation [122, 124, 125, 126]. This allows for functions to be approximated through L^2-orthogonal projections using exact quadratures up to a desired order [122, 127]. To achieve discretizations with favorable symmetry on the sphere, we use the nodes of Lebedev quadrature [2, 1]. This is in contrast to the more common approach of using samping points based on lattitude and longitude coordinates. While lattitude-longitude samplings have a computational advantage through fast transforms, the sampling points have poor symmetry and inhomogeneous distribution over the surface with many points clustering near the poles [128, 129, 130]. The Lebedev quadrature

points provide a more regular distribution on the surface. For a comperable number of points, the Lebedev sampling provides a more uniform resolution of functions [131]. The Lebedev quadrature points also have the feature of being invariant under rotations corresponding to octohedral symmetry [2, 1]. We show Lebedev nodes on example radial manifolds in Figure 3.1.

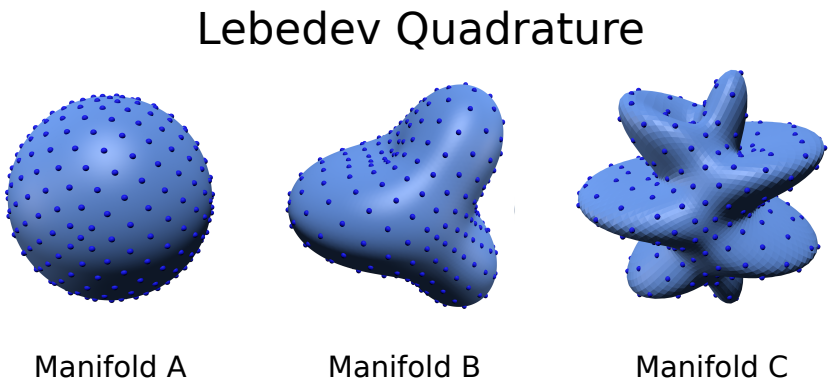

Figure 3.1: Lebedev Quadrature. Shown are the sample points of the Lebedev quadrature in the case of 302 nodes. The Lebedev nodes distribute nearly uniformly over the surface and are invariant under the rotations corresponding to octahedral symmetry [1, 2].

We briefly mention that recently there has also been some very interesting developments using Spherical Designs to perform quadratures of functions on spherical geometries [132]. Historically, a significant challenge has been to find realizations of the nodes for the Spherical Designs of specified order. With recent advances it has been found that Spherical Designs can be developed that perform comperably to Lebedev quadratures in practice [131]. We have chosen to use Lebedev quadratures in our current work presented given our initial familarity with them, more established results including guarentees on symmetry, and more

readily accessible weight-node data sets for exact integration for spherical harmonics up to high order [1, 2]. Recently promising methods have been developed to discover Spherical Designs yielding similar high levels of accuracy [132].

3.1 Radial Manifold Differential Geometry

We consider throughout manifolds of radial shape. A radial manifold is defined as a surface where each point can be connected by a line segment to the origin without intersecting the surface. In spherical coordinates, any point $\mathbf{x}$ on the radial manifold can be expressed as

$$\mathbf{x}(\theta, \phi) = \boldsymbol{\sigma}(\theta, \phi) = r(\theta, \phi)\mathbf{r}(\theta, \phi) \tag{3.1.1}$$

where $\mathbf{r}$ is the unit vector from the origin to the point on the sphere corresponding to angle θ, ϕ and r is a positive scalar function.

We take an isogeometric approach to representing the manifold M. We sample the scalar function r at the Lebedev nodes and represent the geometry using the finite spherical harmonics expansion $r(\theta, \phi) = \sum_i \bar{r}_i Y_i$ up to the order $\lfloor L/2 \rfloor$ where $\bar{r}_i = \langle r, Y_i \rangle_Q$ for a quadrature of order L. In this manner we have an analytic representation of the geometry allowing for fundamental operators to be computed.

Since there is no global non-singular coordinate system on a radial manifold surface, we ensure numerical accuracy by utilizing two coordinate charts. The

first is referred to as Chart A and has coordinate singularities at the north and south pole. The second is referred to as Chart B and has coordinate singularities at the east and west pole. For each chart we use spherical coordinates with $(\theta, \phi) \in [0, 2\pi) \times [0, \pi]$ but to avoid singularities only use values in the restricted range $\phi \in [\phi_{min}, \phi_{max}]$, where $0 < \phi_{min} \leq \frac{\pi}{4}$, and $\frac{3\pi}{4} \leq \phi_{max} < \pi$. In practice, one typically takes $\phi_{min} = 0.8 \times \frac{\pi}{4}$ and $\phi_{max} = 0.8 \times \pi$. To avoid issues with singularities when seeking a value at a point $\mathbf{x}$, we evaluate expressions within each chart in which $\mathbf{x}$ resides. If $\mathbf{x}$ resides in the restricted range of both charts, we simply pick one of the two evaluations to use in our calculations.

For Chart A, the manifold is parameterized in the embedding space $\mathbb{R}^3$ as

$$\mathbf{x}(\hat{\theta}, \hat{\phi}) = r(\hat{\theta}, \hat{\phi})\mathbf{r}(\hat{\theta}, \hat{\phi}),\ \mathbf{r}(\hat{\theta}, \hat{\phi}) = \Big[\sin(\hat{\phi})\cos(\hat{\theta}),\quad \sin(\hat{\phi})\sin(\hat{\theta}),\quad \cos(\hat{\phi})\Big] \tag{3.1.2}$$

and for Chart B

$$\mathbf{x}(\bar{\theta}, \bar{\phi}) = r(\bar{\theta}, \bar{\phi})\mathbf{r}(\bar{\theta}, \bar{\phi}),\ \bar{\mathbf{r}}(\bar{\theta}, \bar{\phi}) = \Big[\cos(\bar{\phi}),\quad \sin(\bar{\phi})\sin(\bar{\theta}),\quad -\sin(\bar{\phi})\cos(\bar{\theta})\Big] \tag{3.1.3}$$

With these coordinate representations, we can derive explicit expressions for geometric quantities associated with the manifold such as the metric tensor and shape tensor. Note that we give all expressions with generic polar coordinates (θ, ϕ) since the calculations are done the same manner in chart A and chart B. The derivatives used as the basis $\partial_\theta, \partial_\phi$ for the tangent space can be expressed as

$$\boldsymbol{\sigma}_\theta(\theta, \phi) = r_\theta(\theta, \phi)\mathbf{r}(\theta, \phi) + r(\theta, \phi)\mathbf{r}_\theta(\theta, \phi) \tag{3.1.4}$$

$$\boldsymbol{\sigma}_\phi(\theta, \phi) = r_\phi(\theta, \phi)\mathbf{r}(\theta, \phi) + r(\theta, \phi)\mathbf{r}_\phi(\theta, \phi). \tag{3.1.5}$$

We have expressions for $\mathbf{r}_\theta$ and $\mathbf{r}_\phi$ in the embedding space $\mathbb{R}^3$ using equation 3.1.2 or equation 3.1.3 depending on the chart being used. The first fundamental form $\mathbf{I}$ (metric tensor) and second fundamental form $\mathbf{II}$ (shape tensor) are given by

$$\mathbf{I} = \begin{bmatrix} E & F \\ F & G \end{bmatrix} = \begin{bmatrix} \boldsymbol{\sigma}_\theta \cdot \boldsymbol{\sigma}_\theta & \boldsymbol{\sigma}_\theta \cdot \boldsymbol{\sigma}_\phi \\ \boldsymbol{\sigma}_\phi \cdot \boldsymbol{\sigma}_\theta & \boldsymbol{\sigma}_\phi \cdot \boldsymbol{\sigma}_\phi \end{bmatrix} = \begin{bmatrix} r_\theta^2 + r^2 \sin(\phi)^2 & r_\theta r_\phi \\ r_\theta r_\phi & r_\phi^2 + r^2 \end{bmatrix}. \tag{3.1.6}$$

and

$$\mathbf{II} = \begin{bmatrix} L & M \\ N & N \end{bmatrix} = \begin{bmatrix} \boldsymbol{\sigma}_{\theta\theta} \cdot \boldsymbol{n} & \boldsymbol{\sigma}_{\theta\phi} \cdot \boldsymbol{n} \\ \boldsymbol{\sigma}_{\phi\theta} \cdot \boldsymbol{n} & \boldsymbol{\sigma}_{\phi\phi} \cdot \boldsymbol{n} \end{bmatrix}. \tag{3.1.7}$$

The $\mathbf{n}$ denotes the outward normal on the surface and is computed using

$$\boldsymbol{n}(\theta, \phi) = \frac{\boldsymbol{\sigma}_\theta(\theta, \phi) \times \boldsymbol{\sigma}_\phi(\theta, \phi)}{\|\boldsymbol{\sigma}_\theta(\theta, \phi) \times \boldsymbol{\sigma}_\phi(\theta, \phi)\|}. \tag{3.1.8}$$

The terms $\boldsymbol{\sigma}_{\theta\theta}$, $\boldsymbol{\sigma}_{\theta\phi}$, and $\boldsymbol{\sigma}_{\phi,\phi}$ are obtained by further differentiation from equation 3.1.4 and equation 3.1.5. We use the notation for the metric tensor $\mathbf{g} = \mathbf{I}$ interchangably. In practical calculations whenever we need to compute the action of the inverse metric tensor we do so through numerical linear algebra (Gaussian elimination with pivoting) [133, 134]. For notational convenience, we use the tensor notation for the metric tensor g_{ij} and its inverse g^{ij} which has the formal correspondence

$$g_{ij} = [\mathbf{I}]_{i,j}\,, \quad g^{ij} = \left[\mathbf{I}^{-1}\right]_{i,j}. \tag{3.1.9}$$

For the metric factor we also have that

$$\sqrt{|g|} = \sqrt{\det(\mathbf{I})} = r\sqrt{r_\theta^2 + (r_\phi^2 + r^2)\sin(\phi)^2} = \|\vec{\sigma}_\theta(\theta, \phi) \times \vec{\sigma}_\phi(\theta, \phi)\|. \tag{3.1.10}$$

To ensure accurate numerical calculations in each of the above expressions the appropriate coordinates either Chart A or Chart B are used to ensure sufficient distance from coordinate singularities at the poles. To compute quantities associated with curvature of the manifold we use the Weingarten map [4] which can be expressed as

$$\mathbf{W} = \mathbf{I}^{-1}\mathbf{II}. \tag{3.1.11}$$

To compute the Gaussian curvature K, we use

$$K(\theta, \phi) = \det\left(\mathbf{W}(\theta, \phi)\right). \tag{3.1.12}$$

For further discussion of the differential geometry of manifolds see [4, 80, 111].

3.2 Hyperinterpolation on Radial Manifolds

3.2.1 Spherical Harmonic Basis

The spherical harmonics are given by

$$Y_n^m(\theta, \phi) = \sqrt{\frac{(2n+1)(n-m)!}{4\pi(n+m)!}} P_n^m\left(\cos(\phi)\right) \exp\left(im\theta\right) \tag{3.2.1}$$

where m denotes the order and n the degree for $n \geq 0$ and $m \in \{-n, \ldots, n\}$. The P_n^m denote the *Associated Legendre Polynomials*. In our notation, θ denotes the azmuthal angle and ϕ the polar angle of the spherical coordinates [123].

Since we work throughout only with real-valued functions, we have that the modes are self-conjugate and we use that $Y_n^m = \overline{Y_n^{-m}}$. We have found it convenient to represent the spherical harmonics as

$$Y_n^m(\theta, \phi) = X_n^m(\theta, \phi) + iZ_n^m(\theta, \phi) \tag{3.2.2}$$

where X_n^m and Z_n^m denote the real and imaginary parts. In our numerical methods we use this splitting to construct a purely real set of basis functions on the unit sphere with maximum degree N. We remark that this consists of $(N+1)^2$ basis elements. In the case of $N = 2$ we have the basis elements

$$\begin{aligned} \tilde{Y}_1 = Y_0^0,\ \tilde{Y}_2 = Z_1^1,\ \tilde{Y}_3 = Y_1^0,\ \tilde{Y}_4 = X_1^1,\ \tilde{Y}_5 = Z_2^2,\ \tilde{Y}_6 = Z_2^1, \\ \tilde{Y}_7 = Y_2^0,\ \tilde{Y}_8 = X_2^1,\ \tilde{Y}_9 = X_2^2. \end{aligned} \tag{3.2.3}$$

We use a similar convention for the basis for the other values of N. We take our final basis elements Y_i to be the normalized as $Y_i = \tilde{Y}_i / \sqrt{\langle \tilde{Y}_i, \tilde{Y}_i \rangle}$.

We compute derivatives of our finite expansions by evaluating analytic formulas for the spherical harmonics in order to try to minimize approximation error [123]. Approximation errors are incurred when sampling the values of expressions involving these derivatives at the Lebedev nodes and performing quadratures. The derivative in the azmuthal coordinate θ of the spherical harmonics is given by

$$\partial_\theta Y_n^m(\theta, \phi) = \partial_\theta \sqrt{\frac{(2n+1)(n-m)!}{4\pi(n+m)!}} P_n^m(\cos(\phi)) \exp(im\theta) = imY_n^m(\theta, \phi).$$

This maps the spherical harmonic of degree n to again a spherical harmonic of degree n. In our numerics, this derivative can be represented in our finite basis which allows us to avoid projections. This allows for computing the derivative in θ without incurring an approximation error. For the derivative in the polar angle ϕ we have that

$$\partial_\phi Y_n^m(\theta,\phi) = m\cot(\phi)Y_n^m(\theta,\phi) + \sqrt{(n-m)(n+m+1)}\exp(-i\theta)\, Y_n^{m+1}(\theta,\phi). \tag{3.2.4}$$

We remark that the expression can not be represented in terms of a finite expansion of spherical harmonics. We use this expression for $\partial_\phi Y_n^m(\theta,\phi)$ when we compute values at the Lebedev quadrature nodes in equation 3.3.1. This provides a convenient way to compute derivatives of differential forms. We remark that it is the subsequent hyperinterpolation of the resulting expressions where the approximation error is incurred. We adopt the notational convention that $Y_n^m = 0$ when $m \geq n+1$. For further discussion of spherical harmonics see [123].

3.2.2 Lebedev Quadratures

The Lebedev quadrature nodes are derived by solving a non-linear system of equations that impose both exactness of integration on spherical harmonics up to a specified order while maintaining symmetry under octahedral rotations and reflections [1, 2]. One could also consider using a quadrature based on spherical coordinates and sampling on the latitudinal and longitudinal points

which have some computational advantages by using the Fast Fourier Transform [130, 135, 129]. However, these nodes have significant asymmetries with nodes forming dense clusters near the poles of the sphere, see Figure 3.2. We favor

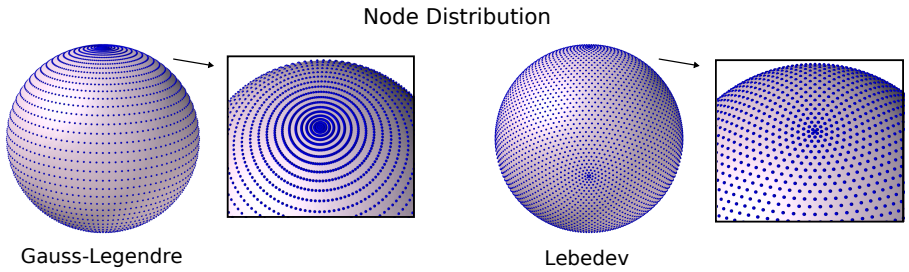

Figure 3.2: Node Distribution of the Gauss-Legendre Quadrature Compared to Lebedev Quadrature. We consider the Gauss-Legendre quadrature with 5886 nodes with a comparable Lebedev quadrature having 5810 nodes (113^{th} order of accuracy) [2]. We see that the Gauss-Legendre quadrature has dense clustering of points along latitudinal rings when approaching the north and south poles. We see that while the Lebedev quadrature has some clustering around a few points, these are less dense and overall exhibits sampling with a greater level of symmetry over the sphere.

Lebedev quadratures which while having some localized clustering at a few points exhibits overall a greater level of symmetry and less severe clustering. Quadrature on the surface of the sphere is still an active area of research with many recent results in the literature investigating the advantages and draw-backs of different methods depending on the intended use and application [124, 136, 137, 131]. We briefly mention that this includes recently introduced Spherical t-Designs [132] and nodes obtained by minimizing different types of energies motivated by generalizing the classical Thomson problem [138, 131]. The recently introduced

Spherical t-Designs are also attractive given their overall symmetry of quadrature nodes [132]. However, the Spherical t-Designs only have 60% approximation efficiency in the number of nodes per the accuracy achieved. In contrast the Lebedev quadratures achieve optimal approximation efficiency [131]. In principle, almost any quadrature on the sphere could be used within the overall numerical approaches we present. We use the Lebedev quadratures given their high level of symmetry and approximation efficiency.

3.2.3 Hyperinterpolation

We use hyperinterpolation to obtain a continuum approximation to fields on the manifold surface [122, 127]. To obtain a continuum representation of a function f on the surface, we perform an L^2-orthogonal projection $\mathcal{P}$ to the space spanned by spherical harmonics up to order $\lfloor L/2 \rfloor$,

$$\mathcal{P}[f] = \bar{f}(\theta, \phi) = \sum_i \hat{f}_i Y_i(\theta, \phi), \tag{3.2.5}$$

where $\hat{f}_i = \langle f, Y_i \rangle_Q$. We take the spherical harmonics Y_i to be normalized with $\langle Y_j, Y_i \rangle_Q = \delta_{ij}$. We use the discrete inner-product defined by

$$\langle u, v \rangle_Q = \sum_\ell w_\ell u(\mathbf{x}_\ell) v(\mathbf{x}_\ell). \tag{3.2.6}$$

where $w_\ell, \mathbf{x}_\ell$ are the Lebedev quadrature weights and nodes. When the quadrature is of order L and the functions u, v are each band-limited with respect to spherical harmonics up to order $\lfloor L/2 \rfloor$, the the inner-product is the same as the

L^2-inner-product $\langle u, v\rangle_Q = \langle u, v\rangle_{L^2}$. This yields the projection property $\mathcal{P}^2 = \mathcal{P}$, see equation 3.2.5.

In practice, computing the inner-product $\langle \cdot, \cdot \rangle_Q$ only requires we know values of f at the Lebedev nodes $\{\mathbf{x}_\ell\}$. This is utilized to represent functions on the surface in numerical calculations. We use this property to represent differential forms on the surface by an equivalent vector field at the Lebedev nodes. We perform in calculations conversions as needed by using the isomorphisms $\flat$, $\sharp$, as shown in Figure 2.1. In two dimensions the 0-forms and 2-forms on the surface are equivalent to scalar fields (a vector field with only one component). For the more interesting case of 1-forms on the surface, we use as our numerical represention an equivalent vector field with values specified at each of the Lebedev quadrature nodes. To simplify our discussion of our numerical methods we use the terminiology vector field and scalar field interchangably throughout.

The 1-form $\mathbf{v}^\flat$ is equivalent through the isomorphism $\sharp$ to the vector field $\mathbf{v}^\sharp$. We represent 1-forms by the values of $\mathbf{v}^\sharp$ stored at the Lebedev quadrature nodes $\{\mathbf{x}_\ell\}$. In numerical calculations we avoid issues with charts and coordinate singularities by representing the form as an expansion of spherical harmonics using the coordinates of the embedding space. This is done by representing the components of the associated vector field $\mathbf{v}^\sharp$ using the embedding space basis $\boldsymbol{\iota}_1, \boldsymbol{\iota}_2, \boldsymbol{\iota}_3$ as $\mathbf{v}^\sharp(\mathbf{x}_\ell) = \bar{v}^x \boldsymbol{\iota}_1 + \bar{v}^y \boldsymbol{\iota}_2 + \bar{v}^z \boldsymbol{\iota}_2 = [\bar{v}^x, \bar{v}^y, \bar{v}^z]_{\boldsymbol{\iota}_1, \boldsymbol{\iota}_2, \boldsymbol{\iota}_3}$. Storing the values $[\bar{v}^x, \bar{v}^y, \bar{v}^z]$ at the Lebedev nodes provides a convenient numerical representation

of the differential form. To simplify the notation, we will often drop the subscript on $[\cdot,\cdot,\cdot]$ for the basis when it can be understood by context. When a continuum representation of the vector field is needed in our numerical calculations, we use the hyperinterpolation in equation 3.2.5 to obtain the associated smooth vector field

$$\bar{\mathbf{v}}^{\sharp}(\theta,\phi) = [\mathcal{P}\bar{v}^{x}, \mathcal{P}\bar{v}^{y}, \mathcal{P}\bar{v}^{z}]. \tag{3.2.7}$$

We take a similar approach for 0-forms and 2-forms which are much easier to handle and are represented by the scalar field $\bar{v}$ to yield $\bar{\mathbf{v}}^{\sharp}(\theta,\phi) = \mathcal{P}\bar{v}$.

3.3 Computing Exterior Calculus Operators

3.3.1 Computing the Exterior Derivative

To approximate the exterior derivative $\mathbf{d}$, we need to approximate derivatives of our numerical representation at the Lebdev nodes for differential forms. For this purpose, we make use of the hyperinterpolation provided by equation 3.2.7. We remark that our approach in our numerical representation making use of the embedding space basis provides a global description of the differential form over the entire surface and a consistent way to obtain derivatives between different coordinate charts. For a given chart, a differential form has coordinate components for a 0-form given by $\mathbf{v}^{\flat} = v$, a 1-form by $\mathbf{v}^{\flat} = v_i d\mathbf{x}^i$, and a 2-form by $\mathbf{v}^{\flat} = v_{ij} d\mathbf{x}^i \wedge d\mathbf{x}^j$. To numerically compute derivatives based on these expressions

we perform a conversion from the vector field representation in the embedding space to the local coordinate representation of the components.

The 1-form presents the most interesting case with the 0-form and 2-form handled similarly. For 1-forms the components v_i are related to the components $\bar{v}^k$ of the vector field representation by $v_i = g_{ij}v^j = g_{ij}a^j_k\bar{v}^k$. The term a^j_k converts between the components $\bar{v}^k$ given in the coordinates of the embedding space $\boldsymbol{\iota}_1, \boldsymbol{\iota}_2, \boldsymbol{\iota}_3$ to the components v^j given in the local coordinates on the surface $\partial_\theta, \partial_\phi$. The exterior derivative of a 1-form can be expressed in coordinate components as $\mathbf{dv}^\flat = \partial_s v_i \, d\mathbf{x}^s \wedge d\mathbf{x}^i$. For numerical calculations at a given location $\mathbf{x}_\ell$ (Lebedev node), we choose an appropriate coordinate chart that is locally non-degenerate. We compute the component derivative as

$$\partial_s v_i = (\partial_s g_{ij})a^j_k\bar{v}^k + g_{ij}(\partial_s a^j_k)\bar{v}^k + g_{ij}a^j_k(\partial_s\bar{v}^k). \tag{3.3.1}$$

The first two terms only depend on the geometry of the manifold and only the values of the differential form at location $\mathbf{x}_\ell$ (Lebedev node). This can be obtained readily from the spherical harmonics representation of the geometry of the manifold. In contrast, the last term depends on the derivatives of the coordinate components and requires use of the continuum representation from the hyperinterpolation obtained in equation 3.2.7. Putting this together with equation 3.3.1 and the coordinate expression for the exterior derivative, we obtain a numerical exterior derivative operator $\overline{\mathbf{d}}$ for 1-forms. The case of 0-form and 2-form can be handled similarly. We should mention that the case of a 2-form in two dimensions

has exterior derivative zero which we also impose in our numerical calculations. In this manner, we obtain a numerical operator $\overline{\mathbf{d}}$ that maps a k-form defined at the Lebedev nodes to a $(k+1)$-form defined at the Lebedev nodes.

We remark that in practical implementations of the numerical exterior derivative operator $\overline{\mathbf{d}}$ it is convenient to represent the coordinate conversion in matrix-vector notation as $\mathbf{v} = GA^{-1}\bar{\mathbf{v}}$. The matrix entries $[A^{-1}]_{jk} = a^j_k$ correspond to the change from the coordinates of the embedding space to the local coordinates of the tangent space. The matrix G corresponds to the linear operator associated with the metric tensor in the tangent plane of the two dimensional manifold. If we oriented the embedding space coordinates so that the first two components are orthogonal and oriented in the direction of the tangent plane of the surface, the entries would be given by $[G]_{i,j} = g_{ij}$ for $i, j \in 1, 2$ and zero otherwise. Of course in general embedding space coordinates the matrix G representing this linear operation takes on an equivalent form under the change of basis formula of linear algebra. With this notation, the derivatives in local coordinates can be expressed as $\partial_s \mathbf{v} = (\partial_s G)A^{-1}\bar{\mathbf{v}} + G(\partial_s A^{-1})\bar{\mathbf{v}} + GA^{-1}(\partial_s \bar{\mathbf{v}})$. To avoid differentiating components of the inverse matrix A^{-1}, we use the identity $\partial_s A^{-1} = -A^{-1}(\partial_s A)A^{-1}$ and use a linear algebra solver to compute the action of A^{-1}. This is done at each Lebedev node $\mathbf{x}_\ell$ with an appropriate choice made for the coordinate chart that is locally non-degenerate.

3.3.2 Computing the Hodge Star

We approximate next the Hodge star $\star$ operator on differential forms. We remark that in the related area of discrete exterior calculus (DEC) efforts are made to preserve geometric structure in the discrete setting, often on triangulated meshes. Interesting issues arise in DEC from the discrete geometry with which one must grapple and extensive studies have been conducted to formulate good approximations for the Hodge star $\star$ operator [139, 140]. Here we avoid many of these issues since we treat the operator at the continuum level and have more geometric information available to us from our spectral representation of both the manifold and the differential forms.

We approximate the Hodge star $\star$ operator on differential forms by a numerical operator $\overline{\star}$ which makes use of the representation at the Lebedev nodes. The Hodge star $\star$ has the feature that it is a local operation that involves values of the differential form and metric tensor only at an individual Lebedev node $\mathbf{x}_\ell$. We obtain a numerical operator $\overline{\star}$ by applying the musical isomorphisms and metric tensor within the appropiate coordinate charts. The main consideration numerically is to choose well the coordinate chart so it is locally non-degenerate. The approximation enters through the fidelity of the metric tensor computed from our representation of the manifold geometry. The geometry for the radial manifold is determined by the radial function $r(\theta, \phi)$ which is represented as an expansion in a finite number of spherical harmonics up to order L, $r(\theta, \phi) =$

$\sum_i \hat{r}_i Y_i(\theta, \phi)$. This provides in a given coordinate chart at location $\mathbf{x}_\ell$ the metric tensor and curvature tensor along with the local coordinate basis vectors $\partial_\theta, \partial_\phi$ and their derivatives. The numerical Hodge star operator $\overline{\star}$ maps k-forms defined at the Lebedev nodes to $(n-k)$-forms defined at the Lebedev nodes. This provides a convenient map between representations for further application of numerical exterior calculus operations. In this manner, the numerical exterior derivative $\overline{\mathbf{d}}$ operator and numerical Hodge star $\overline{\star}$ operator can be used through composition to numerically approximate more complex exterior calculus operations on the manifold.

3.4 Convergence of our Exterior Calculus Operators

We discuss how our numerical methods converge in approximating the fundamental exterior calculus operations of the exterior derivative $\mathbf{d}$ and the Hodge star $\star$ when applied to 0-forms, 1-forms and 2-forms. We then discuss the convergence of our methods for compositions of operators and present results for the Laplace-Beltrami equation.

We remark that throughout our convergence studies, we describe test functions using for a point $\mathbf{x}$ on the manifold its location within the embedding space. To perform calculations we make use of the embedding space coordi-

nates $[x, y, z]$ corresponding to $\mathbf{x} = x\boldsymbol{\iota}_1 + y\boldsymbol{\iota}_2 + z\boldsymbol{\iota}_3$, where $\boldsymbol{\iota}_1, \boldsymbol{\iota}_2, \boldsymbol{\iota}_3$ is the basis for the embedding space. In this manner our test data is not tied to a specific choice of local coordinates on the manifold. All figures report the relative error $\epsilon_{\text{rel}} = \|\bar{\mathbf{w}}^\sharp - \mathbf{w}^\sharp\|_2 / \|\mathbf{w}^\sharp\|_2$. The $\mathbf{w}$ is the exact result and $\bar{\mathbf{w}}$ is the numerically computed result. For $\|\cdot\|_2$, we use the L^2-norm of the embedding space.

3.4.1 Convergence of the Hodge Star

We approximate the Hodge star $\star$ by the numerical operator $\bar{\star}$ using hyper-interpolation. We investigate in practice the accuracy of this approach on a few different geometries and differential forms.

We first consider a 0-form defined on Manifold B defined in Figure 1.1. We take the 0-form to be $f = \exp(z)/(3 - y)$. We show the accuracy of our numerical operator $\bar{\star}$ in approximating the Hodge star $\star$ as the number of Lebedev nodes increases. We find that the main limitation in the accuracy of the $\bar{\star}$ is the resolution of the geometry of the manifold. This is seen in our results where once a sufficient number of spherical harmonic modes are reached the relative error rapidly decays in approximating $\star f$. The convergence of $\bar{\star}$ as the number of Lebedev nodes is increased and when the geometry is varied is shown in Figure 3.3. We remark that the the function f provides a description in terms of the embedding-space coordinates for conveniently generating smooth example fields on the radial manifold surfaces which are all bounded within a ball of radius 2

away from the singularity at $y = 3$. Choosing a function f with a singularity in the embedding-space helps in generating interesting non band-limited fields on the manifold surfaces for testing purposes.

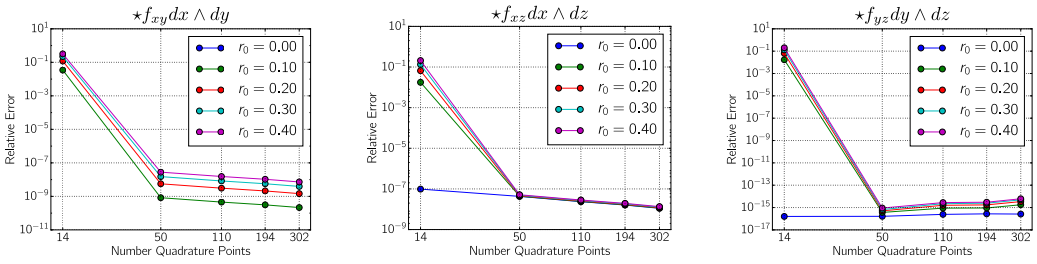

Figure 3.3: Convergence of the numerical Hodge star operator $\overline{\star}$ for 0-forms. We show for Manifold B how the relative error of $\overline{\star} f$ in approximating $\star f$ as the number of Lebedev nodes increases. The 0-form is $f = \exp(z)/(3 - y)$. We investigate how the manifold geometry influences convergence by varying the amplitude r_0 in the range $[0.0, 0.4]$ for Manifold B. The amplitude $r_0 = 0.0$ corresponds to a sphere and $r_0 = 0.4$ to the final shape of Manifold B shown in Figure 1.1. We remark that all plots are log-log where for each data point for clarity we have labelled along the log x-axis the specific number of quadrature points.

We next consider on Manifold B the 1-form $\alpha = \sqrt{|g|}\exp(z)d\theta + \sqrt{|g|}\exp(z)d\phi$. We again find that the main limitation in the accuracy of the $\overline{\star}$ is the resolution of the geometry of the manifold. In this case we find the error rapidly decreases once a sufficient number spherical harmonic modes are used. The convergence of $\overline{\star}$ as the number of Lebedev nodes is increased and when the geometry is varied is shown in Figure 3.4.

These results indicate that the numerical operator $\overline{\star}$ provides an accurate approximation to the Hodge star $\star$. Given the localized nature of the Hodge star,

the main consideration to obtain accurate results with $\overline{\star}$ is to use enough Lebedev nodes to ensure sufficient resolution of the geometry of the manifold.

3.4.2 Convergence of the Exterior Derivative

We investigate the convergence of the numerical operator $\overline{\mathbf{d}}$ in approximating the exterior derivative $\mathbf{d}$ when applied to 0-forms and 1-forms. We do not consider 2-forms here since in two dimensions the exterior derivative would be zero which we also impose in our numerical calculations [80, 111]. We consider the 0-form given by $f = \exp(z)$ and the 1-form given by $\alpha = |g| \exp(z) d\theta + |g| \exp(z) d\phi$. We consider for Manifold B the relative error of $\overline{\mathbf{d}}$ in approximating $\mathbf{d}$ as the number of Lebedev nodes is increased and the manifold geometry is varied. These results are shown in Figure 3.5 and Figure 3.6.

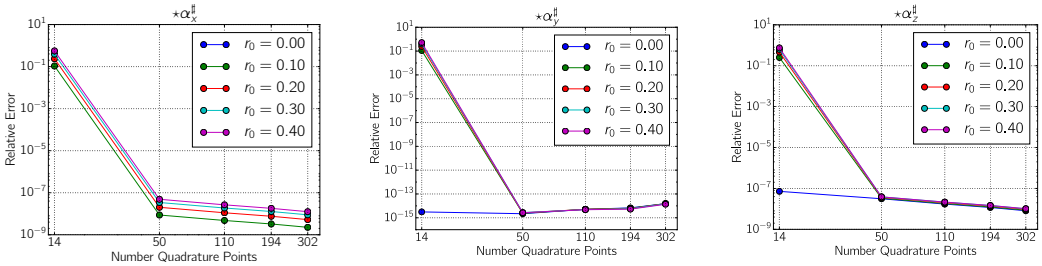

Figure 3.4: Convergence of the numerical Hodge star operator $\overline{\star}$ for 1-forms. We show for Manifold B the relative error of $\overline{\star}\alpha$ in approximating $\star\alpha$ as the number of Lebedev nodes increases. The 1-form is $\alpha = \sqrt{|g|} \exp(z) d\theta + \sqrt{|g|} \exp(z) d\phi$. We investigate how the manifold geometry influences convergence by varying the amplitude r_0 in the range $[0.0, 0.4]$ for Manifold B. The amplitude $r_0 = 0.0$ corresponds to a sphere and $r_0 = 0.4$ to the final shape of Manifold B shown in Figure 1.1.

We see that the numerical operator $\overline{\mathbf{d}}$ converges spectrally in approximating the exterior derivative $\mathbf{d}$ both for the 0-forms and 1-forms. Interestingly, we see that in the case when $r_0 = 0.0$ the approximation converges significantly more rapid than the cases when $r_0 \neq 0$. This occurs since $r_0 = 0$ corresponds to the case when the shape is a sphere where the geometry is relatively simple and many of the geometric terms to be numerically approximated greatly simplify. The main source of error in this case arises primarily from the hyperinterpolation used for computing the derivatives. In the case when $r_0 \neq 0$, the isogeometric approach used to compute $\overline{\mathbf{d}}$ approximates the geometry of the manifold using a finite spherical harmonics representation which results in an additional source of approximation error.

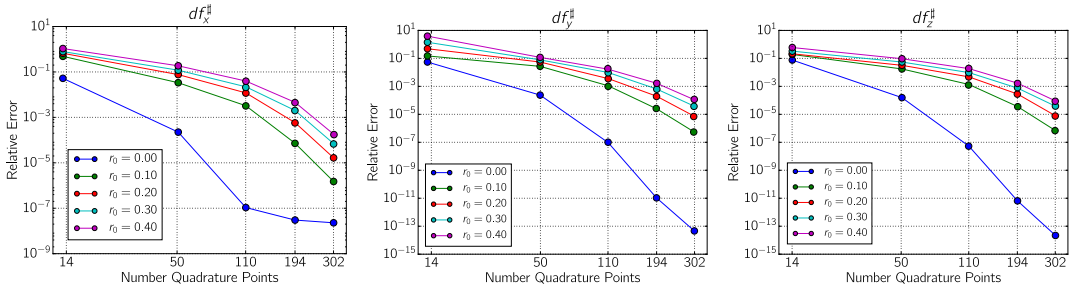

Figure 3.5: Convergence of the numerical exterior derivative operator $\overline{\mathbf{d}}$ for 0-forms. We show for Manifold B the relative error of $\overline{\mathbf{d}}f$ in approximating $\mathbf{d}f$ as the number of Lebedev nodes increases. The 0-form is $f = \exp(z)$. We investigate how the manifold geometry influences convergence by varying the amplitude r_0 in the range $[0.0, 0.4]$ for Manifold B. The amplitude $r_0 = 0.0$ corresponds to a sphere and $r_0 = 0.4$ to the final shape of Manifold B shown in Figure 1.1.

We investigate how the geometry contributes to convergence by varying r_0 over the range $[0.0, 0.4]$. The case with $r_0 = 0.4$ corresponds to the final shape of Manifold B shown in Figure 1.1. The convergence is found to be spectral and comparable in each of these different cases for the geometry. We see that as one might expect the largest errors are incurred in the case with the most pronounced geometry corresponding to $r_0 = 0.4$. Overall, the results indicate that the numerical operator $\overline{\mathbf{d}}$ provides for 0-forms and 1-forms an accurate approximation for the exterior derivative $\mathbf{d}$.

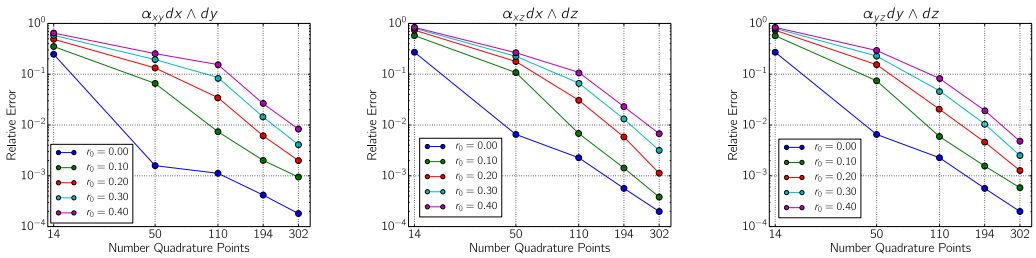

Figure 3.6: Convergence of the numerical exterior derivative operator $\overline{\mathbf{d}}$ for 1-forms. We show for Manifold B the relative error of $\overline{\mathbf{d}}\alpha$ in approximating $\mathbf{d}\alpha$ as the number of Lebedev nodes increases. The 1-form is $\alpha = |g| \exp(z) d\theta + |g| \exp(z) d\phi$. We investigate how the manifold geometry influences convergence by varying the amplitude r_0 in the range $[0.0, 0.4]$ for Manifold B. The amplitude $r_0 = 0.0$ corresponds to a sphere and $r_0 = 0.4$ to the final shape of Manifold B shown in Figure 1.1.

Chapter 4

Implementing a Spectrally Accurate Stokes Solver on Radial Manifolds

We develop spectral methods based on a Galerkin-style approximation by introducing an L^2-inner-product $\langle , \rangle_{\mathcal{M}}$ on the manifold surface $\mathcal{M}$. To approximate the inner-product with a high order of accuracy we use hyperinterpolation [124] on the manifold. For the case when the manifold is a sphere we use the Lebedev quadrature [1, 2]. We introduce here ways to develop high order quadratures for integration on more general manifold surfaces of radial shape. Our approach is based on the use of the Radon-Nikodym Theorem [103] to relate in a coordinate-free manner the measure associated with surface area on the sphere to the radial manifold.

Many approximations enter into our solver with sources of numerical errors including the finite spherical harmonics expansions used to represent fields and the surface geometry, the surface quadratures for integration and inner-products,

and the Galkerin approximation for the differential operators. We first show the efficacy of our approach for quadrature on radial manifolds, and then investigate the convergence and accuracy of our hydrodynamics solver.

4.1 Inducing an Inner-Product on Radial Manifolds

We introduce a metric associated L^2 inner-product $\langle , \rangle_{\mathcal{M}}$ on the manifold surface $\mathcal{M}$. For any two differential k-forms $\boldsymbol{\alpha}$ and $\boldsymbol{\beta}$ we introduce the manifold inner-product

$$\langle \boldsymbol{\alpha}, \boldsymbol{\beta} \rangle_{\mathcal{M}} = \int_{\mathcal{M}} \langle \boldsymbol{\alpha}, \boldsymbol{\beta} \rangle_g \, dA \tag{4.1.1}$$

where $\langle \boldsymbol{\alpha}, \boldsymbol{\beta} \rangle_g$ is the local metric inner-product on k-forms on the manifold. To compute in practice this inner-product to a high order of accuracy we need to integrate over the manifold. For this purpose we introduce an approach based on Lebedev quadratures.

We obtain a quadrature formula having a high level of accuracy for integration on the radial manifold surface using the manifold metric. We derive surface quadratures by using a diffeomorphism Φ that transforms the reference sphere to the radial manifold. This is done by first considering functions f expressible as a finite combination of spherical harmonics up to the order of accuracy of the quadrature. These band-limited functions f are integrated exactly by the

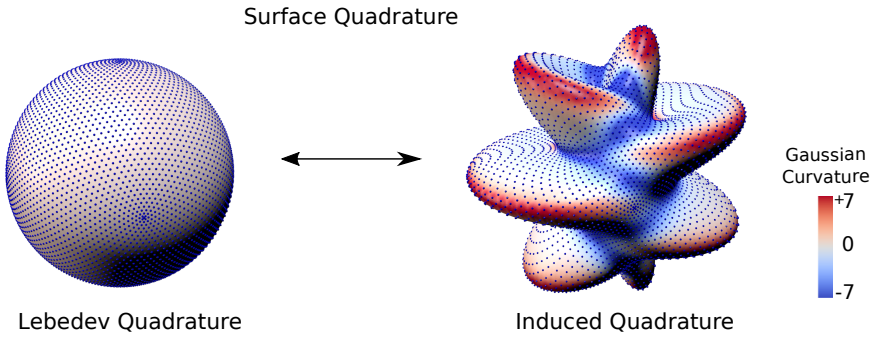

Figure 4.1: Lebedev Quadrature with 5810 nodes. We show on the left the Lebedev quadratures for integration of functions on a sphere of unit radius. The Lebedev quadrature integrates exactly all spherical harmonics up to the 131^{st} order [2]. The mapping of the sphere to the manifold on the right induces a new quadrature weighted by the local manifold metric. While the induced quadrature is no longer exact for spherical harmonics on the surface it still exhibits a high level of accuracy. We show by the colors the Gaussian curvature K on the surfaces over the range -7 to 7.

Lebedev quadrature with nodes $\mathbf{x}_i$ and weights w_i which we can express using spherical coordinates as

$$\int_{\mathcal{S}^2} f dA = \int_0^{2\pi} \int_0^{\pi} f \sin(\phi) d\phi d\theta = \sum_i f_i \cdot w_i. \tag{4.1.2}$$

The integration on the manifold surface $\mathcal{M}$ can be expressed using spherical coordinates as

$$\int_{\mathcal{M}} f dA = \int_0^{2\pi} \int_0^{\pi} f \sqrt{|g|} d\phi d\theta = \int_0^{2\pi} \int_0^{\pi} f \frac{\sqrt{|g|}}{\sin(\phi)} \sin(\phi) d\phi d\theta = \int_{\mathcal{S}^2} f \frac{\sqrt{|g|}}{\sin(\phi)} d\mathcal{S}^2 \tag{4.1.3}$$

The term $\sin(\phi)$ vanishes at the poles and must be considered carefully. Since the metric has been expressed relative to spherical coordinates, we have for radial manifolds generated by diffeomorphisms that the $\sqrt{|g|}$ vanishes at the pole and even more importantly the ratio $\sqrt{|g|}/\sin(\phi)$ approaches a finite value in the limit of approaching a pole. To derive a quadrature on the surface it is useful to give an alternative view on our derivation of equation 4.1.3 more abstractly without relying on coordinates. We can pull-back integration to be on the reference sphere and consider the change of measure for areas that must occur when transforming from the unit sphere to the radial manifold. The pull-back of the radial manifold area measure $\mu_{\mathcal{M}}$ to the sphere is always absolutely continuous with respect to the sphere area measure $\mu_{\mathcal{S}^2}$. By the Radon-Nikodym Theorem [103], this allows us to express without reference to coordinates the relationship between

the integrations as

$$\int_{\mathcal{M}} f d\mu_{\mathcal{M}} = \int_{\mathcal{S}^2} f \eta d\mu_{\mathcal{S}^2}. \tag{4.1.4}$$

The $\eta(\mathbf{x}) = d\mu_{\mathcal{M}}/\mu_{\mathcal{S}^2}$ denotes the Radon-Nikodym derivative at $\mathbf{x}$ [103]. We make the correspondence $dA = d\mu_{\mathcal{M}}$ with dA to be understood by context as the area element on the manifold $\mathcal{M}$. We also make the correspondence $dA = d\mu_{\mathcal{S}^2}$ to be understood by context as the area element on the sphere surface. From these considerations, we have for any chart of spherical coordinates $(\bar{\theta}, \bar{\phi})$ that

$$\int_{\mathcal{M}} f dA = \int_{\mathcal{S}^2} f \eta dA = \int_{\mathcal{S}^2} f \frac{\sqrt{|\bar{g}|}}{\sin(\bar{\phi})} dA. \tag{4.1.5}$$

The first two expressions are coordinate-free whereas the last expression depends on the chosen spherical coordinates $(\bar{\theta}, \bar{\phi})$. Since this correspondence holds for integration over any smooth subset of the manifold, we have that the Radon-Nikodym derivative at $\mathbf{x}$ can be expressed for any two choices of spherical coordinates (θ, ϕ) and $(\tilde{\theta}, \tilde{\phi})$ as

$$\eta(\mathbf{x}) = \frac{\sqrt{|g|}}{\sin(\phi)} = \frac{\sqrt{|\tilde{g}|}}{\sin(\tilde{\phi})}. \tag{4.1.6}$$

This shows that the ratio that arises does not depend on the particular choice of coordinates. This is useful in numerical calculations since we can use coordinate charts so that any location $\mathbf{x}$ on the sphere the ratio has a non-vanishing denominator. We use primarily two coordinate charts throughout our calculations. The first with the poles along the z-axis (north and south poles) and the

second with the poles along the x-axis (east and west poles) [6]. We denote these by (θ, ϕ) and $(\tilde{\theta}, \tilde{\phi})$. For instance, when the denominator would be too close to zero for reliable numerical calculation in the first chart, we switch to the second chart and compute $\sqrt{|\tilde{g}|}/\sin(\phi)$ where $\tilde{g}$ is the metric expressed in the other chart coordinates.

These results give us a way to use a quadrature on the sphere to induce a quadrature on the manifold surface as

$$\int_{\mathcal{M}} f dA = \sum_i f_i \cdot \bar{w}_i. \tag{4.1.7}$$

The induced weights are given by $\bar{w}_i = \eta(\mathbf{x}_i) w_i = \sqrt{|g|}/\sin(\phi) w_i$ and nodes $\mathbf{z}_i = \Phi(\mathbf{x}_i)$. In the case of Lebedev quadratures and radial manifolds the quadrature is no longer exact for spherical harmonics. Instead the quadrature is exact for the collection of functions of the form $f = Y/\eta$ where Y is a finite combination of spherical harmonics. In practice, we find that the induced quadrature still exhibits a high level of accuracy for smooth fields on the radial manifolds we consider. We use these results to compute the manifold L^2-inner-product for the surface by $\langle \boldsymbol{\alpha}, \boldsymbol{\beta} \rangle_{\mathcal{M}} \approx \langle \boldsymbol{\alpha}, \boldsymbol{\beta} \rangle_Q$ with

$$\langle \boldsymbol{\alpha}, \boldsymbol{\beta} \rangle_Q = \sum_i \langle \boldsymbol{\alpha}(\mathbf{x}_i), \boldsymbol{\beta}(\mathbf{x}_i) \rangle_g \cdot \bar{w}_i. \tag{4.1.8}$$

4.2 Validating Our Quadratures on Radial Manifolds

Since in general it is not straight-forward to obtained closed-form analytic solutions for surface integrals on general radial manifolds, we develop a test based on the Gauss-Bonnet Theorem [4, 3]. Since each of the manifolds have spherical topology, a consequence of the Gauss-Bonnet Theorem is that the Gaussian curvature when integrated over the surface must have

$$\int_{\mathcal{M}} K(\mathbf{x}) dA = 2\pi\chi(\mathcal{M}). \tag{4.2.1}$$

The $\chi(\mathcal{M})$ is the Euler Characteristic of the surface [4, 3]. For spherical topology the Euler Characteristic is $\chi(\mathcal{M}) = 2$ requiring for all the radial manifolds that $\int_{\mathcal{M}} K(\mathbf{x}) dA = 4\pi$. We perform this calculation using our surface quadrature introduced in equation 4.1.7.

This provides a significant test of a number of components of our calculation. To obtain the correct final result requires that the Gaussian curvature, metric factor, and first and second fundamental forms computed in our calculations properly combine with the Lebedev quadrature to yield the final integral value of 4π. We show the results of this test for both the oblate and prolate ellipsoidal manifolds as we vary both r_0 and the order of the quadrature in Figure 4.2.

We consider oblate and prolate ellipsoids that can be characterized by a parameter r_0 which controls the shape. In coordinates (x, y, z), the prolate ellipsoid

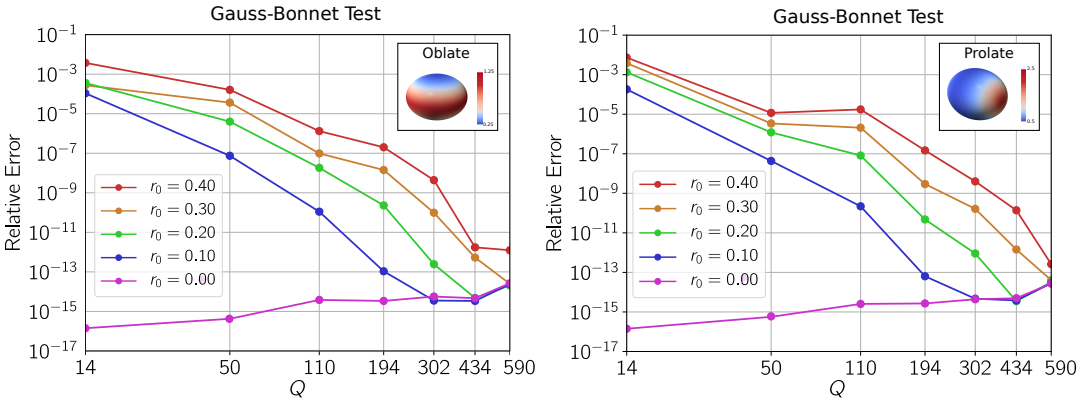

Figure 4.2: Quadrature on Radial Manifolds. For ellipsoids of oblate and prolate shapes we test the quadrature by integrating the Gaussian curvature over the manifold and compare the results with the predictions of the Gauss-Bonnet Theorem [3, 4]. We show the accuracy of the quadrature as the number of quadrature nodes Q increases and when varying the shape parameter r_0 of the ellipsoid, see equation 4.2.2 and equation 4.2.4. The case $r_0 = 0$ gives a sphere with the other r_0 values giving the shapes as shown in Figure 4.4. We show as insets the ellipsoids with $r_0 = 0.4$ and the Gaussian curvature distribution on the surface.

is 'stretched' along the z-axis while the oblate is stretched equally along both the x and y directions. The oblate ellipsoid corresponds to $(x^2+y^2)/(1+r_0)^2+z^2=1$ with

$$r(\theta,\phi) = \frac{1+r_0}{\sqrt{(1+r_0)^2\sin^2(\phi)+\cos^2(\phi)}} \tag{4.2.2}$$

$$K(\theta,\phi) = \frac{1}{\left(1+((1+r_0)^2-1)\cdot\frac{(1+r_0)^2\cos^2(\phi)}{(1+r_0)^2\cos^2(\phi)+\sin^2(\phi)}\right)^2}. \tag{4.2.3}$$

The prolate ellipsoid corresponds to $x^2+y^z+z^2/(1+r_0)^2=1$ with

$$r(\theta,\phi) = \frac{1+r_0}{\sqrt{1+(((1+r_0)^2-1)\sin^2(\phi)}} \tag{4.2.4}$$

$$K(\theta,\phi) = \frac{(1+r_0)^6}{\left((1+r_0)^4+(1-(1+r_0)^2)\cdot\frac{(1+r_0)^2\cos^2(\phi)}{(1+r_0)^2\sin^2(\phi)+\cos^2(\phi)}\right)^2}. \tag{4.2.5}$$

The K denotes the Gaussian curvature and the r is the shape function of the radial manifold. We vary r_0 to obtain different ellipsoidal shapes as shown in Figure 4.4.

For the oblate and prolate ellipsoids, we see that in each case as the number of quadrature nodes increases the computed approximation to the integral converges rapidly to the Euler characteristic of the surface $2\pi\chi(\mathcal{M})=4\pi$. We further see that even on the non-spherical manifolds the rate of convergence is super-algebraic as the number of quadrature points increase. This indicates that despite the distortions and re-weighting induced by the transformation of Lebedev nodes the radial manifold quadrature still retains a high level of accuracy, see Figure 4.2.

We perform further investigation of the quadrature methods on two radial manifolds having the more complicated shapes of Manifold B and Manifold C

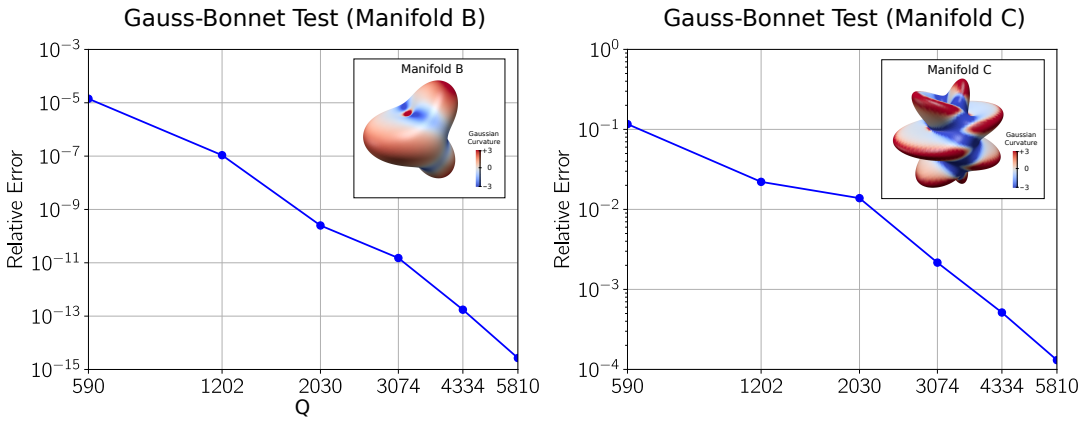

Figure 4.3: Quadrature on Radial Manifolds. We test our quadratures by integrating the Gaussian curvature on the manifold and comparing with the predictions of the Gauss-Bonnet Theorem [3, 4]. We show the relative errors as the number of quadrature points Q increases in the case of $r_0 = 0.3$ for the manifolds B and C given by equation 5.1.1. Since the Gaussian curvature is not known analytically in advance for these manifolds the test also validates the geometric approximations made in our numerical methods.

shown in Figure 4.3 and Figure 5.1. For these shapes, the Gaussian curvature on the surface is not known analytically in advance. These tests provide a stronger test and validation than just the quadratures since contributions from errors arise also from the geometric approximations made by our numerical methods discussed in Section 3.1. Our results for these tests are shown in Figure 4.3.

We find that while the combined sources of approximation yield larger errors we can still obtain overall small errors with a sufficient number of quadrature nodes. The Manifold C shape has a few regions of especially large Gaussian curvatures which provides a useful challenge for the numerical methods. We find that once the spherical harmonic basis captures sufficiently these features of the geometry the quadrature then converges rapidly. In summary, we find that given a sufficient number of quadrature nodes we can use our extended Lebedev quadratures of equation 4.1.7 to obtain accurate integration on radial manifolds.

4.3 Creating a Stiffness Matrix for the Weak Stokes Equation

We develop spectral numerical methods based on Galerkin approximation [141]. Our approach uses hyperinterpolation of functions for L^2-projection to spherical harmonics based on Lebedev quadrature [2, 125]. We consider for radial mani-

folds the partial differential equations of the form

$$\mathcal{L}\mathbf{u} = \mathfrak{g}. \tag{4.3.1}$$

We consider $\mathcal{L}$ that are linear operators that take k-forms to m-forms. We take $\mathfrak{g}$ to be a general m-form not to be confused with the metric tensor $\mathbf{g}$ discussed in Section 3.1. Typical differential operators $\mathcal{L}$ encountered in practice include operators that arise from composition of the exterior derivative $\mathbf{d}$ and Hodge star $\star$. This includes the Laplace-Beltrami operator $\Delta_{LB} = -\boldsymbol{\delta}_1\mathbf{d}_0$ which takes 0-forms to 0-forms and the Hodge Laplacian $\Delta_H = \boldsymbol{\delta}_2\mathbf{d}_1 + \mathbf{d}_0\boldsymbol{\delta}_1$ which takes 1-forms to 1-forms. The subscripts here indicate the order of differential form upon which the operators act.

To obtain numeric methods for equation 4.3.1, we consider Galerkin approximations based on the weak formulation

$$\langle \mathcal{L}\mathbf{u}, \boldsymbol{\psi} \rangle = \langle \mathfrak{g}, \boldsymbol{\psi} \rangle . \tag{4.3.2}$$

Here the $\boldsymbol{\psi}$ are test differential m-forms. We take the inner-product $\langle \cdot \rangle = \langle \cdot \rangle_{\mathcal{M}}$ to be the manifold metric associated inner-product on m-forms defined in equation 2.1.3. We denote the corresponding Hilbert space of square integrable differential m-forms as $\Lambda^2_m(\mathcal{M})$ [103, 79]. Central to our approximation is a choice of the finite dimensional subspace of $\Lambda^2_m(\mathcal{M})$. We use for our solution space the finite subspace of differential forms ψ that are dual to finite spherical harmonic expansions. In particular, we consider test m-forms that correspond to

the surface viewed as a submanifold of the ambient space. This allows in numerical calculations a way to more readily obtain global test m-forms $\boldsymbol{\psi}$. We take for given coordinates of the ambient space the test m-forms to be those forms that can be expressed using a finite spherical harmonics expansion of the form $\boldsymbol{\psi} = \psi_{i_1 \ldots i_k} \mathbf{d}x^{i_1} \wedge \ldots \wedge \mathbf{d}x^{i_k}$ with each component having finite expansion $\psi_{i_1 \ldots i_k} = \sum \hat{\psi}_{i_k}^{(\ell)} Y_\ell$ where $i_k \in \{1, 2, 3\}$ and Y_ℓ is a spherical harmonic mode. We expand using spherical harmonics up to order $\lfloor L/2 \rfloor$ since we take our quadratures up to order L. We remark that this general approach reduces to a finite spherical harmonics expansions of functions in the case of 0-forms.

We compute numerical approximations of the inner-products on the manifold surface, using our surface-induced quadratures to obtain

$$\langle \mathcal{L}\bar{u}, \boldsymbol{\psi} \rangle_Q = \langle \bar{\mathfrak{g}}, \boldsymbol{\psi} \rangle_Q \,. \tag{4.3.3}$$

When the manifold is a sphere the quadrature exactly computes the manifold inner-product when taken up to order L. In the case of the more general radial manifolds the quadrature introduces some additional source of errors in the calculation. Also in practice the operators $\mathcal{L}$ considered often have significant dependence on geometric features of the manifold. We use throughout an isogeometric approach with the manifold shape represented as a finite spherical harmonics expansion of order L. For radial manifolds this corresponds to an expansion of the function $r(\theta, \phi)$ and then computing related geometric quantities using the formulas from Section 3.2.1 to compute derivatives of the spherical harmonics.

Given these approximations we obtain the final linear system of equations for $\hat{\mathbf{u}}$

$$L\hat{\mathbf{u}} \quad = \quad M\hat{\mathfrak{g}}. \tag{4.3.4}$$

The $\hat{\mathbf{u}}$ and $\hat{\mathfrak{g}}$ denote the collection of coefficients in the expansions of $\bar{u}$ and $\bar{\mathfrak{g}}$. The L denotes the stiffness matrix and M denotes the mass matrix [141].

We mention that this weak-form associated with the manifold metric offers some particular conveniences when $\mathcal{L}$ is a differential operator that can be written as a composition of exterior calculus operators. This allows for natural use to be made of the adjoint operators to lower the differential order of the equations as is typically done in the Euclidean setting by use of integration by parts. For instance, for the Laplace-Beltrami operator we have $\langle \boldsymbol{\delta}\mathbf{d}u, \psi\rangle = \langle \mathbf{d}u, \mathbf{d}\psi\rangle$ by using the adjoint property of $\mathbf{d}$ and $\boldsymbol{\delta}$ given in equation 2.1.9. A similar approach can be carried out for other operators.

We develop numerical methods using Galerkin approximation for the hydrodynamic equations we formulated in Section 2.5 for curved fluid interfaces. We consider how to approximate equation 2.6.4 using the corresponding weak formulation. We then discuss some details of how we handle the different terms. We first give general expressions for the terms in equation 4.3.4 and then discuss how these expressions are approximated numerically.

We showed that for incompressible fluids on a surface governed by equation 2.5.3 the Hodge decomposition of equation 2.6.1 could be used to obtain equation 2.6.4. This allows us to express the fluid velocity in terms of a vector

potential Φ. For a force density $\mathbf{b}$ driving the fluid and using the generalized curl, we have $\Xi = \star\mathbf{d}\mathbf{b}^\flat = -\mathrm{curl}_{\mathcal{M}}(\mathbf{b}^\flat)$ which gives the RHS term of equation 2.6.4. We represent these fields on the radial manifold numerically using truncations of the spherical harmonics expansions

$$\Phi = \sum_{\ell} \hat{\Phi} Y_\ell, \quad \Xi = \sum_{\ell} \hat{\Xi} Y_\ell. \tag{4.3.5}$$

We use the orthogonality and normalization of the spherical harmonics discussed in Section 3.2.1. We compute the differential operators using the expressions in Section 2.3 and 3.1. In the case we are given the force density $\mathbf{b}^\flat$ we can construct the term $M\hat{\mathfrak{g}}$ in equation 4.3.4 by computing

$$[M\hat{\mathfrak{g}}]_i = \langle \Xi, Y_i \rangle_{\mathcal{M}} = -\langle - \star \mathbf{d}\mathbf{b}^\flat, Y_i \rangle_{\mathcal{M}}. \tag{4.3.6}$$

In the case when we instead are given Ξ or the expansion coefficients of $\hat{\Xi}$, we alternatively compute the product $M\hat{\mathfrak{g}}$ from

$$[\hat{\mathfrak{g}}]_i = \hat{\Xi} \tag{4.3.7}$$

$$[M]_{ij} = \langle Y_j, Y_i \rangle_{\mathcal{M}}. \tag{4.3.8}$$

The stiffness tensor L for the Stokes equations can be expressed in terms of our surface Laplacian $\bar{\Delta}$ in equation 2.6.4 as

$$L_{ij} = \left\langle \left(\mu_m \bar{\Delta}^2 - \gamma \bar{\Delta} + 2\mu_m \left(- \star \mathbf{d}(K(- \star \mathbf{d})) \right) \right) Y_i, Y_j \right\rangle_M = \tilde{A}_{ij} + \tilde{B}_{ij} + \tilde{C}_{ij} \tag{4.3.9}$$

In this notation, we have $\bar{\Delta} = -\boldsymbol{\delta}\mathbf{d}$, $\tilde{A}_{ij} = \mu_m \left\langle \bar{\Delta}^2 Y_i, Y_j \right\rangle_{\mathcal{M}}$, $\tilde{B}_{ij} = -\gamma \left\langle \bar{\Delta} Y_i, Y_j \right\rangle_{\mathcal{M}}$, $\tilde{C}_{ij} = 2\mu_m \left\langle (\star\mathbf{d}(K(\star\mathbf{d}))) Y_i, Y_j \right\rangle$. In our numerical calculations, we prefer to avoid

carrying around the sign and use the equivalent formulation in terms of the Hodge-Laplacian $\Delta_H = \boldsymbol{\delta}\mathbf{d} = -\bar{\Delta}$ as

$$L_{ij} = \left\langle \left(\mu_m \Delta_H^2 + \gamma \Delta_H + 2\mu_m \left(- \star \mathbf{d}(K(- \star \mathbf{d}))\right)\right) Y_i, Y_j \right\rangle_{\mathcal{M}} = A_{ij} + B_{ij} + C_{ij} \quad (4.3.10)$$

In this notation, we have $A_{ij} = \mu_m \left\langle \Delta_H^2 Y_i, Y_j \right\rangle_{\mathcal{M}}$, $B_{ij} = \gamma \left\langle \Delta_H Y_i, Y_j \right\rangle_{\mathcal{M}}$, $C_{ij} = 2\mu_m \left\langle (\star \mathbf{d}(K(\star \mathbf{d}))) Y_i, Y_j \right\rangle$.

As shown in Equation 2.1.9, the exterior calculus has the convenient property of allowing us to identify readily adjoint operators and perform calculations in a manner similar to integration by parts done in the Euclidean setting. We make use of the adjoint relationship between the exterior derivative operator $\mathbf{d}$ and co-differential operator $\boldsymbol{\delta}$ which gives $\langle \boldsymbol{\delta} u, v \rangle = \langle u, \mathbf{d} v \rangle$. Using these adjoint properties allows us to express the stiffness tensor as

$$\begin{aligned} L_{ij} &= A_{ij} + B_{ij} + C_{ij} && (4.3.11) \\ A_{ij} &= \mu_m \left\langle \Delta_H Y_j, \Delta_H Y_i \right\rangle_{\mathcal{M}} && (4.3.12) \\ B_{ij} &= \gamma \left\langle \mathbf{d} Y_j, \mathbf{d} Y_i \right\rangle_{\mathcal{M}} && (4.3.13) \\ C_{ij} &= -2\mu_m \left\langle K(- \star \mathbf{d}) Y_i, (- \star \mathbf{d}) Y_j \right\rangle_{\mathcal{M}}. && (4.3.14) \end{aligned}$$

This formulation for the stiffness matrix L is similar to expressions obtained in the Euclidean setting by use of integration by parts [141]. An advantage of this weak form for the stiffness matrix is that the order of differentiation has now been reduced to order two. This weak form allows us in equation 4.3.12 to replace eval-

uation of the bi-harmonic operator Δ_H^2 in equation 2.6.4 with the computation of the Hodge-Laplacian operator Δ_H two times without composition. The exterior calculus adjoint relationships are particularly useful for C_{ij} where we see that we can avoid the need to take a derivative of the Gaussian curvature K on the surface, see equation 4.3.14.

We use these expressions for the stiffness matrix to obtain $\tilde{L}$ by approximating each of the manifold inner-products $\langle \cdot, \cdot \rangle_M$ by $\langle \cdot, \cdot \rangle_Q$ using our induced Lebedev quadratures. Computing the stiffness tensor components $\tilde{L}_{ij}$ then is reduced to computing accurate local approximations of the Hodge-Laplacian operator $\Delta_H = \boldsymbol{\delta}\mathbf{d}$, exterior derivative operator $\mathbf{d}$, and the generalized curl operator $\text{curl}_{\mathcal{M}} = -\star\mathbf{d}$. This is done by using our spherical harmonics representation of the surface and applying in real-space the evaluation of these operators at the quadrature points to evaluate the needed inner-products. In this manner we obtain the terms of equations 4.3.11– 4.3.14 needed to formulate equation 4.3.4. This allows us to approximate numerically solutions of equation 2.6.4 which govern hydrodynamic flows on the surface.

4.4 Validating Spectral Convergence of our Stokes Solver on Radial Manifolds

For manifolds there are few analytically known solutions against which we can compare the results of our solver. To address this issue, we construct reference solutions on the manifold using the method of manufactured solutions [142, 143]. In the manifold setting we have additional challenges since even computing the action of the differential operators involves non-trivial dependencies on the geometry of the surface. We show how to handle these issues in the case of ellipsoids having prolate and oblate shapes to obtain reference solutions with high precision against which we can compare the results of our hydrodynamics solver.

We use the method of manufactured solutions in the hydrodynamics setting by specifying a velocity potential $\bar{\Phi}$. We make a choice for the right-hand side (RHS) force density term $\star\mathbf{d}\mathbf{b}^\flat$ so that in equation 2.6.4 we would obtain as the solution our specified $\bar{\Phi}$. To obtain the RHS data with high precision on ellipsoids we evaluate the differential operators on the left-hand-side (LHS) of equation 2.6.4 using symbolic computations [144]. We then use the RHS data for our numerical methods to solve the hydrodynamic equations 2.6.4 and compare our numerical results $\tilde{\Phi}$ and $\tilde{\mathbf{v}}$ with the known solutions $\bar{\Phi}$ and $\bar{\mathbf{v}}^\sharp = \left(-\star\,\mathbf{d}\bar{\Phi}\right)^\sharp$.

Ellipsoids provide good test manifolds for our methods since they have a level of geometric richness, such as heterogeneous Gaussian curvature, while remaining

tractable for symbolic computations. Also for ellipsoids, we have explicit expressions for many of the intermediate terms, such as the Gaussian curvature, which vary over the surface. The final expressions for the action of the operators can still result in rather large symbolic expressions but ultimately these can be evaluated accurately. We use the symbolic computational package [144] to evaluate the LHS of equation 2.6.4 throughout our calculations. We obtain with high precision the data needed for the method of manufactured solutions by evaluating $\mathcal{L}\bar{\Phi}$ to obtain

$$\text{RHS Data} = \star\mathbf{d}\mathbf{b}^\flat = \mathcal{L}\bar{\Phi}. \tag{4.4.1}$$

The $\mathcal{L}$ denotes the differential operator that appears on the LHS of equation 2.6.4. We mention that this would correspond to the surface force density $\mathbf{b}^\flat = (\boldsymbol{\delta}\mathbf{d})^{-1}(-\star\mathbf{d})\mathcal{L}\bar{\Phi}$ in equation 2.5.3.

We consider hydrodynamic flows with velocity fields generated by the vector potential

$$\Phi(\mathbf{x}) = \frac{\exp(z)}{(4-x)(4-y)}. \tag{4.4.2}$$

Note that we use the ambient space coordinates $\mathbf{x} = (x, y, z)$ to avoid issues with surface coordinates that for spherical topologies would require multiple coordinate charts to describe the function on the entire surface.

We solve the hydrodynamic equations 2.6.4 using our numerical solver. We investigate how the hydrodynamics solver performs as we refine the approximation by increasing the number of spherical harmonics. We also investigate how

the convergence behaves when we vary the shape of the manifold. We do this for ellipsoids having the prolate and oblate shapes given by equation 4.2.2 and equation 4.2.4 as shown in Figure 4.4.

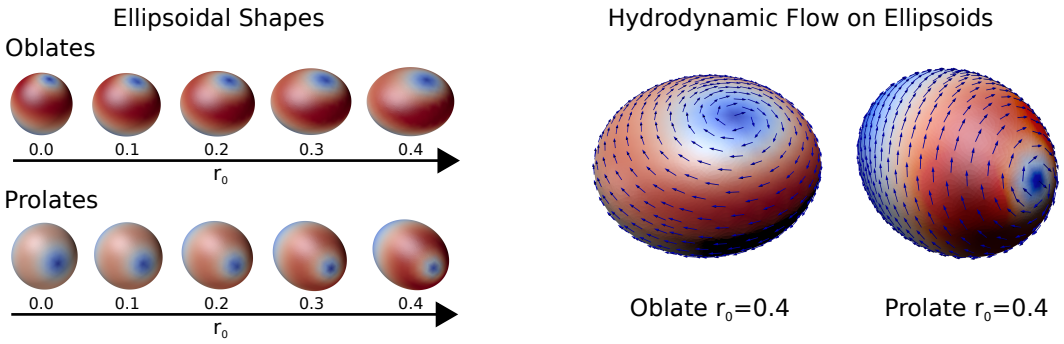

Figure 4.4: Hydrodynamic Flow on Ellipsoids. We show on the left the ellipsoid shapes in the oblate and prolate cases from equation 4.2.2 and 4.2.2 as r_0 is varied. We use these shapes for computing hydrodynamic flows driven by the surface force density in equation 4.4.1 corresponding to the vector potential of equation 4.4.2. We investigate the accuracy of the hydrodynamics solver as the number of spherical harmonics increases and the shape is varied. We show on the right the hydrodynamics flows corresponding to equation 4.4.2 in the case of the oblate and prolate when $r_0 = 0.4$.

We investigate as r_0 is varied the relative errors $\epsilon_r = \|\tilde{u} - u\|/\|u^*\|$ where u is the reference solution and $\tilde{u}$ the numerical solution. We consider both the L^2-norm and H^1-norm of the vector potential Φ, and the L^2-norm of the velocity field $\mathbf{v}$. We use on the manifold surface the L^2-norm given by $\|\boldsymbol{\alpha}\|^2 = \langle \boldsymbol{\alpha}, \boldsymbol{\alpha} \rangle_{\mathcal{M}}$ where $\boldsymbol{\alpha}$ is a k-form and the H^1-norm is given by $\|\Phi\|_{H^1} = \langle \Phi, \Phi \rangle_{\mathcal{M}} + \langle \mathbf{d}\Phi, \mathbf{d}\Phi \rangle_{\mathcal{M}}$. The convergence results for the numerical solver for hydrodynamics of ellipsoids when

increasing the resolution of spherical harmonics and when the geometry is varied are given for the oblate case in Figure 4.5 and the prolate case in Figure 4.6.

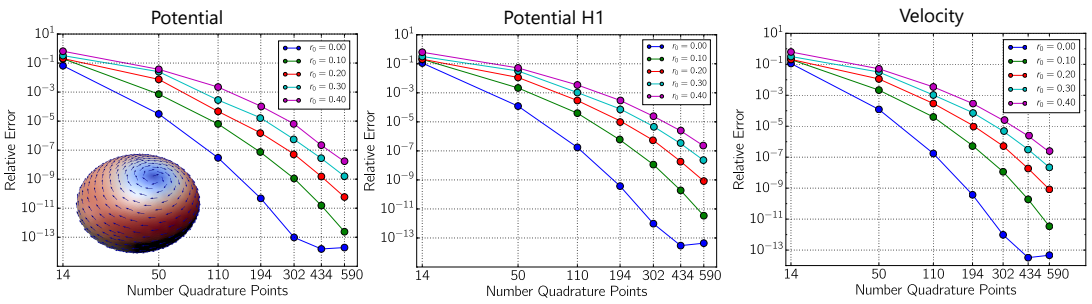

Figure 4.5: Convergence of the Stokes Flow for Oblate Ellipsoids. We show the relative errors of the L^2-norm of the potential, H^1-norm of the potential, and L^2-norm of the velocity. The results show how the error behaves as we increase the number of quadrature nodes Q and number of spherical harmonics. We use spherical harmonics up to degree $\lfloor L/2 \rfloor$ where L is the largest exact order of the corresponding Lebedev quadrature with Q nodes. We also show how convergence depends on the shape as r_0 is varied. We find in each case super-algebraic convergence of the hydrodynamic solver. For additional discussions can also see [5].

From the convergence results in Figure 4.5 and 4.6, we find in all cases that the hydrodynamics solver exhibits super-algebraic rates of convergence. We see the numerical solver can handle shapes that deviate significantly from the sphere. For these shapes the differential operators of the hydrodynamic equations involve more complicated contributions from the geometry. As the shapes become more pronounced we find somewhat slower convergence relative to the sphere case. We find that for the sphere case we can capture the solution almost up to round-off error after which the errors no longer decrease. This occurs around 434 quadra-

ture points which exactly integrates spherical harmonics up to degree 35 in the absence of round-off errors.

We mention that the convergence results of the velocity is especially indicative of our methods successfully capturing accurately geometric contributions. To obtain the solution Φ to the hydrodynamics equations 2.6.4, this requires computing accurately the geometric contributions in the differential operators. This includes sources of errors contributing from the Laplace-Beltrami operator, terms involving the Gaussian curvature, and also quadrature on the surface using equation 4.1.7. To compute the fluid velocity field $\mathbf{v}$, this also requires computing operators with geometric contributions such as the generalized curl involving

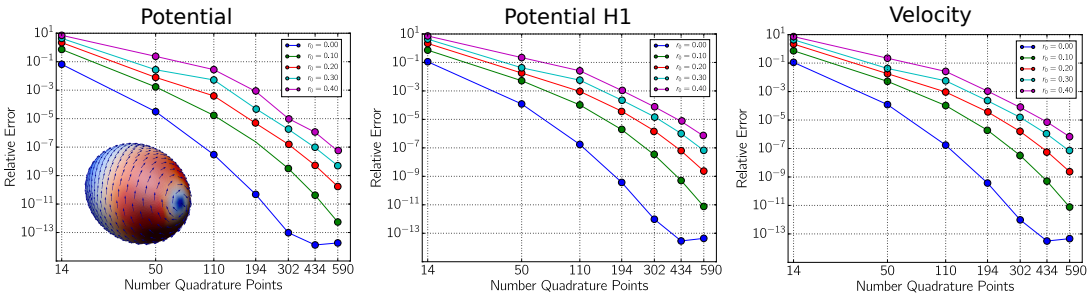

Figure 4.6: Convergence of the Stokes Flow for Prolate Ellipsoids. We show the relative errors of the L^2-norm of the potential, H^1-norm of the potential, and L^2-norm of the velocity. The results show how the error behaves as we increase the number of quadrature nodes Q and number of spherical harmonics. We use spherical harmonics up to degree $\lfloor L/2 \rfloor$ where L is the largest exact order of the corresponding Lebedev quadrature with Q nodes. We also show how convergence depends on the shape as r_0 is varied. We find in each case super-algebraic convergence of the hydrodynamic solver. For additional discussions can also see [5].

a combination of the Hodge star and exterior derivative to recover from Φ the velocity $\mathbf{v}$.

We notice in the results that the H^1 relative errors and the velocity L^2 relative errors are seen to be in close agreement. This agrees with what one would intuitively expect given the close relationship between $\mathbf{d}\Phi$ and $\mathbf{v}$. This provides another test of the accuracy of our numerical Hodge star $\star$ operator since $\mathbf{v}^\flat = - \star \mathbf{d}\Phi$.

In summary, our numerical results indicate our solver provides a convergent approximation with a super-algebraic order of accuracy for surface hydrodynamics on smooth radial manifolds. Additional discussions and details can also be found in [8, 5].

Chapter 5

Stokes Responses Under Varying Geometries

As a demonstration of our methods, we show how our approach can be used to investigate the dependence of hydrodynamic flow responses on the geometry. We compute flow responses motivated by particles immersed within a fluid interface and how they would move and interact through the interfacial hydrodynamic coupling. This arises in many physical settings such as the motions of proteins within lipid bilayer membranes [14, 17, 15] and recent interface-embedded colloidal systems [18, 19, 20, 22, 21]. We capture the fluid-structure coupling building on our recently introduced extended immersed boundary methods for manifolds in [6, 145]. While we focus here primarily on hydrodynamic flow responses, we mention that our solver could also be used as the basis for drift-diffusion simulations of microstructures on radial manifolds using our fluctuating hydrodynamics approaches [146, 147, 148, 6].

5.1 Experiments of Stokes Responses on Radial Manifolds

We consider the case of three particles subject to force when immersed within curved fluid interfaces having the shapes in Figure 5.1. We generate a force density on the surface using our extended immersed boundary methods for manifolds introduced in [6]. In the reference spherical shape, the particles are configured at the locations $\mathbf{x}_1 = (-1, 0, 0)$, $\mathbf{x}_2 = (1, 0, 0)$, $\mathbf{x}_3 = (0, -1, 0)$ with each subjected to the force $\mathbf{F} = (0, 0, 1)$. For each radial manifold shape we use the push-forward of the three locations $\mathbf{x}_1, \mathbf{x}_2, \mathbf{x}_3$ and apply force using $\mathbf{F}$ projected in the tangential direction of the surface and normalized to maintain a unit force magnitude for all shapes. We spread forces over the length-scale 0.1 on the surface using our extended immersed boundary method discussed in [6]. We show the particle configuration, force density, and hydrodynamic flow response on the sphere in Figure 5.2.

We remark that throughout our numerical calculations we allow for a net total force F_T or torque τ_T acting on the manifold which physically could drive rotational and translational rigid body motions of the entire interface within the surrounding fluid. We resolve explicitly the tangential contributions of the rigid-body motions with our numerical solver, and treat implicitly the non-tangential

contributions. Of course the flow field in other reference frames can be recovered by adding the non-tangent $\mathbf{v}_0$ velocity field at each location on the surface.

We consider the radial manifold shapes shown in Figure 5.1. These shapes are generated by the radial functions $r(\theta, \phi)$. For Manifold A which is a sphere we have $r(\theta, \phi) = 1.0$. For Manifold B and C we use

$$r(\theta,\phi) = 1 + r_0 \sin(3\phi)\cos(\theta) \ \text{(Manifold B)}, \quad r(\theta,\phi) = 1 + r_0 \sin(7\phi)\cos(\theta) \ \text{(Manifold C)} \tag{5.1.1}$$

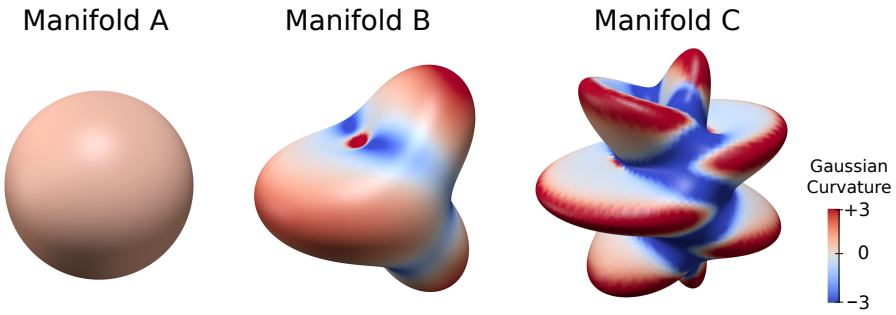

Figure 5.1: Radial Manifold Shapes. We consider hydrodynamic flows on manifolds with shapes ranging from the sphere to the more complicated geometries generated by equation 5.1.1. We show with colors the Gaussian curvature of the shapes. We take Manifold A to be a sphere of radius $R = 1.0$. We show Manifold B with $r_0 = 0.4$ and Manifold C with $r_0 = 0.4$ in equation 5.1.1.

We demonstrate how the solver captures geometric effects when varying shapes transitioning from a sphere to either Manifold B or Manifold C. Since our manifolds are always compact with spherical topology, we have from the Poincare-Hopf Theorem that our surface flows must have singularities [81, 3]. We consider hydrodynamic flow responses on shapes when changing the amplitude r_0 in the

range 0.0 to 0.4 in equation 5.1.1. We find for shapes having a relatively homogeneous curvature close to a sphere that the flows are observed to recirculate the interfacial fluid globally with just two vortices as in Figure 5.2. Interestingly, as the shapes become more complicated with heterogeneous positive and negative curvatures we see that the flow responses are observed to undergo quantitative changes and a topological transition exhibiting the creation of new vortices and saddle-point stagnation points as seen in Figure 5.3. This appears to arise from the hydrodynamic flow recirculating fluid more locally and from rigid-body rotational motions of the interface, which we discuss more below. To investigate this further, we characterize the hydrodynamics and contributions of geometry by quantifying the dissipation rates associated with flows on curved surfaces.

5.2 Variational Formulation of Stokes Equation

Stokes hydrodynamics can be viewed as solving a variational principle through the Helmholtz Minimum Dissipation Theorem [117, 149]. This corresponds to the flow minimizing the Rayleigh-Dissipation in the space of solenoidal velocity fields subject to boundary or auxiliary conditions [150]. We generalize this result and the Rayleigh-Dissipation rate to obtain a variational principle $\mathrm{Q}[\mathbf{v}^\flat]$ for the Stokes hydrodynamics equation 2.5.3 for curved fluid surfaces. This can be expressed

using the exterior calculus as

$$\inf_{\mathbf{v}} \mathrm{Q}[\mathbf{v}^\flat], \text{ where} \tag{5.2.1}$$

$$\mathrm{Q}[\mathbf{v}^\flat] = \mathrm{RD}[\mathbf{v}^\flat] - \mathrm{F}[\mathbf{v}^\flat] \tag{5.2.2}$$

$$\mathrm{RD}[\mathbf{v}^\flat] = \mu_m \langle \mathbf{d}\mathbf{v}^\flat, \mathbf{d}\mathbf{v}^\flat \rangle_{\mathcal{M}} - 2\mu_m \langle K\mathbf{v}^\flat, \mathbf{v}^\flat \rangle_{\mathcal{M}} + \gamma \langle \mathbf{v}^\flat, \mathbf{v}^\flat \rangle_{\mathcal{M}} \tag{5.2.3}$$

$$\mathrm{F}[\mathbf{v}^\flat] = \langle \mathbf{b}^\flat, \mathbf{v}^\flat \rangle_{\mathcal{M}}. \tag{5.2.4}$$

Here the minimization in $\mathbf{v}^\flat$ is constrained to be over smooth solenoidal vector fields on the surface in the sense $-\boldsymbol{\delta}\mathbf{v}^\flat = 0$ and $\mathbf{v}^\flat \in H^2(\mathcal{M})$ [103, 116]. For the given fluid constitutive laws, the Rayleigh-Dissipation term $\mathrm{RD}[\mathbf{v}^\flat]$ of equation 5.2.3 gives the rate at which the fluid is doing work when flowing according to the velocity field $\mathbf{v}^\flat$. The term F of equation 5.2.4 corresponds to the work done by the external body forces acting to drive the fluid. We derived equation 5.2.2 by taking the manifold inner product of $\mathbf{v}^\flat$ with both sides using equation 2.5.3. Central to our derivation is use of the adjoint property of the exterior derivative $\mathbf{d}$ with the co-differential $\boldsymbol{\delta}$ in the sense of equation 2.1.9. It can be shown that the solution of the Stokes equations 2.5.3 minimizes equation 5.2.2 over all velocity fields subject to the incompressibility constraint $-\boldsymbol{\delta}\mathbf{v}^\flat = 0$. Taking variational derivatives of equation 5.2.2 it readily follows that the Stokes equations 2.5.3 are recovered as the Euler-Lagrange equations of the variational problem given in equation 5.2.1 [150]. The constraints when handled by the method of Lagrange multipliers [150] gives the pressure term in equations 2.5.3.

The variational principle in equation 5.2.2 provides a useful way to view the hydrodynamic flows as arising from competing physical effects. For steady flows there is a balance between the work done by an external body force with the dissipation from the solvent drag and the dissipation from the internal shearing motions of the fluid. We see the dissipation from shearing motions can be split into two parts. The first term in equation 5.2.3 is equivalent to $\mu_m \langle \mathbf{dv}^\flat, \mathbf{dv}^\flat \rangle_{\mathcal{M}} = \mu_m \langle - \star \mathbf{dv}^\flat, - \star \mathbf{dv}^\flat \rangle_{\mathcal{M}} = \mu_m \langle \mathrm{curl}_{\mathcal{M}} \mathbf{v}^\flat, \mathrm{curl}_{\mathcal{M}} \mathbf{v}^\flat \rangle_{\mathcal{M}} = \mu_m \| \mathrm{curl}_{\mathcal{M}} \mathbf{v}^\flat \|^2_{\mathcal{M}}$. This corresponds to creation of vorticity $\omega = \mathrm{curl}_{\mathcal{M}} \mathbf{v}^\flat$ within the fluid.

The second term involves the Gaussian curvature K which depending on the sign either penalizes or promotes relative to the flat case changes in the magnitude of the fluid velocity. Since these two terms arise from the shearing motions of the fluid material in the ambient space they have a strong relationship through the surface geometry. For regions having the same vorticity distribution ω the curvature weighted term shows that regions with positive Gaussian curvature have a smaller rate of dissipation relative to regions having negative Gaussian curvature. We see that unlike the flat case the local curvature of the surface requires the fluid to flow with a momentum in the ambient space that must change locally in direction to remain within the surface. As a consequence, we see for surface constrained flows the geometry can result in additional sources of shearing motions and dissipation.

The third term corresponds to dissipation from drag of the surface fluid with the surrounding solvent fluid depending in this case only on the total manifold L^2-norm of the flow. The term $\mathrm{F}[\mathbf{v}^\flat]$ associated with equation 5.2.4 corresponds to the applied body force and penalizes the flow when it is not aligned with the force density $\mathbf{b}$. We see that expressing the Rayleigh-Dissipation with exterior calculus and splitting into these distinct terms starts to reveal some of the interesting ways hydrodynamic responses can depend on the geometry of the surface.

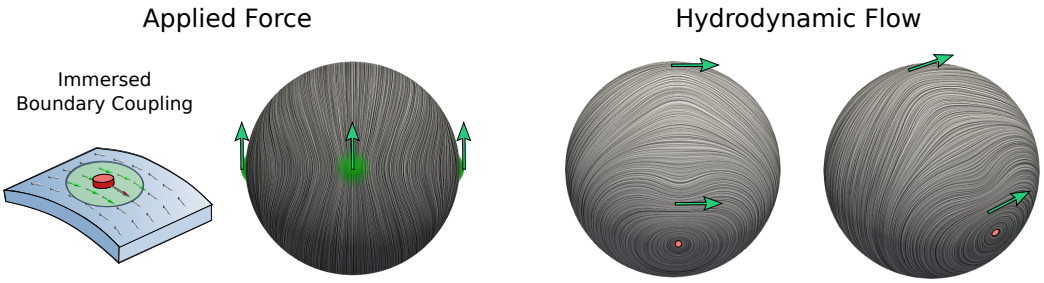

Figure 5.2: Structure of the hydrodynamic flow. We consider the case of three particles immersed within an interface of spherical shape and subjected to force. We generate a force density on the surface using the extended immersed boundary method for manifolds we introduced in [6]. The particles are configured at the locations $\mathbf{x}_1 = (-1, 0, 0)$, $\mathbf{x}_2 = (1, 0, 0)$, $\mathbf{x}_3 = (0, -1, 0)$, and each subjected to the force $\mathbf{F} = (0, 0, 1)$. We show in the left panel the immersed boundary approach for fluid-particle coupling on manifolds [6] and range of spreading around each particle used to obtain a force density on the surface. We show in the right panel the hydrodynamic flow response. The flow exhibits two two vortices and global recirculation of the fluid. We visualize the streamlines of the hydrodynamics flows using Line Integral Convolution (LIC) [7]. Hydrodynamic results are for the case with $\mu = 0.1$,$\gamma = 0.1$ and $Q = 5810$ [8].

5.3 Dissipation of Stokes Flows Under Varying Geometries

We compute the dissipation rates for hydrodynamic flow responses for the geometries ranging from the sphere to Manifold B and C when varying r_0 in the range 0.0 to 0.4 in equation 5.1.1. We show the final shapes in Figure 4.1. As a basis for comparison for investigating the role of the geometry we consider both the Stokes hydrodynamic response $\mathbf{v}$ obtained from our solver for equation 2.5.3 and the flow obtained from the push-forward of the flow $\hat{\mathbf{v}}$ from the sphere to the surface geometry $\tilde{\mathbf{v}} = \phi_* \hat{\mathbf{v}}$. The ϕ denotes the radial mapping from the sphere to the surface geometry and ϕ_* the associated push-forward [80]. We show our results for the dissipation rates for hydrodynamic flow responses $\mathbf{v}$ and push-forward flows $\tilde{\mathbf{v}}$ in Figure 5.5.

We find as we transition from the sphere to Manifold B and C with the shapes becoming more heterogeneously curved the dissipation rates for the Stokes flow is significantly smaller than the push-forward flow $\tilde{\mathbf{v}}$. The differences become especially large after the Stokes flows exhibit the topological transition with the emergence of new vortices and saddle-points as seen in Figure 5.3. We see as the geometry is varied in the range of r_0 around the topological transitions the Rayleigh-Dissipation appears to remain relatively constant in both cases in Figure 5.5. This seems to indicate that changes in the flow can accommodate to

some extent changes in the geometry to avoid the otherwise increases in dissipation that would have occurred within the fluid interface if remaining with the flow structure associated with the sphere case. We show the flow responses and relation to geometry in more detail in the plots of Figure 5.4. The geometry appears to promote for both Manifold B and C a recirculation of the fluid more locally to regions of positive Gaussian curvature possibly at the expense of creating some additional local vorticity in the fluid flow, see Figure 5.3 and Figure 5.4. We also emphasize that the quantitative and topological changes can also in part be explained by the generation from the forces acting on the fluid interface body that result in a rigid-body rotational motion. We see that in the case of the sphere we can obtain similar locally re-circulating flows when viewed in the moving reference-frame of the rotating fluid interface.

In our numerical results for Manifold B and C, we see that our geometries can exhibit elongated regions of positive Gaussian curvature surrounded by regions of negative Gaussian curvature. This is especially prominent for Manifold C as seen in Figure 4.1 and 5.4. The role of the negative Gaussian curvature term in equation 5.2.3 indicates that dissipation rates can increase relative to regions of positive curvature. This could potentially explain the preference of the fluid to recirculate more locally to avoid having to flow through regions of negative curvature. Related to our findings, there has also been some related work concerning fluid dissipation in the case of perturbations from a flat sheet, as arise in planar

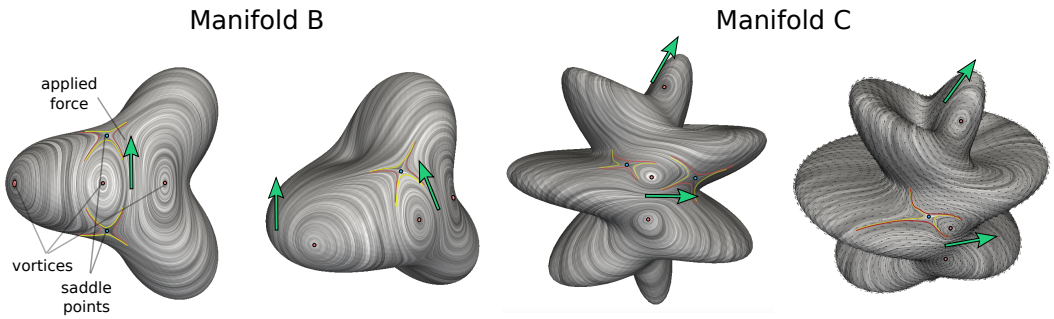

Figure 5.3: Structure of the Hydrodynamic Flow. We show for Manifold B and C the hydrodynamic flow responses for a localized unit force applied in the tangential direction to particles on the surface at the push-forward of the locations discussed in Figure 5.2. We visualize the streamlines using Line Integral Convolution (LIC) [7]. The flow responses exhibit eight critical points corresponding to six vortices and four saddle points. The vortices are marked with red points and the saddle points with cyan points. We sketch approximate separatrices for each of the saddle points. For these surfaces the hydrodynamic flows appear to exhibit structures that favor more localized recirculation of the fluid relative to the responses seen for the sphere in Figure 5.2 [8].

soap films, which were recently reported in [104]. These authors also find that curvature-induced dissipation can amplify dissipation and affect structure of the hydrodynamic flow. In our work we see even further phenomena with observed topological transitions in the structure of the hydrodynamic flow response.

5.4 The Role of Rigid-Body Rotations in Stokes Responses

We show that changes in the observed hydrodynamic responses can in part be explained by the rigid-body rotational motions induced by the non-torque balance force acting on the fluid interface seen in the ambient space reference frame. When a force is applied the fluid interface responds with a combination of localized internal flows and global rigid-body rotation.

Note, that for the purposes of this discussion we define rigid-body rotations as the projection of the canonical rigid-body rotational field into the tangent space. Since true rigid-body rotations of tangent vector fields can only occur on axially-symetric manifolds (such as the sphere or ellipsoids), our discussion generally refers to the latter definition. The key difference between these being that true rigid-body rotational flows are shear-free in our equations, while in the non-axial symetric case the shear of the flow is only minimized.

We show the hydrodynamic velocity field in the moving reference frame counter-rotated by the rigid-body rotational motions. We see in the case of the sphere we have similar vortices and saddle points when observed in the moving reference frame. In either reference frame, we find the hydrodynamic flow responses favor quantitatively more localized re-circulation of fluid.

The trade-off between these global and local responses is governed by the traction stress with the surrounding bulk fluid. In equation 2.5.3, we used a basic drag model with traction stress $\boldsymbol{\tau}_f = -\gamma \mathbf{v}$. For a fully hydrodynamic approach, which would require a solver for the bulk fluid flow, the traction stress would be $\boldsymbol{\tau}_f = \mu_f \left(\nabla \mathbf{v} + \nabla \mathbf{v}^T\right) \cdot \mathbf{n}$. We can relate these parameters for the purpose of obtaining scaling relations by $\mu_f \sim \gamma \ell_f$, where ℓ_f is a characteristic length-scale associated with variations in the flow field. We can characterize the expected relative strength of the external traction stress with the internal shear stresses of the interface by the Saffman-Delbrück (SD) length ratio L/R [6, 16]. The SD ratio characterizes the length-scale over which the interfacial flow field varies in response to a point force, where $L = \mu_m/2\mu_f \sim \mu_m/2\gamma\ell_f$ and R is the effective radius of the manifold [6]. These considerations suggest that when $L/R \ll 1$ the external traction stress $\boldsymbol{\tau}_f$ becomes large relative to the internal shear stresses and the hydrodynamic responses avoid rigid rotations and prefer instead to have flows that are more localized within the fluid interface. When $L/R \gg 1$, the external traction stress $\boldsymbol{\tau}_f$ becomes small relative to internal shear

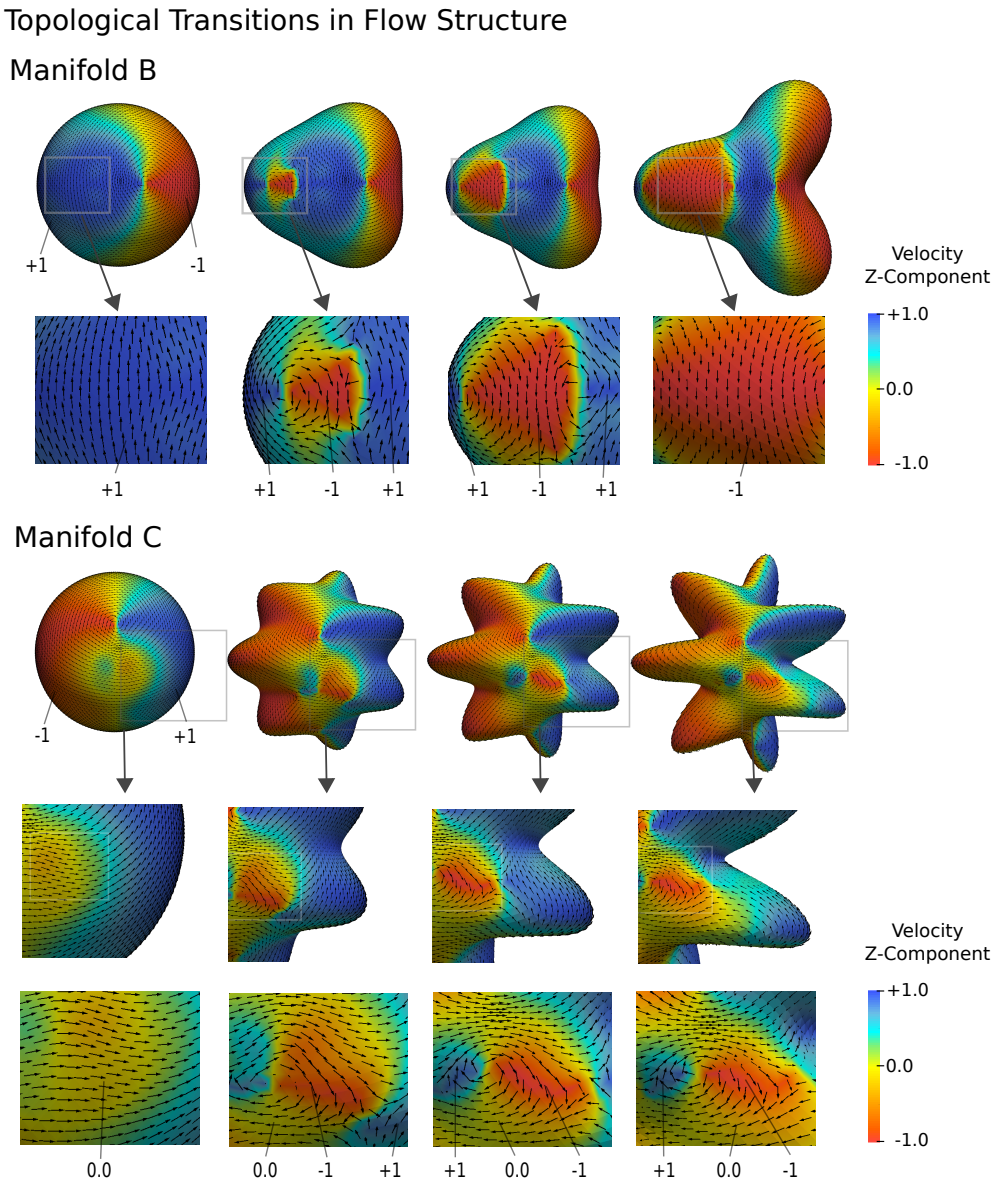

Figure 5.4: Topological Transitions in the Flow Structure. As the shapes of the manifolds deviate more from the sphere the velocity field of the hydrodynamic flow undergoes a topological transition with the creation of new vortices and saddle-points. The topological structures appear to correspond with the flow reorganizing to recirculate fluid in a more localized manner relative to the global recirculation seen on the sphere. This is especially pronounced in the elongated geometries that form for the Manifold C shapes. We show configurations for Manifold B and Manifold C when $r_0 = 0.0, 0.15, 0.25, 0.4$ in equation 5.1.1. We quantify the Rayleigh-Dissipation associated with each of these flows in Figure 5.5.

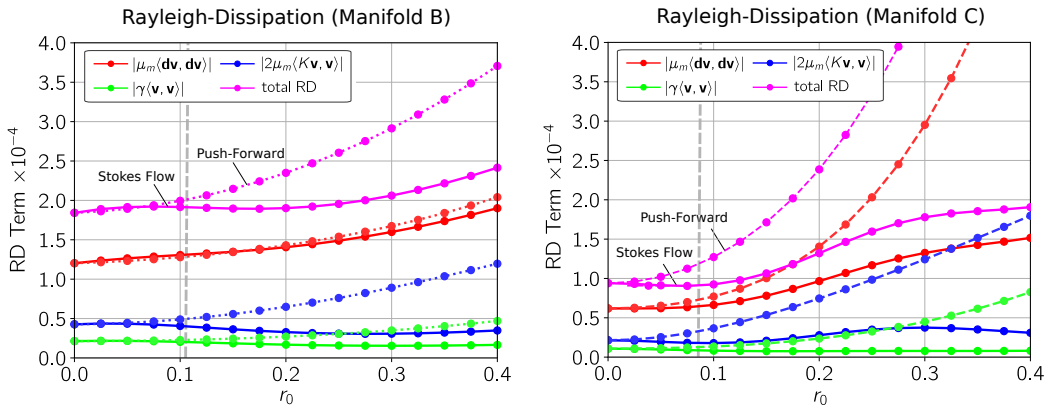

Figure 5.5: Rayleigh-Dissipation Rates of Hydrodynamic Flows. Hydrodynamic flows $\mathbf{v}$ on surfaces are obtained by solving the Stokes equations 2.5.3 as r_0 is varied. We take $\mu_m = 0.1$ and $\gamma = 0.1$ for the manifolds in Figure 5.1. RD rates for $\mathbf{v}$ are shown as solid curves. For comparison we consider the rates obtained from the velocity field $\hat{\mathbf{v}}$ of flow on the sphere (case $r_0 = 0$) obtained by the pushed-forward $\tilde{\mathbf{v}} = \phi_* \hat{\mathbf{v}}$ to the manifold shape with given r_0. RD rates for $\tilde{\mathbf{v}}$ are shown as dotted curves. We find that as the geometry deviates from the sphere the rates for the Stokes flow on the manifold become significantly smaller than the push-forward flow fields from the sphere. We find the two cases begin to diverge significantly in the regime where the velocity field transitions topologically with the addition of new vortices and saddle-point stagnation points as in Figure 5.3. This transition occurs for Manifold B around $r_0^* = 0.105$ and for Manifold C around $r_0^* = 0.085$ (vertical dashed line). These results indicate some of the ways that surface geometry can contribute to dissipation rates and hydrodynamic flow responses [8].

stresses and the hydrodynamic responses prefer now to rotate the entire interface rigidly within the bulk fluid with relatively less internal hydrodynamic flows that would result in intra-interfacial shear stresses.

We investigate hydrodynamic responses by performing a study that finds for each hydrodynamic flow the best approximating rigid-body rotational motion and then look at the counter-rotated velocity so the rotational motion can be subtracted from the hydrodynamic velocity field. This conversion of the velocity corresponds to making observations in a moving reference frame that rotates in agreement with the rigid rotational motion of the fluid interface. We show the flows in this moving reference frame for the spherical case (Manifold A) and Manifold B and Manifold C in Figure 5.6.

We find the rigid-body rotational motion when subtracted from the hydrodynamic response results within the interface in a localize flow pattern for the sphere case (Manifold A), see right-panel of Figure 5.6. We see this counter-rotation has less of a qualitative impact on the hydrodynamic responses for Manifold B and C. This in part arises since the complex shapes have larger surface area and thus larger external traction stresses that further inhibit rigid-body rotational motions relative to internal flows. These results have important implications for how the hydrodynamic flow fields are to be interpreted depending on the circumstances and reference-frame of interest in a given problem or application. When considering internal mixing or transport within the hydrodynamic interface itself, or

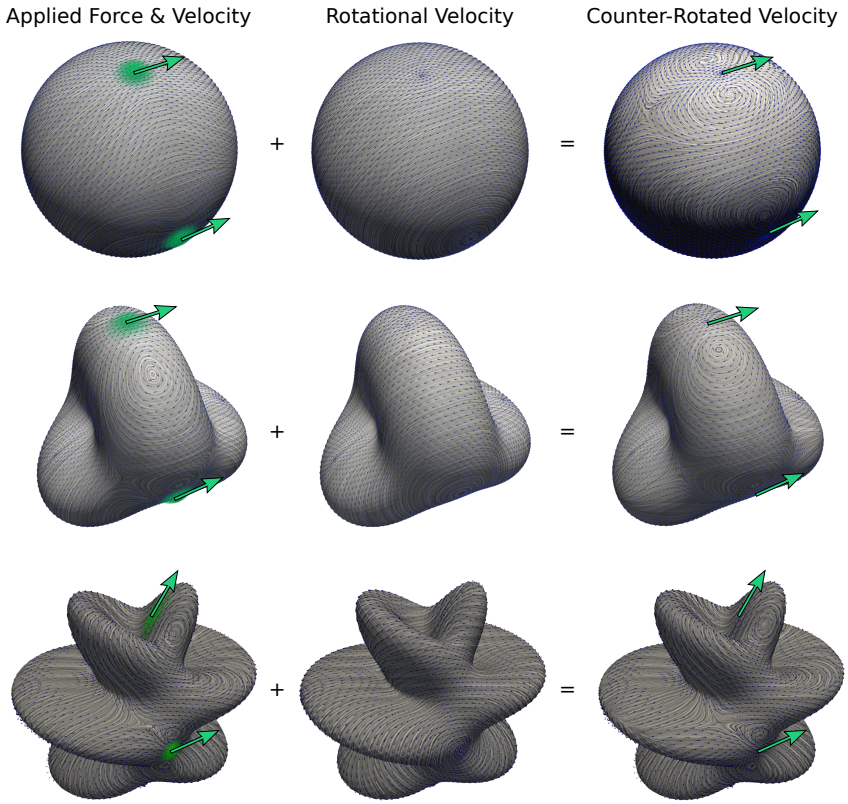

Figure 5.6: Counter-Rotated Hydrodynamic Flows. We consider the case of three particles configured at the locations $\mathbf{x}_1 = (-1, 0, 0)$, $\mathbf{x}_2 = (1, 0, 0)$, $\mathbf{x}_3 = (0, -1, 0)$ embedded within an interface and subjected to force $\mathbf{F} = (0, 0, 1)$ for the sphere and tangent for the other manifolds. We use our extended immersed boundary method for manifolds we introduced in [6]. In the left panel, we show the hydrodynamic responses for $\mu = 0.1$,$\gamma = 0.1$ and $Q = 5810$. In the middle panel, we show the rotational field that best counters the rigid-body rotation of the fluid interface. In the right panel, we have combining the velocity fields to arrive at a counter-rotated velocity field that would be observed in the moving reference frame. We visualize the streamlines of the hydrodynamics flows using Line Integral Convolution (LIC) [7].

when the interface is immobilized to prevent it from rotating, the interpretation in the reference-frame associated with the rigid-body rotational motion of the fluid interface may be the most appropriate. When considering laboratory measurements or how outside entities in the bulk fluid, such as particles or polymers, interact with the moving interface the rotational motions may play a significant role and the reference frame in the ambient space may be most appropriate. Our numerical solvers can be utilized in either of these cases to resolve the hydrodynamic flow responses. As we see from Figure 5.6, these rigid-body rotational motions can in part account for the quantitative and topological transitions in stream-lines exhibited from the perspective of the ambient space reference-frame. These results show for compact geometries the importance of considering the role of the rigid-body rotational motions in flow responses captured by our solvers and in the mechanics of the interfacial hydrodynamics. Additional discussions and details can also be found in [8, 6].

5.5 Implications of Our Experiments

These results indicate some of the rich mechanics and related phenomena captured by our solver that can arise when going beyond the often considered setting of infinite fluid sheets to instead consider hydrodynamic flows confined within compact geometries.

The numerical results we have present here to demonstrate our hydrodynamics solver indicate some of the rich ways geometry could have implications for hydrodynamic coupling and possible kinetic consequences for the motions of inclusion particles immersed in curved fluid interfaces. Further investigations also could be performed readily into the role of geometry in surface hydrodynamic phenomena using our introduced solver. We also mention that our solver can be used as the basis for developing extended immersed boundary methods for manifolds [6] and drift-diffusion simulations of particles and microstructures within curved fluid interfaces building on our fluctuating hydrodynamics approaches [146, 147, 6]. These approaches could be useful in computing interfacial mobilities and surface kinetics for many systems, such as proteins within curved lipid bilayer membranes, polymeric networks in cell biology like the spectrin network of the red-blood cell, or self-assembly for colloidal systems immersed in fluid interfaces. We also expect many of the underlying ideas used in our solver could be used to develop solvers for other PDEs on radial manifolds.

Chapter 6

Generalized Moving Least Squares for Discretizing Surface PDEs

6.1 Generalized Moving Least Squares (GMLS)

We use a Generalized Moving Least Squares (GMLS) approach for approximating partial differential equations on manifolds to approximate hydrodynamic flow responses as in our recent work [9]. GMLS is a non-parametric functional regression technique to construct approximations of functionals from scattered samples of an underlying field by solving local least-square problems [98]. Consider a function u from a Banach space $\mathbb{V}$. We assume that u is characterized by a scattered collection of sampling functionals $\Lambda(u) := \{\lambda_j(u)\}_{j=1}^N \subset \mathbb{V}^*$, where $\mathbb{V}^*$ is the dual of $\mathbb{V}$. For the purposes of this work, we will sample from point functionals, i.e. $\lambda_i(u) = \delta_{x_i} \circ u$. We thus may associate with the collection of samples the point cloud $\mathbb{X}_h := \{\mathbf{x}_j\}_{j=1}^N$. We further assume that $\mathbb{X}_h \subset \Omega \subset \mathbb{R}^d$,

for some compactly supported Ω. We characterize the distribution of points by the *fill distance*

$$h_{\mathbb{X},\Omega} = \sup_{\mathbf{x}\in\Omega} \min_{1\leq j\leq N} ||\mathbf{x} - \mathbf{x}_j||_2. \tag{6.1.1}$$

The $||\cdot||_2$ denotes the Euclidean norm. We define the *separation distance* of $\mathbb{X}_h$ by

$$q_{\mathbb{X}} = \frac{1}{2}\min_{i\neq j} ||\mathbf{x}_i - \mathbf{x}_j||_2. \tag{6.1.2}$$

We characterize the point set as being *quasi-uniform*(with respect to a constant c_{qu}) if there exists $c_{qu} > 0$ such that the following holds

$$q_{\mathbb{X}} \leq h_{\mathbb{X},\Omega} \leq c_{qu} q_{\mathbb{X}}. \tag{6.1.3}$$

For the purposes of our current work, we will assume $\mathbb{X}_h$ to be quasi-uniform; such a condition is necessary to prove existence and accuracy of the GMLS process [98, 102].

We aim to recover a given linear, bounded target functional $\tau_{\hat{\mathbf{x}}}$, where $\hat{\mathbf{x}}$ denotes a position associated with the functional. For example, when approximating the point evaluation of a differential operator with multi-index α, one may select $\tau_{\hat{\mathbf{x}}} = D^\alpha u(\hat{\mathbf{x}})$. We do this by solving the following local weighted ℓ_2-optimization problem to find the best reconstruction of the samples over some finite dimensional subspace $\mathbb{V}_h \subset \mathbb{V}$,

$$p^* = \underset{q\in\mathbf{V}_h}{\operatorname{argmin}} \sum_{j=1}^{N} \left(\lambda_j(u) - \lambda_j(q)\right)^2 \omega(\lambda_j, \tau_{\hat{\mathbf{x}}}). \tag{6.1.4}$$

Here, ω is a compactly supported positive function establishing the correlation between the information at the sample locations $\mathbf{x}_j$ and the target location $\tilde{\mathbf{x}}$. We take throughout a radially symmetric form for our weight function given by

$$\omega(\lambda_j, \tau_{\tilde{\mathbf{x}}}) = \Phi(||\mathbf{x}_j - \tilde{\mathbf{x}}||_2). \tag{6.1.5}$$

We select $\Phi(r) = (1 - r/\epsilon)^{\bar{p}+}$, where f_+ denotes the positive part of a function f and $\bar{p} > 0$ is an integer parameter used to control the decay of the weighting. The ϵ parameter controls the support of ω, and thus the compactness of the resulting approximation.

Assume a basis for $\mathbb{V}_h = \text{span}\{\phi_1, ..., \phi_{\dim(\mathbb{V}_h)}\}$, and denote as $\mathbb{P}(x)$ as the vector whose i^{th} entry is $\phi^i(x)$. Then the solution to equation 6.1.4 may be expressed in terms of a coefficient vector $\mathbf{a}(u)$,

$$p^* = P(x)^\intercal \mathbf{a}(u). \tag{6.1.6}$$

We define the GMLS approximation of $\tau_{\tilde{\mathbf{x}}}$

$$\tau^h_{\tilde{\mathbf{x}}}(u) = \tau_{\tilde{\mathbf{x}}}(\mathbb{P})^\intercal \mathbf{a}(u) \tag{6.1.7}$$

We summarize the GMLS approximation approach in Figure 6.1.

An error analysis of the GMLS process involves a number of factors. A solution to the reconstruction problem requires that Λ be unisolvent over $\mathbb{V}_h$, meaning that any element of $\mathbb{V}_h$ is uniquely determined by the collection of samples in the support of ω [98].

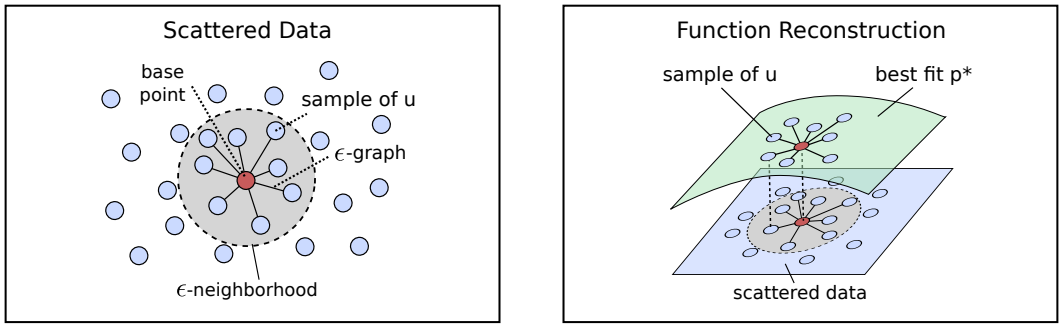

Figure 6.1: GMLS Approximation of Target Functionals. In the Generalized Moving Least Squares (GMLS) approach a collection of scattered data samples of the function values u is approximated by multiple local reconstructions. This is done by building an ϵ-graph between the points within an ϵ-neighborhood around a base point $\tilde{\mathbf{x}}$ (shown on the left). A function space $\mathbb{V}_h$ is used to reconstruct u by finding the best fitting function $p^* \in \mathbb{V}_h$ that matches the values of the sampling functionals $\{\lambda_j\}$ in the optimization problem given in equation 6.1.4 (shown on the right). For approximating a target functional τ acting on u at the base point $\tilde{\mathbf{x}}$, we obtain the approximating GMLS functional τ^h by evaluating the target functional on the reconstruction space at p^*. In this manner we can obtain approximations to general functionals acting on u [9].

The GMLS estimate of $\tau_{\tilde{\mathbf{x}}}$ in equation 6.1.7 may be expressed analytically as

$$\tau^h_{\tilde{\mathbf{x}}}(\phi) = \tau_{\tilde{\mathbf{x}}}(\mathbf{P})^\intercal \left(\Lambda(\mathbf{P})^\intercal \mathbf{W} \Lambda(\mathbf{P})\right)^{-1} \Lambda(\mathbf{P})^\intercal \mathbf{W} \Lambda(u). \tag{6.1.8}$$

We use the following notation throughout our discussions of GMLS

- $\tau_{\tilde{\mathbf{x}}}(\mathbf{P}) \in \mathbb{R}^{\dim(V_h)}$ denotes the vector with components consisting of the target functional applied to each of the basis functions ϕ_k.
- $\mathbf{W} \in \mathbb{R}^{N \times N}$ denotes the diagonal matrix with entries $\{\omega(\lambda_j, \tau_{\tilde{\mathbf{x}}})\}_{j=1}^N$.
- $\Lambda(\mathbf{P}) \in \mathbb{R}^{N \times \dim(V_h)}$ denotes the rectangular matrix whose (j,k)-entry is $\lambda_j(\phi_k)$ corresponds to the application of the j^{th} sampling functional λ_j applied to the k^{th} basis function ϕ_k.
- $\Lambda(u) \in \mathbb{R}^N$ denotes the vector consisting of entries $\{\lambda_j(u)\}_{j=1}^N$ corresponding to the N sampling functionals λ_j applied to the function u.

In practice, we remark that a particular advantage of GMLS over other least-squares approaches is that it requires only local information to build up approximations. Algorithmically, this amounts over the base points $\tilde{\mathbf{x}}$ to inversion of many separate small dense systems of normal equations given by equation 6.1.8. The GMLS approach is very well-suited to hardware acceleration and parallelization using packages such as the recent Compadre toolkit [109].

We shall consider here primarily the case when the target functional τ is selected to approximate point evaluations of either the function (i.e. regression)

or of differential operators acting on manifolds. In the case where the manifold is in $\mathbb{R}^d$, Mirzaei provides the following convergence result [102].

$$\|\mathcal{D}^{\boldsymbol{\alpha}} u - \mathcal{D}^{\boldsymbol{\alpha}} p^*\|_2 \leq C h^{m+1-|\alpha|}, \tag{6.1.9}$$

assuming reconstruction over the space of $m^{th}-$order polynomials. When we extend this process to the manifold setting in the subsequent section, we will obtain a nonlinear target functional due to metric-dependent terms, thus violating the assumptions of Mirzaei's analysis. Nevertheless, we will informally refer to such estimates as *optimal* if they numerically demonstrate convergence consistent with Mirzaei's analysis.

For our purposes, we will consider point clouds of two-dimensional manifolds embedded in $\mathbb{R}^3$. It is easily shown (see e.g. [98]) for the Euclidean setting in $\mathbb{R}^2$ that there exists constants $c_1, c_2 > 0$ such that $c_1 h_{\mathbb{X},\not\leqslant} \leq \frac{1}{\sqrt{n}} \leq c_2 h_{\mathbb{X},\not\leqslant}$, and thus the fill distance scales as $h \sim 1/\sqrt{n}$, where n is the number of points. We will therefore use the notation $\bar{h}^{-1} := \sqrt{n}$ to characterize the refinement of a given quasi-uniform point set.

6.2 GMLS Reconstruction of Geometries from Point Clouds

Consider a smooth manifold $\mathcal{M} \subset \mathbb{R}^d$ and assume a quasi-uniform point cloud representation $\mathbb{X}_h \subset \mathcal{M}$. At each point $\mathbf{x}_i \in \mathbb{X}_h$, we shall construct an

approximation to the tangent space $T_{\mathbf{x}_i}$ [98, 88]. For this purpose, we use a principal component analysis (PCA) of the point set consisting of $\mathbf{x}_i$ and nearby nieghbor points $\mathbf{x}_j$ such that $j \in \mathcal{N}_i$. We define $\mathcal{N}_i = \mathcal{N}_\epsilon(\mathbf{x}_i)$ as the collection of points $\mathbf{x}_j$ that are in an $\epsilon-$ball about $\mathbf{x}_i$, which can be expressed as $\mathcal{N}_\epsilon(\mathbf{x}_i) = \mathbb{X}_h \bigcap B_\epsilon(\mathbf{x}_i)$. To perform PCA we must center the data set and we define the centering point as

$$\bar{\mathbf{x}}_i = \frac{1}{|\mathcal{N}_i|} \sum_{j \in \mathcal{N}_i} \mathbf{x}_j. \tag{6.2.1}$$

We remark that while in general we will have that $\bar{\mathbf{x}}_i \neq \mathbf{x}_i$, these are typically close in practice. We refer to $\mathcal{N}_i = \mathcal{N}_\epsilon(\mathbf{x}_i)$ as the patch of points at $\mathbf{x}_i$. We use for $\mathcal{C}$ in PCA the empirical estimate of the covariance of the patch of points given by

$$\mathcal{C} = \mathrm{Cov}(\{\mathbf{x}_j\}) = \frac{1}{|\mathcal{N}_i|} \sum_{j \in \mathcal{N}_i} (\mathbf{x}_j - \bar{\mathbf{x}}_i) (\mathbf{x}_j - \bar{\mathbf{x}}_i)^\intercal . \tag{6.2.2}$$

This provides in practice a good estimate to the local geometry when we assume that $h_{\mathbb{X}}$ and ϵ are chosen sufficiently small so that the set of points $\mathcal{N}_\epsilon(\mathbf{x}_i)$ is nearly co-planar. We estimate the tangent space $T\mathcal{M}_{\mathbf{x}_i}$ of the manifold using the $(d-1)$-largest eigenvectors of $\mathcal{C}$. These provide when $d = 3$ a basis for the tangent plane that we denote by $\boldsymbol{\psi}_i^1$ and $\boldsymbol{\psi}_i^2$ and normalize to have unit magnitude. These also give the unit normal as $\boldsymbol{\eta}_i = \boldsymbol{\psi}_i^1 \times \boldsymbol{\psi}_i^2$. We show this reconstruction approach in Figure 6.2.

It is important to note that the PCA-approach can arbitrarily assign an orientation in the reconstruction of the tangent space. This can have the undesir-

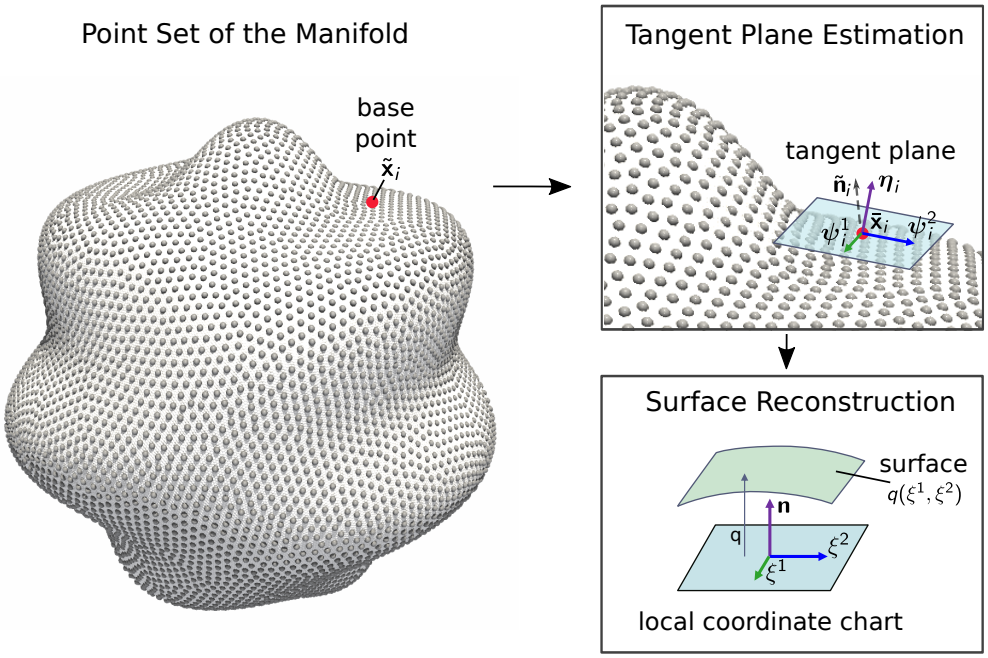

Figure 6.2: GMLS Surface Reconstruction and Local Parameterization. For a manifold represented as a point set, we use a GMLS approach to obtain local patches and coordinate charts for parameterizing the surface. At a given base point $\tilde{\mathbf{x}}$ we collect all neighbors within an ϵ-ball and perform Principle Component Analysis (PCA) to determine a local tangent plane and normal for the surface. We parameterize the surface locally using $(\xi^1, \xi^2, q(\xi^1, \xi^2))$, where we obtain $q(\xi^1, \xi^2)$ by performing a GMLS reconstruction of the surface [9].

able property that neighboring patches have opposite orientations resulting in sign changes for some surface operators, such as the curl. In the general case, globally orienting the surface is a challenging NP-hard problem, as discussed in Wendland [98]. Many specialized algorithms have been proposed for this purpose which are efficient in practice, including front-marching and voronoi-based methods [151, 98]. We shall assume throughout that at each point $\mathbf{x}_i$ there is a reference normal $\tilde{\mathbf{n}}_i$ either determined in advance algorithmically or specified by the user. We take in our PCA procedures that the normals $\boldsymbol{\eta}_i$ are oriented with $\tilde{\mathbf{n}}_i^T \boldsymbol{\eta}_i > 0$.

We use this approach to define a local coordinate chart for the manifold in the vicinity of the base point $\tilde{\mathbf{x}} = \mathbf{x}_i$. For this purpose, we take as the origin the base point $\mathbf{x}_i$ and use the tangent plane bases $\boldsymbol{\psi}_i^2, \boldsymbol{\psi}_i^2$ and normal $\boldsymbol{\eta}_i$ obtained from the PCA procedure. We then define a local coordinate chart using the embedding map $\boldsymbol{\sigma}$

$$\boldsymbol{\sigma}(\xi^1, \xi^2; q) = \mathbf{x}_i + \xi^1 \boldsymbol{\psi}_i^1 + \xi^2 \boldsymbol{\psi}_i^2 + q(\xi^1, \xi^2) \boldsymbol{\eta}_i. \tag{6.2.3}$$

This provides a family of parameterizations in terms of local coordinates (ξ^1, ξ^2), defined by choice of a smooth function q. Without loss of generality we could always define the ambient space coordinates so that locally at a given base point $\tilde{\mathbf{x}}$ we have $\boldsymbol{\sigma} = (\xi^1, \xi^2, q(\xi^1, \xi^2))$. This can be interpreted as describing the surface as the graph of a function over the (ξ^1, ξ^2)-plane where q is the height above the plane, see Figure 6.2. This parameterization is known as the Monge-Gauge repre-

sentation of the manifold surface [152, 4], and we will use GMLS to approximate derivatives of $\boldsymbol{\sigma}$ through the following choices:

- We take for our sampling functionals $\Lambda = \{\lambda_j\}_{j=1}^N$ point evaluations $\lambda_j = \delta_{\mathbf{x}_i}$ at all points $\mathbf{x}_j$ in the ϵ-ball neighborhood $\mathcal{N}_i$ of $\mathbf{x}_i$.

- We use the target functional $\tau^{[\boldsymbol{\alpha}]}$ is the point evaluation of the derivative $\mathcal{D}^{\boldsymbol{\alpha}}\boldsymbol{\sigma}$ at $\mathbf{x}_i$, where $\mathcal{D}^{\boldsymbol{\alpha}}$ denotes the partial derivative of $\boldsymbol{\sigma}$ in $\{\xi^c\}$ described by the multi-index $\boldsymbol{\alpha}$ [153].

- We take for the reconstruction space the collection of m_1^{th}-order polynomials.

- We use for our weighting function the kernel in equation 6.1.5 with support matching the parameter ϵ used for selecting neighbors in our reconstruction and for defining our ϵ-graph on the point set.

We use these point estimates of the derivative of $\boldsymbol{\sigma}$ to evaluate non-linear functionals of $\boldsymbol{\sigma}$ characterizing the geometry of the manifold. Consider the metric tensor

$$g_{ab} = \langle \boldsymbol{\sigma}_{\xi^a}, \boldsymbol{\sigma}_{\xi^b} \rangle_g. \tag{6.2.4}$$

The $\langle \mathbf{a}, \mathbf{b} \rangle_g$ corresponds to the usual Euclidean inner-product $\mathbf{a} \cdot \mathbf{b}$ when the vectors $\boldsymbol{\sigma}_{\xi^c} = \partial\boldsymbol{\sigma}/\partial\xi^c$ are expressed in the basis of the ambient embedding space. Other geometric quantities can be similarly calculated from this representation once estimates of $\mathcal{D}^{\boldsymbol{\alpha}}\boldsymbol{\sigma}$ are obtained.

6.3 Monge Gauge Differential Geometry

To compute in practice the action of our operators during the GMLS reconstruction of the geometry of the manifolds or differential operators on scalar and vector fields on the surface, we use local Monge-Gauge parameterizations of the surface. To obtain high-order accuracy we further expand expressions involving derivatives of the metric and other fields explicitly using symbolic algebra packages, such as Sympy [144]. This allows us to avoid some of the tedium notorous in differential geometry to compute on-the-fly needed expressions for computing the action of our operators. We summarize here the basic differential geometry of surfaces expressed in the Monge-Gauge and the associated expressions we use in such calculations.

In the Monge-Gauge we parameterize locally a smooth surface in terms of the tangent plane coordinates u, v and the height of the surface above this point as the function $h(u, v)$. This gives the embedding map

$$\mathbf{x}(u, v) = \boldsymbol{\sigma}(u, v) = (u, v, \mathbf{h}(u, v)). \tag{6.3.1}$$

We see that this parameterization of the surface is closely related to equation 6.2.3. We can use the Monge-Gauge equation 6.3.1 to derive explicit expressions for geometric quantities. The derivatives of $\boldsymbol{\sigma}$ provide a basis ∂_u, ∂_v for the tangent

space as

$$\partial_u = \boldsymbol{\sigma}_u(u,v) \;=\; (1, 0, \mathbf{h}_u(u,v)) \tag{6.3.2}$$

$$\partial_v = \boldsymbol{\sigma}_v(u,v) \;=\; (0, 1, \mathbf{h}_v(u,v)). \tag{6.3.3}$$

The first fundamental form **I** (metric tensor) and second fundamental form **II** (curvature tensor) are given by

$$\mathbf{I} = \begin{bmatrix} E & F \\ F & G \end{bmatrix} = \begin{bmatrix} \boldsymbol{\sigma}_u \cdot \boldsymbol{\sigma}_u & \boldsymbol{\sigma}_u \cdot \boldsymbol{\sigma}_v \\ \boldsymbol{\sigma}_v \cdot \boldsymbol{\sigma}_u & \boldsymbol{\sigma}_v \cdot \boldsymbol{\sigma}_v \end{bmatrix} = \begin{bmatrix} 1 + \mathbf{h}_u(u,v)^2 & \mathbf{h}_u\mathbf{h}_v(u,v) \\ \mathbf{h}_u(u,v)\mathbf{h}_v(u,v) & 1 + \mathbf{h}_v(u,v)^2 \end{bmatrix}. \tag{6.3.4}$$

and

$$\mathbf{II} = \begin{bmatrix} L & M \\ M & N \end{bmatrix} = \begin{bmatrix} \boldsymbol{\sigma}_{uu} \cdot \boldsymbol{n} & \boldsymbol{\sigma}_{uv} \cdot \boldsymbol{n} \\ \boldsymbol{\sigma}_{vu} \cdot \boldsymbol{n} & \boldsymbol{\sigma}_{vv} \cdot \boldsymbol{n} \end{bmatrix} = \frac{1}{\sqrt{1 + \mathbf{h}_u^2 + \mathbf{h}_v^2}} \begin{bmatrix} \mathbf{h}_{uu} & \mathbf{h}_{uv} \\ \mathbf{h}_{uv} & \mathbf{h}_{vv} \end{bmatrix}. \tag{6.3.5}$$

The $\mathbf{n}$ denotes the outward normal on the surface and is given by

$$\boldsymbol{n}(u,v) = \frac{\boldsymbol{\sigma}_u(u,v) \times \boldsymbol{\sigma}_v(u,v)}{\|\boldsymbol{\sigma}_u(u,v) \times \boldsymbol{\sigma}_v(u,v)\|} = \frac{1}{\sqrt{1 + \mathbf{h}_u^2 + \mathbf{h}_v^2}}(-\mathbf{h}_u, -\mathbf{h}_v, 1). \tag{6.3.6}$$

We use throughout the notation for the metric tensor $\mathbf{g} = \mathbf{I}$ interchangeably. In practical calculations whenever we need to compute the action of the inverse metric tensor this should be done with numerical linear algebra (Gaussian elimination with pivoting) [133, 134]. For notational convenience, we use the tensor notation for the metric tensor g_{ij} and for its inverse g^{ij}. These correspond to the first and second fundamental forms as

$$g_{ij} = [\mathbf{I}]_{i,j}\,, \quad g^{ij} = \left[\mathbf{I}^{-1}\right]_{i,j}. \tag{6.3.7}$$

For the metric tensor $\mathbf{g}$, we also use the notation $|g| = \det(\mathbf{g})$ and have that

$$\sqrt{|g|} = \sqrt{\det(\mathbf{I})} = \sqrt{1 + \mathbf{h}_u^2 + \mathbf{h}_v^2} = \|\vec{\sigma}_u(u,v) \times \vec{\sigma}_v(u,v)\|. \tag{6.3.8}$$

The provides the local area element as $dA_{u,v} = \sqrt{|g|}dudv$. To compute quantities associated with curvature of the manifold we construct the Weingarten map [4] which can be expressed as

$$\mathbf{W} = \mathbf{I}^{-1}\mathbf{II}. \tag{6.3.9}$$

The Gaussian curvature K can be expressed in the Monge-Gauge as

$$K(u,v) = \det\left(\mathbf{W}(u,v)\right) = \frac{\mathbf{h}_{uu}\mathbf{h}_{vv} - \mathbf{h}_{uv}^2}{(1 + \mathbf{h}_u^2 + \mathbf{h}_v^2)^2}. \tag{6.3.10}$$

For further discussions of these tensors and more generally the differential geometry of manifolds see [4, 80, 3]. We use these expressions as the basis of our calculations of the action of our surface operators.

6.4 GMLS Approximations of Surface Operators

We now show how to formulate GMLS problems to recover estimates of the metric tensor and other geometric quantities associated with the shape of the manifold. The metric tensor and geometric quantities must first be extracted from the point cloud representation of the manifold, and may then be used in the approximation of differential operators on the surface.

6.4.1 GMLS Reconstructions of Our Manifold Geometries

We now utilize this process to estimate Gaussian curvature, as a representative geometric quantity of interest, which we will later need to discretize the Stokes equations. To demonstrate in practice the convergence behavior of our techniques as the fill-distance is refined, we consider the four example manifolds shown in Figure 6.3.

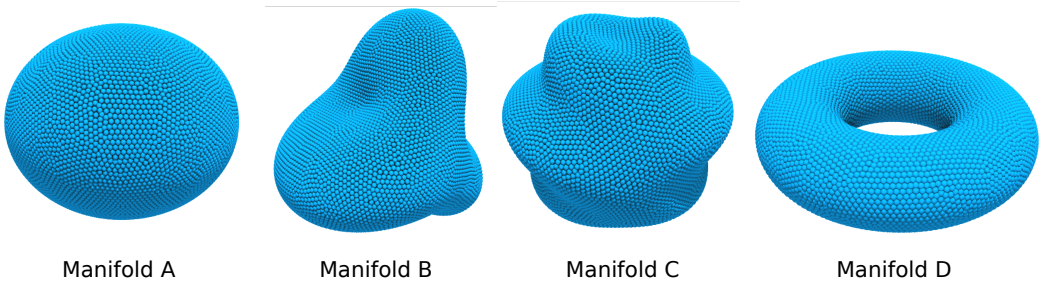

Figure 6.3: Point Set Representations of Manifolds. Manifold A is an ellipsoid defined by the equation $x^2/a^2 + y^2/b^2 + z^2 = s_0^2$ with $a = 1.2, b = 1.2, s_0^2 = 1$. Manifold B is a radial manifold defined in spherical coordinates by $(\theta, \phi, r(\theta, \phi)$ where $r(\theta, \phi) = 1 + r_0 \sin(3\phi)\cos(\theta)$ with $r_0 = 0.1$. Manifold C is a radial manifold defined in spherical coordinates by $(\theta, \phi, r(\theta, \phi)$ where $r(\theta, \phi) = 1 + r_0 \sin(7\phi)\cos(\theta)$ with $r_0 = 0.1$. Manifold D is a torus defined by the equation $(s_1^2 - \sqrt{x^2 + y^2})^2 + z^2 = s_2^2$ with $s_1^2 = 0.7, s_2^2 = 0.3$. Each of the manifolds shown are represented by quasi-uniform point sets with approximately $n = 10^4$ samples. For quasi-uniform sampling we expect the fill-distance h to scale as $h \sim 1/\sqrt{n}$. When reporting our results, we use throughout the notation $\bar{h}^{-1} = \sqrt{n}$. We discuss further details of the point sampling of the manifolds in Section 7.0.1.

We utilize the Weingarten map $\mathbf{W} = \mathbf{I}^{-1}\mathbf{II}$ to estimate the Gaussian curvature via the formula $K = \det(\mathbf{W})$ when using the GMLS estimate of $\boldsymbol{\sigma}_{\xi^c}$ to calculate $\mathbf{I}$ and $\mathbf{II}$, as in Equation 6.3.10. We investigate the convergence of the estimated curvature to analytic results for the manifolds A-D, shown in Figure 6.4. We plot the estimated curvature on the surface of each of the manifolds in Figure 6.5. We tabulate the results in Table 6.1. We find our GMLS methods with $m = 6$ yields approximations having 5^{th}-order accuracy. While there is currently no convergence theory for our non-linear estimation procedure, the results for $k = 2$ for Gaussian Curvature are consistent with the suggestive predictions $m + 1 - k$ similar to equation 6.1.9.

	Manifold A		**Manifold B**		**Manifold C**			**Manifold D**	
h	ℓ_2**-error**	**Rate**	ℓ_2**-error**	**Rate**	ℓ_2**-error**	**Rate**	**h**	ℓ_2**-error**	**Rate**
0.1	2.1351e-04	-	1.1575e-01	-	1.2198e-01	-	.08	5.5871e-02	-
0.05	3.0078e-06	6.07	1.6169e-02	2.84	4.7733e-03	4.67	.04	6.5739e-04	6.51
0.025	5.3927e-08	5.77	8.3821e-04	4.26	1.6250e-04	4.88	.02	1.3418e-05	5.67
0.0125	1.1994e-09	5.48	2.3571e-05	5.14	4.5204e-06	5.17	.01	3.1631e-07	5.37

Table 6.1: Convergence of GMLS Approximation of the Gaussian Curvature K. The GMLS reconstruction of the manifold is used with polynomial order $m_1 = 6$. Our GMLS methods involve operations with $k_1 = 2^{nd}$-order differentiation. We find $\sim 5^{th}$-order asymptotic convergence rate. The target sampling distance h is discussed in Section 7.0.1.

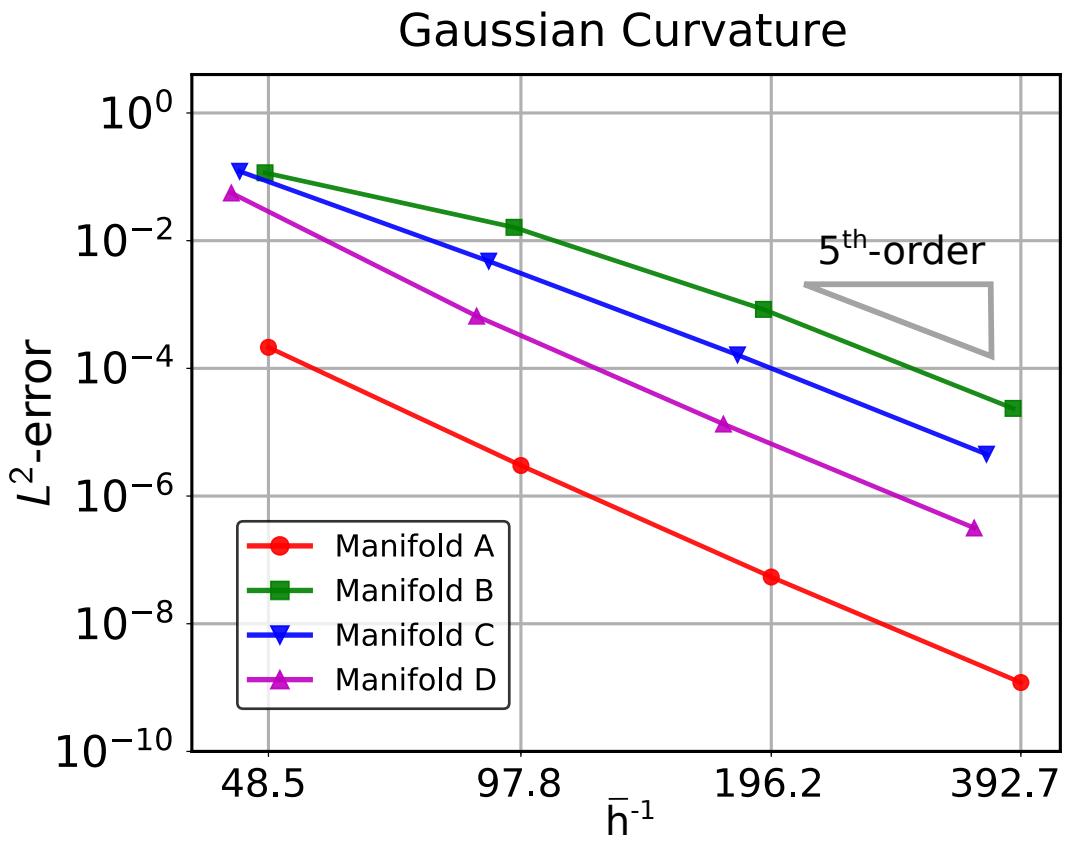

Figure 6.4: GMLS Estimate of the Gaussian Curvature vs Point Set Resolution. We show on log-log scale the convergence of the GMLS-based estimation of Gaussian Curvature as the number of sample points is increased. The $\bar{h}^{-1} = \sqrt{n}$, where n is the number of points. Manifold B and Manifold C present the greatest challenge given localized regions of particularly large Gaussian Curvatures, see Figure 6.5. We find the accuracy is 5^{th}-order in agreement with the suggestive prediction $m + 1 - k$ similar to equation 6.1.9, where in our GMLS approximation $m = 6, k = 2$, see Table 6.1.

6.4.2 GMLS Approximations of Geometry-Dependent Operators

We finally have the requisite information to perform GMLS estimates of differential operators on the manifold. We consider the approximation of a target functional which may depend nonlinearly upon the estimate of the inverse metric tensor. Consider as an example the Laplace-Beltrami operator, which may be expressed in local coordinates as

$$\Delta_{LB}\phi = \frac{1}{\sqrt{|g|}}\partial_i\left(\sqrt{|g|}g^{ij}\partial_j\phi\right). \tag{6.4.1}$$

We assume an estimate of $\mathbf{g}$ to be calculated at each particle following the process outlined in the previous sections. We then approximate the action of

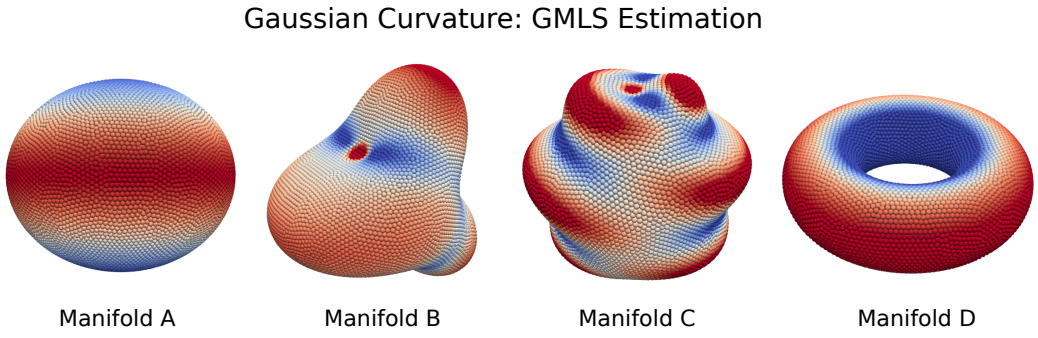

Figure 6.5: Gaussian Curvature from GMLS Estimation. We use a GMLS reconstruction approach to estimate the Gaussian Curvature of each of the manifolds using Equation 6.3.10. Shown are results for the case of a quasi-uniform sampling of the surface with approximately $n = 10^4$ samples for each manifold. We show the L^2-error of the GMLS approximation of the Gaussian curvature and convergence rate in Figure 6.4.

the operator on scalar and vector fields through the following GMLS approach. First, we find locally the best approximating reconstruction $\mathbf{P}$ of the scalar or vector field components on the manifold. In the second, we apply the target functional for the differential operator to $\mathbf{P}$ using geometric quantities from our initial GMLS reconstruction of the manifold. This can be expressed as

$$\tau^h_{\tilde{\mathbf{x}}}(\phi) = \tau_{\tilde{\mathbf{x}}}(\mathbf{P})^\intercal a_{\tilde{\mathbf{x}}}(u). \tag{6.4.2}$$

The optimal coefficient vector a is given by.

$$a_{\tilde{\mathbf{x}}}(u) = \left(\Lambda(\mathbf{P})^\intercal \mathbf{W} \Lambda(\mathbf{P})\right)^{-1} \Lambda(\mathbf{P})^\intercal \mathbf{W} \Lambda(u). \tag{6.4.3}$$

We note that in the general setting, the sampling functionals λ_j may also depend nonlinearly upon the geometric information. In the case where λ_j are selected as point samples however the sampling functionals are in fact linear.

We remark that the two components $a_{\tilde{\mathbf{x}}}(u)$ and $\tau_{\tilde{\mathbf{x}}}(\mathbf{P})$ encode different types of information about the approximation. The $\tau_{\tilde{\mathbf{x}}}(\mathbf{P})$ encodes the action of the target functional on the basis for the space $\mathbb{V}_h$. The $a_{\tilde{\mathbf{x}}}(u)$ encodes the reconstruction of the function u by the best approximating function p^* in $\mathbb{V}_h$ according to the best match between the sampling functionals λ_j acting on u and p^*, see equation 6.1.4. As a consequence, for each of the target operators τ, the $a_{\tilde{\mathbf{x}}}(u)$ will not change since this term only depends on the function u. As a result, we need only compute fresh for each operator the $\tau_{\tilde{\mathbf{x}}}(\mathbf{P})$ which represents how the differential operator on the manifold acts on the function space $\mathbb{V}_h$.

As a summary our GMLS approximation of the operators on the manifold involve the following steps

- We take $\Lambda = \{\lambda_j\}_{j=1}^N$ with $\lambda_j = \delta_{\mathbf{x}_j}$ the point evaluations of $\lambda_j \phi = \phi(\mathbf{x}_j)$ for $\mathbf{x}_j$ in the neighborhood $j \in \mathcal{N}_i$ around the point $\mathbf{x}_i$.

- We use target functionals τ for surface differential operators by utilizing for evaluation the parameterization and approximate metric tensor.

- We take the reconstruction space $\mathbb{V}_h$ by selecting the collection of m_2^{th}-order polynomials $p(x, y)$ over $\mathbb{R}^2$ where m_2 is an integer parameter for the maximum degree.

- We use the weight function $\omega(\lambda_j, \tau_{\mathbf{x}_i}) = w(\|\mathbf{x}_j - \mathbf{x}_i\|)$ by selecting a positive kernel $w(r)$ with support contained within an ϵ-ball of $\mathbf{x}_i$. We also shall use ϵ to define an ϵ-graph on the points.

We remark that the reconstruction space $\mathbb{V}_h$ consists of polynomials of order m_2 which need not be chosen to be the same order as in the geometric reconstructions. In general we can choose $m_2 \neq m_1$, however, in practice given that the operators on the manifold often involve differentiating geometric quantities we will typically need in practice to choose $m_1 \geq m_2$ to achieve convergence.

As an illustration of our approach, we discuss in detail our GMLS approximation of the Laplace-Beltrami operator. The other differential operators for the manifold follow similarly, but have much more complicated expressions which

we evaluate symbolically. The Laplace-Beltrami operator can be expressed in coordinates as

$$\Delta_{LB}\phi = \frac{1}{\sqrt{|g|}}\partial_i\left(\sqrt{|g|}g^{ij}\partial_j\phi\right). \tag{6.4.4}$$

To obtain an approximation at the base point $\tilde{\mathbf{x}}$, we compute the action of the operator on the space $\mathbb{V}_h$ to obtain the representation

$$\tau_{\tilde{\mathbf{x}}}(\mathbf{P};\mathbf{g}) = \frac{1}{\sqrt{|g|}}\partial_i\left(\sqrt{|g|}g^{ij}\partial_j\mathbf{P}\right), \tag{6.4.5}$$

where $\mathbf{P}$ represents the vector of basis functions of $\mathbb{V}_h$ and the differentials act component-wise.

It is necessary to consider how to choose a reconstruction space $\mathbb{V}_h$ of sufficient richness that a differential operator on the manifold $\mathcal{L}_{\mathbf{g}}$ can be adequately captured. For instance, a differential operator of order k should have a polynomial space of order m_2 satisfying $m_2 \geq k$, as suggested by the bounds in equation 6.1.9. Further, larger choices of m_2 will necessitate a larger kernel support to ensure unisolvency therefore solvability of the GMLS problem. As may be expected, this suggests that GMLS will perform better having more accuracy and requiring less computational effort when working with lower order differential operators. Therefore, we should prefer schemes which avoid higher order differential operators whenever possible. As we shall discuss in Chapter 7, this can be achieved to some extent by splitting equations into systems of lower order equations or by choosing alternative formulations.

Chapter 7

Convergence of our GMLS Methods

We numerically solve for the velocity of the hydrodynamic flow based on equations 7.1.1 or 7.1.2 using the GMLS approximations detailed in Chapter 6 and [9]. We briefly discuss the overall steps used in our numerical methods to obtain solutions. We formulate the hydrodynamics using a vector-potential formulation to obtain a gauge that intrinsically enforces the incompressibility constraints of the flow appearing in equation 2.5.3. For steady-state hydrodynamic flows, we derived conditions for the vector potential of the flow resulting in equation 7.1.1. We summarize the steps used in our solution approach in Figure 7.1.

To determine numerically the hydrodynamic flow in response to a body force density $\mathbf{b}$ acting on the surface fluid, in our approach, we first convert force fields into co-variant form $\mathbf{b}^\flat$. We next use our exterior calculus formulation of the generalized curl to obtain the corresponding vector-potential for the body force

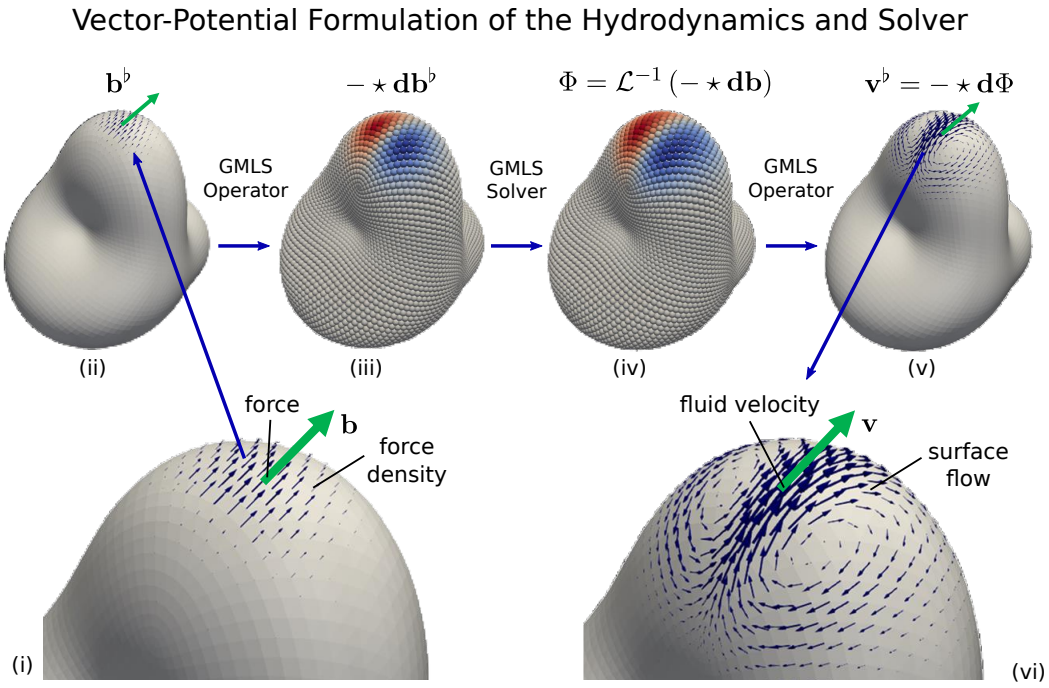

Figure 7.1: Approach for Computing Numerically the Surface Hydrodynamic Flows. For a given body force density or stresses $\mathbf{b}$ acting on the surface fluid we convert the fields to covariant form $\mathbf{b}^\flat$, shown in (i),(ii). To handle incompressibile flows, we convert all fields to a divergence-free gauge using the generalized surface curl $-\star\,\mathbf{d}\mathbf{b}^\flat$, shown in (iii). We solve for the vector potential Φ of the surface hydrodynamic flow using equations 7.1.1 or 7.1.2 and our GMLS collocation methods for the differential operators, shown in (iv). We construct the covariant form of the velocity field of the hydrodynamic flow response using the generalized surface curl $\mathbf{v}^\flat$, shown in (v). We obtain our final results by converting the covariant form $\mathbf{v}^\flat$ to the velocity field by $\mathbf{v} = \left(\mathbf{v}^\flat\right)^\sharp$. This yields the surface hydrodynamic flow shown in (vi) [9].

$\Psi = \mathcal{C}_1 \mathbf{b}^\flat$ where $\mathcal{C}_1 = - \star \mathbf{d}$ acts on 1-forms. We numerically compute $\Psi = \tilde{C}_1 \mathbf{b}^\flat$ where $\tilde{C}_1$ is our GMLS approximation of the curl operator $\mathcal{C}_1$.

We will utilize equation 7.1.1 to specify the differential equation for the steady-state velocity response. We use GMLS to assemble in strong form a stiffness matrix A using a collocation approach. The full differential operator that appears on the left-hand-side is computed at each base point $\tilde{\mathbf{x}}$ of the point set of the manifold. This results in the system of equations linear in $\tilde{\mathbf{\Phi}}$

$$A\tilde{\mathbf{\Phi}} = \tilde{C}_0 \mathbf{b}. \tag{7.0.1}$$

We solve the large linear system using GMRES with algebraic multigrid (AMG) preconditioning.

The velocity field is given from the vector potential Φ by the generalized surface curl operator $\mathbf{v}^\flat = \mathcal{C}_0 \Phi$, where $\mathcal{C}_0 = - \star \mathbf{d}$ acts on 0-forms. From the solution $\tilde{\mathbf{\Phi}}$ of equation 7.0.1, we construct numerically the co-variant velocity field of the flow using $\tilde{\mathbf{v}}^\flat = \tilde{C}_0 \tilde{\mathbf{\Phi}}$. The $\tilde{C}_0$ is our GMLS approximation of the generalized curl operator $\mathcal{C}_0$. Finally, using the metric tensor obtained from the GMLS reconstruction, we obtain the surface velocity field $\tilde{\mathbf{v}}$ by converting the covariant field $\mathbf{v}^\flat$ into the contravariant field by $\tilde{\mathbf{v}} = \left(\tilde{\mathbf{v}}^\flat\right)^\sharp$. We use this approach to numerically compute incompressible hydrodynamic flows in response to applied driving forces or stresses acting on the surface fluid. We remark that our approach can also be combined with other computational methods and solvers to compute coupling to bulk three dimensional hydrodynamics or more generally for resolving

in other physical systems interactions that occur at interfaces having non-trivial geometries.

All tangent plane approximations, local chart calculations, and GMLS problems were set up and solved using the Compadre toolkit [109]. We were able to extend the capability of the toolkit by implementing our symbolically generated target operators into it. The toolkit provides domain decomposed distributed vector representation of fields as well as global matrix assembly. Through the Compadre toolkit, we had access to iterative block solvers (Belos [154]), block preconditioners (Teko) and AMG preconditioning (MueLu [155, 156]), all in the Trilinos software framework [157].

7.0.1 Manifold Point Cloud Refinements Used

We provide a summary of the sampling resolution h used for each of the manifolds in Table 7.1. We refer to h as the *target fill distance*. For each of the manifolds, we achieve a nearly uniform collection of the points as in equation 6.1.3 using the DistMesh code [158]. We emphasize this approach was used only for convenience to obtain quasi-uniform samplings and other sampling techniques can also be utilized for this purpose of representing the manifolds. We specify h and the algorithm produces a point sampling of the manifold. In practice, we have found this yields a point spacing with neighbor distances varying by

only $\approx \pm 30\%$ relative to the target distance h. We summarize for each of the manifolds how this relates to the number of sample points n in Table 7.1.

Refinement Level	**A**: h	n	**B**: h	n	**C**: h	n	**D**: h	n
1	.1	2350	.1	2306	.1	2002	.08	1912
2	.05	9566	.05	9206	.05	7998	.04	7478
3	.025	38486	.025	36854	.025	31898	.02	29494
4	.0125	154182	.0125	147634	.0125	127346	.01	118942

Table 7.1: Sampling Resolution for each of the Manifolds A–D. Relation between the target distance h and the number of sample points n used for each of the manifolds. In each case, the neighbor distances between the points sampled were within $\approx \pm 30\%$ of the target distance h.

7.1 Optimizing The Stokes Equation for GMLS

7.1.1 Biharmonic Formulation of the Hydrodynamics

As discussed in Chapter 2, we can formulate the hydrodynamics equations 2.5.3 in terms of an unconstrained equation for the scalar vector potential Φ. We substitute equation 2.6.3 into equation 2.5.3 and apply the generalized curl operator $\text{curl}_{\mathcal{M}} = - \star \mathbf{d}$ to both sides. This gives the biharmonic hydrodynamic equations on the surface

$$-\mu_m \Delta_H^2 \Phi - \gamma \Delta_H \Phi - 2\mu_m (- \star \mathbf{d}(K(- \star \mathbf{d})))\Phi \;\; = \;\; - \star \mathbf{d}\mathbf{b}^\flat. \qquad (7.1.1)$$

The Hodge Laplacian now acts on 0-forms as $\Delta_H \Phi = \boldsymbol{\delta}\mathbf{d}\Phi$ and is related the surface Laplace-Beltrami operator by $\Delta_H \Phi = -\Delta_{LB}\Phi$. As before, μ_m is the

surface shear viscosity, γ the drag with the surrounding bulk fluid, and K the Gaussian curvature of the manifolds. The $\mathbf{b}^\flat$ is the covariant form for the body force acting on the fluid. We see the pressure term no longer plays a role relative to equation 2.5.3.

We shall refer in our numerical methods to this approach to the hydrodynamics as the *biharmonic formulation*. Additional discussion of this formulation of the hydrodynamics can be found in our previous papers [6, 8].

7.1.2 Split Formulation of the Hydrodynamics

While the equation 7.1.1 is expressed in terms of biharmonic operators, for numerical purposes we can reformulate the problem by splitting it into two subproblems each of which only involve the Hodge Laplacian. This is helpful since for our numerical methods this would require us to only need to resolve second order operators with our GMLS approximations. This has the practical benefit of greatly reducing the size of the GMLS stencil sizes (ϵ-neighborhoods) required for unisolvency for the operator as discussed in Section 6.4.2.

We reformulate the hydrodynamic equations by defining $\Psi = \Delta_H \Phi$, which allows us to split the action of the fourth-order biharmonic operator into two equations involving only second- order Hodge Laplacian operators as

$$-\mu_m \Delta_H \Psi - \gamma \Psi - 2\mu_m(- \star \mathbf{d}(K(- \star \mathbf{d})))\Phi = - \star \mathbf{d}\mathbf{b}^\flat. \quad (7.1.2)$$

$$\Delta_H \Phi - \Psi = 0. \quad (7.1.3)$$

As we shall discuss, the lower order of the differentiation has a number of benefits even thought we incur the extra issue of dealing with a system of equations. This reformulation results in less sensitivity to errors in the underlying approximations in the GMLS reconstructions of the geometry and surface fields. This reformulation also requires much less computational effort and memory when assembling the stiffness matrices since the lower order permits use of smaller ϵ-neighborhoods to achieve unisolvency as discussed in Section 6.4.2. We refer to this reformulation of the hydrodynamic equations as the *split formulation*.

7.2 Convergence of Surface Operators in GMLS

We investigate the convergence of the operators required to solve these hydrodynamic equations. An important consideration is that our target functionals involve a non-linear dependence on the geometry. This results in approximations that arise from two different GMLS procedures. The first is the GMLS reconstruction of the geometry of the manifold from the sampled point set and the calculation of associated geometric quantities. The second is the GMLS approximation of differential operators acting on the surface scalar and vector fields.

To solve the hydrodynamic flows on the surface as formulated in equation 7.1.1 and 7.1.2, we require the following operators

- Laplace-Beltrami Operator: $\mathcal{L}_{LB} = -\Delta_H = -\mathbf{d}\boldsymbol{\delta}$.

- Biharmonic Operator: $\mathcal{L}_{BH} = \mathcal{L}_{LB}^2 = \Delta_H^2$.
- Curvature Operator: $\mathcal{L}_K = curl_{\mathcal{M}}\left(K \cdot curl_{\mathcal{M}}\right) = - \star \mathbf{d}\left(K \cdot (- \star \mathbf{d}\right)$.
- Surface Curl $\mathcal{C}_0$ for 0-Forms: $\mathcal{L}_{C0} = \text{curl}_{\mathcal{M}}\Phi = - \star \mathbf{d}_0$.
- Surface Curl $\mathcal{C}_1$ for 1-Forms: $\mathcal{L}_{C1} = \text{curl}_{\mathcal{M}}\mathbf{v} = - \star \mathbf{d}_1$.

We mention that in the case of the split formulation of the hydrodynamic equation 7.1.2 this simplifies slightly, and we no longer need to compute numerically $\mathcal{L}_{BH}$.

To study the accuracy of our GMLS approximation of these operators, we investigate the action of these operators when acting on the test scalar field $\Phi(\mathbf{X}) = \Phi(x, y, z) = z(x^4 + y^4 - 6x^2y^2)$ and test vector field $\mathbf{v}^\flat = \mathcal{C}_0\Phi = - \star \mathbf{d}_0\Phi$. The function we have chosen $\Phi(x, y, z)$ is in fact a smooth continuation of a spherical harmonic mode to the full space $\mathbb{R}^3$. Since our manifolds $\mathcal{M}$ are smooth, we can obtain a smooth surface scalar field Φ by simple evaluation of the function $\Phi(\mathbf{X})$ on the surface. More formally, this would correspond to using the inclusion map $\iota : \mathbb{R}^3 \hookrightarrow \mathcal{M}$ to obtain $\Phi(\mathbf{x}) = \iota_{\mathbf{x}}\Phi(\cdot)$. We find this approach convenient since it provides a way for us to define scalar fields and vector fields independent of coordinate charts on the manifold.

We investigate the accuracy of the GMLS approximation of these operators. We study the ℓ^2-errors

$$\epsilon_{op0} = \left\| \tilde{L}_{\mathbf{g}}\Phi - \mathcal{L}_{\mathbf{g}}\Phi \right\|_2 \tag{7.2.1}$$

$$\epsilon_{op1} = \left\| \tilde{L}_{\mathbf{g}}\mathbf{v} - \mathcal{L}_{\mathbf{g}}\mathbf{v} \right\|_2 . \tag{7.2.2}$$

The ℓ^2-norm is computed by averaging the error over all n sample points of the manifold $\|u-v\|_2^2 = \frac{1}{n}\sum_i \left(u(\mathbf{x}_i) - v(\mathbf{x}_i)\right)^2$. The $\tilde{L}_{\mathbf{g}}$ denotes the numerical GMLS approximation of the operator $\mathcal{L}_{\mathbf{g}}$. In practice, we evaluate to high precision the action of the operators $\mathcal{L}_{\mathbf{g}}$ for the purposes of the convergence studies by using symbolic calculations using SymPy [144]. In general, we emphasize that such

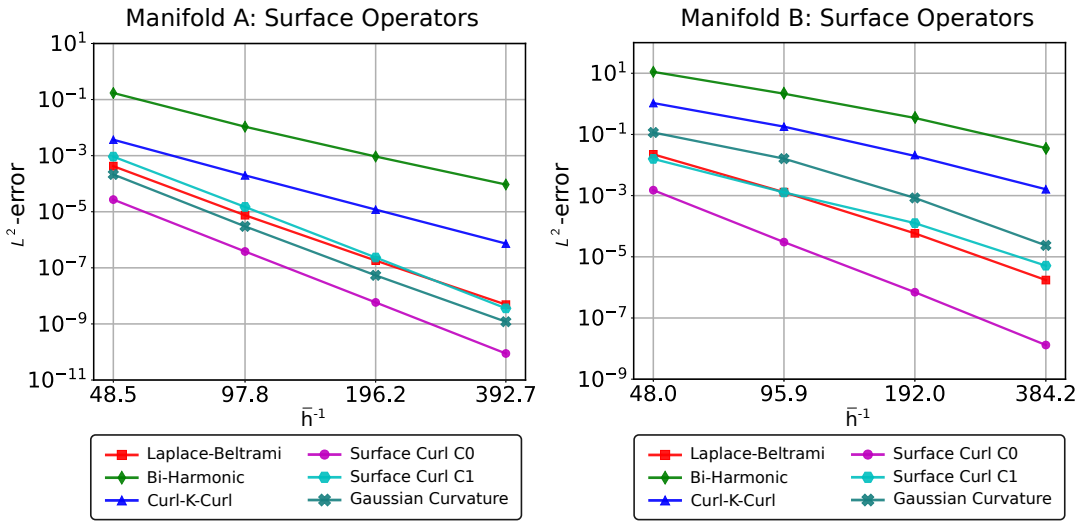

Figure 7.2: GMLS Approximation of Operators vs Resolution. We show log-log plot of the L^2-error of the GMLS approximation of the surface operators with $m_1 = m_2 = 6$. We find in each case our GMLS numerical methods converge with a high order of accuracy in $\bar{h}$ as reported in Table 7.2– 7.4 [9].

calculations of expressions symbolically is prohibitive. What makes these symbolic calculations tractable here is that both the manifold geometry and surface fields we have chosen are symbolically representable using elementary functions for which we have relatively brief initial expressions. Using this approach, we investigate the accuracy of the GMLS approximation of the operators for each of the manifolds in Figures 7.2–7.3.

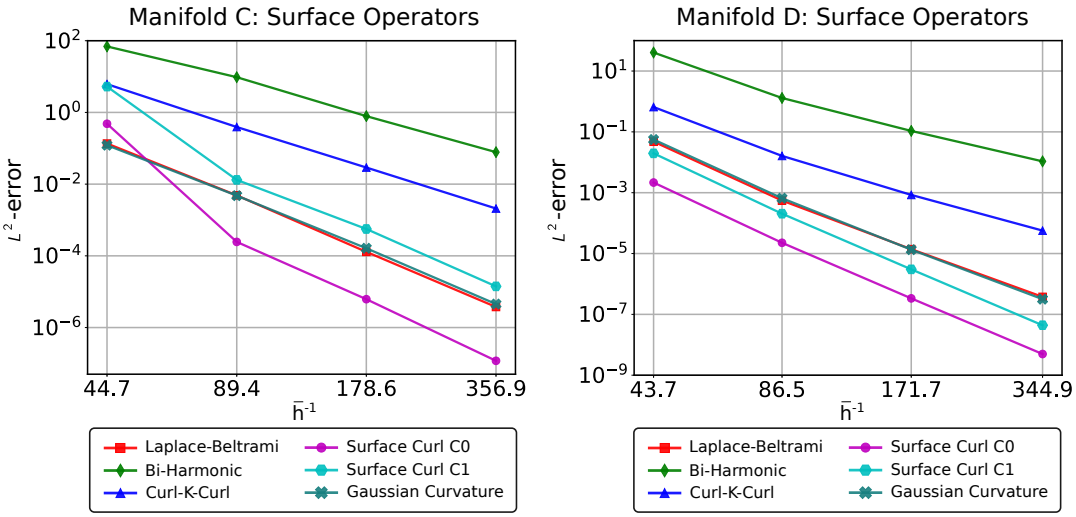

Figure 7.3: GMLS Approximation of Operators vs Resolution. We show log-log plot of the L^2-error of the GMLS approximation of the surface operators with $m_1 = m_2 = 6$. We find in each case our GMLS numerical methods converge with a high order of accuracy in $\bar{h}$ as reported in Table 7.2– 7.4 [9].

We report tabulated results for these convergence studies in Table 7.2– 7.4. We estimate approximate convergence rates by fitting in the log-log plot the error between the reported h value and the previous h value. While there is no theory given that the operators have a non-linear dependence on the manifold

geometry, we do have the suggestive predictions that for an operator of order k and GMLS approximation of order m the convergence might be expected to be on the order $m+1-k$ similar to equation 6.1.9. Since our GMLS methods involve approximations both of the geometry and the surface fields, for purposes of most of the comparisons we take $k = \max(k_1, k_2)$ and $m = \max(m_1, m_2)$. The k_1 denotes the order of the differentiation involved in obtaining the quantities associated with the geometry and k_2 with the order of differentiation of the surface fields. The m_1, m_2 are the polynomial orders used for the approximations for the manifold geometry and surface fields, as discussed in Section 6.4.2.

	Manifold A		**Manifold B**		**Manifold C**			**Manifold D**	
h	**ℓ_2-error**	**Rate**	**ℓ_2-error**	**Rate**	**ℓ_2-error**	**Rate**	**h**	**ℓ_2-error**	**Rate**
0.1	4.2208e-04	-	2.2372e-02	-	1.3580e-01	-	.08	4.7880e-02	-
0.05	7.503e-06	5.74	1.2943e-03	4.11	4.8597e-03	4.80	.04	5.5252e-04	6.54
0.025	1.8182e-07	5.34	5.8300e-05	4.46	1.2928e-04	5.24	.02	1.3877e-05	5.36
0.0125	4.8909e-09	5.21	1.7364e-06	5.06	3.7508e-06	5.11	.01	3.7568e-07	5.17

Table 7.2: Convergence of GMLS Approximation of the Laplace-Beltrami Operator $\mathcal{L}_{LB}$. We use GMLS with $(k = 2, m = 6)$ and find the methods have $\sim 5^{th}$-order asymptotic convergence. The target sampling distance h is discussed in Section 7.0.1.

We find to a good approximation our GMLS methods exhibit convergence rates in agreement with the suggestive prediction $m+1-k$. For the Laplace-Beltrami operator $\mathcal{L}_{LB}$ with $(k = 2, m = 6)$, we find $\sim 5^{th}$-order convergence rate, see Table 7.2. For the Biharmonic operator $\mathcal{L}_{BH}$ with $(k = 4, m = 6)$, we find 3^{rd}-order convergence rate, see Table 7.3. In the case of the Curvature Operator $\mathcal{L}_K$ we have $(k_1 = 3, k_2 = 2, m = 6)$. The $k_1 = 3$ arises since the operator

	Manifold A		Manifold B		Manifold C			Manifold D	
h	**ℓ_2-error**	**Rate**	**ℓ_2-error**	**Rate**	**ℓ_2-error**	**Rate**	**h**	**ℓ_2-error**	**Rate**
0.1	1.7177e-01	-	1.1102e+01	-	6.9226e+01	-	.08	4.0566e+01	-
0.05	1.0768e-02	3.94	2.1455e+00	2.37	9.6017e+00	2.85	.04	1.3004e+01	5.04
0.025	9.3281e-04	3.51	3.4556e-01	2.63	7.8738e-01	3.61	.02	1.0736e-01	3.63
0.0125	9.3585e-05	3.31	3.5904e-02	3.26	7.7925e-02	3.34	.01	1.0722e-02	3.30

Table 7.3: Convergence of GMLS Approximation of the Biharmonic Laplace-Beltrami Operator $\mathcal{L}_{BH} = \mathcal{L}_{LB}^2$. We use GMLS with $(k = 4, m = 6)$ and find the methods have $\sim 3^{rd}$-order asymptotic convergence.

	Manifold A		Manifold B		Manifold C			Manifold D	
h	**ℓ_2-error**	**Rate**	**ℓ_2-error**	**Rate**	**ℓ_2-error**	**Rate**	**h**	**ℓ_2-error**	**Rate**
0.1	3.7004e-03	-	1.0621e+01	-	6.1440e+01	-	.08	6.5445e-01	-
0.05	1.9863e-04	4.16	1.7987e-01	2.56	3.9161e-01	3.97	.04	1.6209e-02	5.42
0.025	1.1937e-05	4.03	1.9796e-02	3.18	2.9043e-02	3.76	.02	8.4581e-04	4.30
0.0125	7.3369e-07	4.01	1.6147e-03	3.61	2.0897e-03	3.80	.01	5.6742e-05	3.87

Table 7.4: Convergence of GMLS Approximation of the Curl-K-Curl Operator $\mathcal{L}_K$. We use GMLS with $(k_1 = 3, k_2 = 2, m = 6)$ and find the methods have $\sim 4^{rd}$-order asymptotic convergence.

involves estimation not only of the surface Gaussian Curvature K but also its first derivatives. For $\mathcal{L}_K$, we find $\sim$ 4th-order convergence rate, see Table 7.4.

7.2.1 Convergence of Curl Operators in GMLS

We also report tabulated results for the GMLS approximations of the operators $\mathcal{L}_{C0}$ and $\mathcal{L}_{C1}$ shown in Figure 7.2– 7.3.

	Manifold A		**Manifold B**		**Manifold C**			**Manifold D**	
h	ℓ_2**-error**	**Rate**	ℓ_2**-error**	**Rate**	ℓ_2**-error**	**Rate**	**h**	ℓ_2**-error**	**Rate**
0.1	2.7152e-05	-	1.5075e-03	-	4.8243e-01	-	.08	2.1570e-03	-
0.05	3.8309e-07	6.07	3.0281e-05	5.64	2.4465e-04	10.9	.04	2.2565e-05	6.68
0.025	5.8491e-09	6.00	6.9649e-07	5.43	6.1779e-06	5.31	.02	3.3550e-07	6.13
0.0125	8.8291e-11	6.04	1.3078e-08	5.72	1.1817e-07	5.71	.01	4.9708e-09	6.04

Table 7.5: Convergence of GMLS Approximation of the Surface Curl Operator on Scalars $\mathcal{L}_{C0}$. We use GMLS with $(k = 1, m = 6)$ and find the methods have $\sim 6^{th}$-order asymptotic convergence.

The Manifolds B and C have more complicated geometry and require more resolution to see behaviors in the asymptotic regime with a high-degree basis. We see that by lowering the degree of the basis these operators exhibit more readily behaviors in the asymptotic regime in Table 7.7 and 7.8.

Again, we emphasize while there is currently no rigorous convergence theory given the non-linear dependence on geometry in our GMLS approximations, we do find in each case agreement with the suggestive predictive rates $m + 1 - k$ similar to equation 6.1.9.

	Manifold A		Manifold B		Manifold C			Manifold D	
h	**ℓ_2-error**	**Rate**	**ℓ_2-error**	**Rate**	**ℓ_2-error**	**Rate**	**h**	**ℓ_2-error**	**Rate**
0.1	9.2312e-04	-	1.5887e-02	-	5.2497e+01	-	.08	1.9686e-02	-
0.05	1.4851e-05	5.88	1.2736e-03	3.64	1.3126e-02	8.65	.04	2.0410e-04	6.70
0.025	2.3374e-07	5.96	1.2597e-04	3.33	5.6087e-04	4.55	.02	3.0223e-06	6.13
0.0125	3.5970e-09	6.01	5.1267e-06	4.61	1.4082e-05	5.32	.01	4.3847e-08	6.07

Table 7.6: Convergence of GMLS Approximation of the Surface Curl Operator on Vectors $\mathcal{L}_{C1}$. We use GMLS with $(k_1 = 2, k_2 = 1, m = 6)$ and find the methods have $\sim 5^{th}$-order asymptotic convergence or greater. It is notable that in the case of Manifold A and D we in fact see $\sim 6^{th}$-order convergence. This manifests since the manifolds have a relatively symmetric geometry compared to Manifold B and C, see Figure 6.3. This results in a simplification with fewer non-zero terms and derivatives associated with the contributions of the geometry to the operator. As a consequence, the GMLS approximation at a given order m becomes more accurate by one order for Manifold A and D.

	Manifold B		Manifold C	
h	**ℓ_2-error**	**Rate**	**ℓ_2-error**	**Rate**
0.1	5.2558e-03	-	1.2083e-02	-
0.05	3.6359e-04	3.85	1.0345e-03	3.54
0.025	2.3078e-05	3.97	7.3790e-05	3.81
0.0125	1.4569e-06	3.98	4.8316e-06	3.93

Table 7.7: Convergence of GMLS Approximation of the Surface Curl on Scalars $\mathcal{L}_{C0}$. We use GMLS with $(k = 1, m = 4)$ and find the methods have $\sim 4^{th}$-order asymptotic convergence.

7.3 Convergence of GMLS Stokes Solvers on Spherical Topologies

We investigate the convergence of our GMLS methods for the surface hydrodynamic equations formulated in Section 7.1. We study convergence of our solvers for hydrodynamic flows by developing manufactured solutions using high precision symbolic calculations of the incompressible flow field $\mathbf{v}^\flat = -\star\mathbf{d}\Phi = \mathcal{C}_0\Phi$ with the specific choice of Φ given in Section 7.2.

We calculate symbolically the expressions of the forcing term $\mathbf{b}$ using equation 2.5.3 where $\mu_m(-\boldsymbol{\delta}\mathbf{d} + 2K)\mathbf{v}^\flat - \gamma\mathbf{v}^\flat - \mathbf{d}p = -\mathbf{b}^\flat$. We manufacture the data $\mathbf{b}$ needed on the RHS of equation 2.5.3 using

$$\mathbf{b}^\flat = \mu_m\boldsymbol{\delta}\mathbf{d}\mathbf{v}^\flat + (\gamma - 2\mu_m K)\mathbf{v}^\flat. \tag{7.3.1}$$

Since generating both the velocity field $\mathbf{v}$ and force density $\mathbf{b}$ this way will already be incompressible, we have used that we can set $p = 0$ when manufacturing our

	Manifold B		**Manifold C**	
h	ℓ_2**-error**	**Rate**	ℓ_2**-error**	**Rate**
0.1	6.3586e-01	-	7.6579e-01	-
0.05	1.6568e-01	1.94	2.1680e-01	1.82
0.025	4.1633e-02	1.99	5.6498e-02	1.94
0.0125	1.0399e-02	1.99	1.4336e-02	1.98

Table 7.8: Convergence of GMLS Approximation of the Surface Curl on Vectors $\mathcal{L}_{C1}$. We use GMLS with $(k = 1, m = 2)$ and find the methods have $\sim 2^{nd}$-order asymptotic convergence.

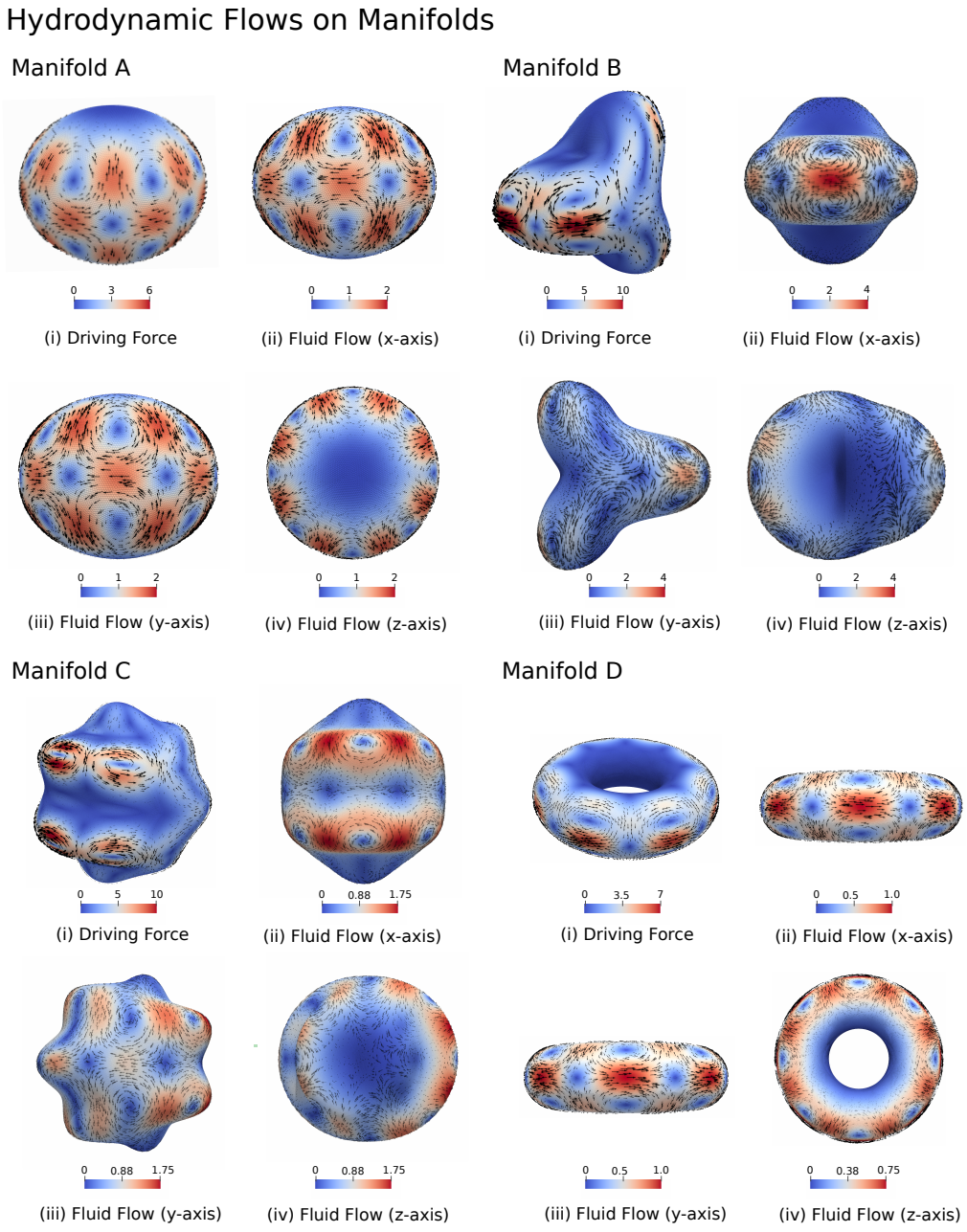

Figure 7.4: Surface Hydrodynamic Flows on Manifolds A–D. For a given force density, shown in (i), we use our GMLS solver to compute numerically the surface hydrodynamic flow responses, shown in (ii)–(iv), on each of the manifolds, defined in Section 6.4.1. Manifold $A-D$ solutions were computed at a resolution with number of sample points $n_A = 38,486, n_B = 147,634, n_C = 127,346$, and $n_D = 118,942$ [9].

data. In practice, we evaluate equation 7.3.1 to high precision using the symbolic package SymPy [144].

We investigate the convergence of the GMLS solvers using the ℓ^2-error

$$\epsilon_{hydro} = \|\tilde{\mathbf{v}} - \mathbf{v}\|_2 / \|\mathbf{v}\|_2 \tag{7.3.2}$$

$$\tilde{\mathbf{v}} = \mathcal{C}_0(\mathcal{S}^{-1}(\mathcal{C}_0\mathbf{b})). \tag{7.3.3}$$

The $\mathbf{v}$ denotes the exact solution, $\mathcal{C}_0$ approximates numerically $-\star\,\mathbf{d}_0$, $\mathcal{C}_1$ approximates numerically $-\star\,\mathbf{d}_1$, and $\mathcal{S}^{-1}$ denotes the numerical solution operator corresponding to use of our GMLS solver. We use the hydrodynamics equations both formulated using the biharmonic form in equation 7.1.1 or in the split form in equation 7.1.2.

For each of the manifolds $A - D$, we computed manufactured solutions with the parameters $\mu_m = 0.1$, $\gamma = 0.1$ in equation 7.3.1. We used the surface force density $\mathbf{b}$ to numerically compute surface hydrodynamic flow responses $\tilde{\mathbf{v}}$ using our GMLS solvers discussed at the begining of the Chapter. We show the hydrodynamic surface flows in Figure 7.4. We show our convergence results for both the case of the biharmonic formulation and split formulation in Figure 7.5. We give tabulated results for each of these convergence studies in Tables 7.9– 7.16.

We emphasize that these convergence studies take into account the full pipeline of our GMLS numerical methods as shown in Figure 7.1. This involves not only the solution of biharmonic or split equations, but also the GMLS reconstruction of the surface velocity field $\mathbf{v}$ from the computed vector-potential Φ and the cal-

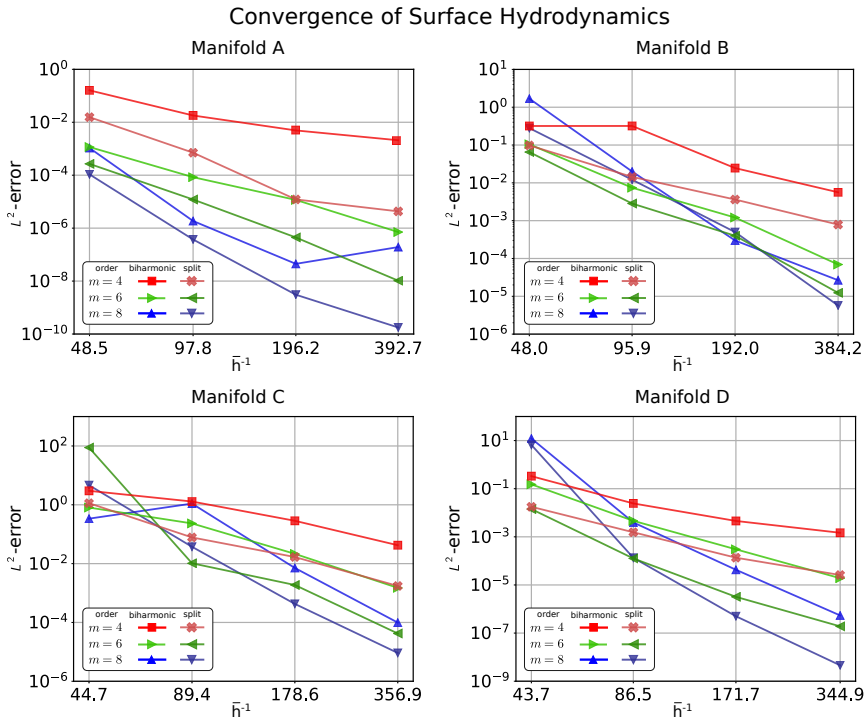

Figure 7.5: Convergence of GMLS Solvers for the Hydrodynamic Velocity Field. We use the GMLS methods with $m_1 = m_2 = m$ polynomial orders for approximating the surface geometry and surface velocity field $\mathbf{v}$. We study convergence for the GMLS solver when using the biharmonic formulation in equation 7.1.1 verses when using the split formulation in equation 7.1.2 [9].

	m = 4		**m = 6**		**m = 8**	
h	ℓ_2**-error**	**Rate**	ℓ_2**-error**	**Rate**	ℓ_2**-error**	**Rate**
0.1	1.6072e-01	-	1.1597e-03	-	1.0648e-03	-
0.05	1.8027e-02	3.11	8.4190e-05	3.73	1.8627e-06	9.04
0.025	4.9155e-03	1.86	1.1655e-05	2.84	4.4796e-08	5.35
0.0125	2.0873e-03	1.23	7.1161e-07	4.02	1.9263e-07	-2.10

Table 7.9: Convergence on Manifold A of our GMLS solver based on the biharmonic formulation of the hydrodynamics in equation 7.1.1. The target sampling distance h is discussed Section 7.0.1.

	m = 4		**m = 6**		**m = 8**	
h	ℓ_2**-error**	**Rate**	ℓ_2**-error**	**Rate**	ℓ_2**-error**	**Rate**
0.1	1.5578e-02	-	2.6826e-04	-	1.0756e-04	-
0.05	7.0783e-04	4.40	1.2065e-05	4.41	3.7309e-07	8.06
0.025	1.2151e-05	5.83	4.4532e-07	4.74	3.0556e-09	6.90
0.0125	4.3056e-06	1.49	1.0349e-08	5.42	1.7664e-10	4.10

Table 7.10: Convergence on Manifold A of our GMLS solver based on the split formulation of the hydrodynamics in equation 7.1.2.

culation of the vector-potentials $\Psi = - \star \mathbf{db}$ for the body force density $\mathbf{b}$ which drives the flow. These steps also each have a non-linear dependence on the geometry which contributes through our GMLS reconstructions from the point set sampling of the manifold.

In the convergence studies, we find in all cases that the GMLS solvers are able to resolve the surface hydrodynamic fields to a high level of precision. The Manifolds B and C presented the most challenges for the solvers with largest prefactors in their convergence. This is expected given the increased amount of resolution required to resolve the geometric contributions to the differential operators in the hydrodynamic equations 7.1.1– 7.1.2. In all cases, we found our GMLS solvers

	m = 4		**m = 6**		**m = 8**	
h	**ℓ_2-error**	**Rate**	**ℓ_2-error**	**Rate**	**ℓ_2-error**	**Rate**
0.1	3.1890e-01	-	1.0457e-01	-	1.6845e+00	-
0.05	3.1951e-01	-0.002	7.4388e-03	3.81	1.9954e-02	6.40
0.025	2.4571e-02	3.69	1.2081e-03	2.62	2.9917e-04	6.05
0.0125	5.6309e-03	2.12	6.9269e-05	4.11	2.6601e-05	3.48

Table 7.11: Convergence on Manifold B of our GMLS solver based on the biharmonic formulation of the hydrodynamics in equation 7.1.1.

	m = 4		**m = 6**		**m = 8**	
h	**ℓ_2-error**	**Rate**	**ℓ_2-error**	**Rate**	**ℓ_2-error**	**Rate**
0.1	9.7895e-02	-	6.5222e-02	-	2.8024e-01	-
0.05	1.4383e-02	2.77	2.8402e-03	4.52	1.2100e-02	4.53
0.025	3.6243e-03	1.98	3.9929e-04	2.82	4.9907e-04	4.59
0.0125	7.8747e-04	2.20	1.2357e-05	5.00	5.7023e-06	6.44

Table 7.12: Convergence on Manifold B of our GMLS solver based on the split formulation of the hydrodynamics in equation 7.1.2.

based on the split formulation performed better when using equation 7.1.2 relative to our GMLS solvers based on the biharmonic formulation of equation 7.1.1. Interestingly, for Manifold B and C these differences for $m = 8$ where not as pronounced, see Figure 7.5. We think this is a manifestation of the challenges in capturing the geometric contributions to the differential operator that with limited resolution will not benefit as much from the higher order approximations or split formulations relative to the case of less complicated geometries.

We find in the case of Manifold A that the GMLS solver for sufficiently large order ($m \geq 6$) converges at a rate of approximately $\sim 4^{th}$-order for the biharmonic formulation and at a rate of approximately $\sim 5^{th}$-order for the split formulation.

	m = 4		**m = 6**		**m = 8**	
h	ℓ_2**-error**	**Rate**	ℓ_2**-error**	**Rate**	ℓ_2**-error**	**Rate**
0.1	2.9886e+00	-	8.0650e-01	-	3.3799e-01	-
0.05	1.2926e+00	1.21	2.3277e-01	1.79	1.0993e+00	-1.70
0.025	2.8576e-01	2.18	2.1497e-02	3.44	7.1166e-03	7.28
0.0125	4.2226e-02	2.76	1.4986e-03	3.84	9.8921e-05	6.17

Table 7.13: Convergence on Manifold C of our GMLS solver based on the biharmonic formulation of the hydrodynamics in equation 7.1.1.

	m = 4		**m = 6**		**m = 8**	
h	ℓ_2**-error**	**Rate**	ℓ_2**-error**	**Rate**	ℓ_2**-error**	**Rate**
0.1	1.1346e+00	-	8.8130e+01	-	4.6473e+00	-
0.05	7.7801e-02	3.86	1.0276e-02	13.0	3.7375e-02	6.96
0.025	1.6751e-02	2.22	1.8764e-03	2.45	4.2722e-04	6.46
0.0125	1.7381e-03	3.27	4.2181e-05	5.48	9.1845e-06	5.54

Table 7.14: Convergence on Manifold C of our GMLS solver based on the split formulation of the hydrodynamics in equation 7.1.2.

We base these conclusions on the overall trends, and some of this is a little obscured by the noise of the convergence after acheiving a high level of accuracy. We suspect the last up tick of the error observed for $m = 8$ for the biharmonic formulation is likely a consequence of the conditioning of the linear system becoming a limiting factor. We note the overall high level of precision already achieved by that data point with errors on the order of 10^{-8}, see Figure 7.5 and Table 7.9. We find there is a particular advantage of our GMLS solvers when based on the split formulation. Our GMLS methods in this case are able to converge to much higher levels of precision achieving errors on the order 10^{-10} in the case of $m = 8$ at the largest resolutions considered, see Table 7.9.

	m = 4		**m = 6**		**m = 8**	
h	**ℓ_2-error**	**Rate**	**ℓ_2-error**	**Rate**	**ℓ_2-error**	**Rate**
0.08	3.3170e-01	-	1.5154e-01	-	1.2223e+01	-
0.04	2.4421e-02	3.82	4.6233e-03	5.11	3.9632e-03	11.7
0.02	4.5705e-03	2.44	3.0246e-04	3.97	4.2784e-05	6.60
0.01	1.4748e-03	1.62	1.9067e-05	3.96	5.4137e-07	6.26

Table 7.15: Convergence on Manifold D of our GMLS solver based on the biharmonic formulation of the hydrodynamics in equation 7.1.1.

	m = 4		**m = 6**		**m = 8**	
h	**ℓ_2-error**	**Rate**	**ℓ_2-error**	**Rate**	**ℓ_2-error**	**Rate**
0.08	1.7719e-02	-	1.4221e-02	-	6.6061e+00	-
0.04	1.5473e-03	3.57	1.2632e-04	6.92	1.3431e-04	15.8
0.02	1.3575e-04	3.54	3.2125e-06	5.35	5.0041e-07	8.15
0.01	2.5891e-05	2.37	1.9018e-07	4.05	4.5906e-09	6.72

Table 7.16: Convergence on Manifold D of our GMLS solver based on the split formulation of the hydrodynamics in equation 7.1.2.

Our results show that both formulations of the GMLS solvers are able to achieve high order convergence rates in approximating the hydrodynamic fields. We emphasize that these results assess contributions from the entire pipe-line that includes not only the GMLS solve but also the pre-processing and post-processing steps involving the curl operators that arise in our vector-potential formulation for incompressible hydrodynamic flows. We expect that many of our GMLS methods can be extended to obtain other high order solvers for the solution of related scalar-valued and vector-valued partial differential equations on surfaces. Additional discussion and details can also be found in [9].

Chapter 8

Conclusion

We developed meshfree solvers for manifolds for investigating hydrodynamic flows on curved surfaces. We formulated GMLS methods both for adaptive handling of the geometry on-the-fly of the manifold and for solving general scalar-valued and vector-valued PDEs on surfaces. We demonstrated our approaches for hydrodynamic flows on curved surfaces in the Stokesian regime. We studied how our solvers perform in each of these different settings by performing convergence studies for manifolds having non-trivial geometries of spherical topology. We found our GMLS solver were able to achieve high-order convergence rates on these geometries.

We expect our solvers to be useful for applications involving hydrodynamic transport and coupling on curved fluid interfaces. We are currently working on extending our GMLS solver to general smooth compact topologies. Additionally we plan to use this framework to develop fluctuating hydrodynamics simulations

on these surfaces, and to leverage the full parallel computing power of the Compadre toolkit. Additional discussions and details can also be found in [9].

Bibliography

[1] V.I. Lebedev. Quadratures on a sphere. *USSR Computational Mathematics and Mathematical Physics*, 16(2):10–24, 1976.

[2] V. I. Lebedev and D. N. Laikov. A quadrature formula for the sphere of the 131st algebraic order of accuracy. *Dokl. Math.*, 59:477–481, 1999.

[3] Micheal Spivak. *A Comprehensive Introduction to Differential Geometry*, volume 1. Publish or Perish Inc., 1999.

[4] A. Pressley. *Elementary Differential Geometry*. Springer, 2001.

[5] B. Gross and P. J. Atzberger. Spectral numerical exterior calculus methods for differential equations on radial manifolds. *Journal of Scientific Computing*, Dec 2017.

[6] Jon Karl Sigurdsson and Paul J. Atzberger. Hydrodynamic coupling of particle inclusions embedded in curved lipid bilayer membranes. *Soft Matter*, 12(32):6685–6707, 2016.

[7] Brian Cabral and Leith Casey Leedom. Imaging vector fields using line integral convolution. In *Proceedings of the 20th Annual Conference on Computer Graphics and Interactive Techniques*, SIGGRAPH '93, pages 263–270, New York, NY, USA, 1993. ACM.

[8] B.J. Gross and P.J. Atzberger. Hydrodynamic flows on curved surfaces: Spectral numerical methods for radial manifold shapes. *Journal of Computational Physics*, 371:663 – 689, 2018.

[9] B. J. Gross, N. Trask, P. Kuberry, and P. J. Atzberger. Meshfree methods on manifolds for hydrodynamic flows on curved surfaces: A generalized moving least-squares (gmls) approach, 2019.

[10] H. Kellay. Hydrodynamics experiments with soap films and soap bubbles: A short review of recent experiments. *Physics of Fluids*, 29(11):111113, 2017.

[11] U Kornek, F Mauller, K Harth, A Hahn, S Ganesan, L Tobiska, and R Stannarius. Oscillations of soap bubbles. *New Journal of Physics*, 12(7):073031, 2010.

[12] Z. C. Feng and L. G. Leal. Nonlinear bubble dynamics. *Annual Review of Fluid Mechanics*, 29(1):201–243, 1997.

[13] S. Kim and S.J. Karrila. *Microhydrodynamics: Principles and Selected Applications*. Butterworth-Heinemann, 1991.

[14] Aurelia R. Honerkamp-Smith, Francis G. Woodhouse, Vasily Kantsler, and Raymond E. Goldstein. Membrane viscosity determined from shear-driven flow in giant vesicles. *Phys. Rev. Lett.*, 111(3):038103–, July 2013.

[15] Francois Quemeneur, Jon K. Sigurdsson, Marianne Renner, Paul J. Atzberger, Patricia Bassereau, and David Lacoste. Shape matters in protein mobility within membranes. *Proceedings of the National Academy of Sciences*, 111(14):5083–5087, 2014.

[16] P. G. Saffman and M. Delbruck. Brownian-motion in biological-membranes. *Proceedings of the National Academy of Sciences of the United States of America*, 72(8):3111–3113–, 1975.

[17] Thomas R. Powers, Greg Huber, and Raymond E. Goldstein. Fluid-membrane tethers: Minimal surfaces and elastic boundary layers. *Phys. Rev. E*, 65(4):041901–, March 2002.

[18] Marcello Cavallaro, Lorenzo Botto, Eric P Lewandowski, Marisa Wang, and Kathleen J Stebe. Curvature-driven capillary migration and assembly of rod-like particles. *Proceedings of the National Academy of Sciences of the United States of America*, 108(52):20923–20928, December 2011.

[19] S.Q. Choi, S. Steltenkamp, J.A. Zasadzinski, and T.M. Squires. Active microrheology and simultaneous visualization of sheared phospholipid monolayers. *Nat Commun*, 2:312–, May 2011.

[20] Dmitry Ershov, Joris Sprakel, Jeroen Appel, Martien A. Cohen Stuart, and Jasper van der Gucht. Capillarity-induced ordering of spherical colloids on an interface with anisotropic curvature. *Proceedings of the National Academy of Sciences*, 110(23):9220–9224, 2013.

[21] F Bresme and M Oettel. Nanoparticles at fluid interfaces. *Journal of Physics: Condensed Matter*, 19(41):413101, 2007.

[22] S. Panzuela Q. Xiao R. Delgado-Buscalioni A. Donev R. P. Peláez, F. Balboa Usabiaga. Hydrodynamic fluctuations in quasi-two dimensional diffusion. *arXiv*, 2018.

[23] R. J. Braun, R. Usha, G. B. McFadden, T. A. Driscoll, L. P. Cook, and P. E. King-Smith. Thin film dynamics on a prolate spheroid with application to the cornea. *Journal of Engineering Mathematics*, 73(1):121–138, Apr 2012.

[24] Eline Hermans, M. Saad Bhamla, Peter Kao, Gerald G. Fuller, and Jan Vermant. Lung surfactants and different contributions to thin film stability. *Soft Matter*, 11:8048–8057, 2015.

[25] Harishankar Manikantan and Todd M. Squires. Pressure-dependent surface viscosity and its surprising consequences in interfacial lubrication flows. *Phys. Rev. Fluids*, 2:023301, Feb 2017.

[26] Alex Mogilner and Angelika Manhart. Intracellular fluid mechanics: Coupling cytoplasmic flow with active cytoskeletal gel. *Annual Review of Fluid Mechanics*, 50(1):347–370, 2018.

[27] Sarah A Nowak and Tom Chou. Models of dynamic extraction of lipid tethers from cell membranes. *Physical Biology*, 7(2):026002, 2010.

[28] J.E. Marsden and T.J.R. Hughes. *Mathematical Foundations of Elasticity*. Dover, 1994.

[29] James Eells. Geometric aspects of currents and distributions. *Proceedings of the National Academy of Sciences*, 41(7):493–496, 1955.

[30] Hassler Whitney. *Geometric Integration Theory*. Princeton University Press, 1957.

[31] Eva Kanso, Marino Arroyo, Yiying Tong, Arash Yavari, Jerrold G. Marsden, and Mathieu Desbrun. On the geometric character of stress in continuum mechanics. *Zeitschrift für angewandte Mathematik und Physik*, 58(5):843–856, 2007.

[32] C. Pozrikidis. Interfacial dynamics for stokes flow. *Journal of Computational Physics*, 169(2):250 – 301, 2001.

[33] Thomas R. Powers. Dynamics of filaments and membranes in a viscous fluid. *Rev. Mod. Phys.*, 82:1607–1631, May 2010.

[34] P. A. Kralchevsky, J. C. Eriksson, and S. Ljunggren. Theory of curved interfaces and membranes: Mechanical and thermodynamical approaches. *Advances in Colloid and Interface Science*, 48:19–59, April 1994.

[35] L.E. Scriven. Dynamics of a fluid interface equation of motion for newtonian surface fluids. *Chemical Engineering Science*, 12(2):98–108, 1960.

[36] Francis G. Woodhouse and Raymond E. Goldstein. Shear-driven circulation patterns in lipid membrane vesicles. *Journal of Fluid Mechanics*, 705:165–175, 2012.

[37] Wei zang Chien. *The intrinsic theory of elastic shells and plates.* PhD thesis, University of Toronto, 1942.

[38] J. L. Ericksen and C. Truesdell. Exact theory of stress and strain in rods and shells. *Archive for Rational Mechanics and Analysis*, 1(1):295–323, Jan 1957.

[39] D. A. Edwards and D. T. Wasan. Surface rheology ii. the curved fluid surface. *Journal of Rheology*, 32(5):447–472, 1988.

[40] Gretchen M. Mavrovouniotis and Howard Brenner. A micromechanical investigation of interfacial transport processes. i. interfacial conservation equations. *Philosophical Transactions of the Royal Society of London A: Mathematical, Physical and Engineering Sciences*, 345(1675):165–207, 1993.

[41] Gretchen M. Mavrovouniotis, Howard Brenner, David A. Edwards, and Li Ting. A micromechanical investigation of interfacial transport processes. ii. interfacial constitutive equations. *Philosophical Transactions of the Royal Society of London A: Mathematical, Physical and Engineering Sciences*, 345(1675):209–228, 1993.

[42] T. W. Secomb and R. Skalak. Surface flow of viscoelastic membranes in viscous fluids. *Quarterly Journal of Mechanics and Applied Mathematics*, 35(pt 2):233–247, 5 1982.

[43] Mohammad Rahimi, Antonio DeSimone, and Marino Arroyo. Curved fluid membranes behave laterally as effective viscoelastic media. *Soft Matter*, 9:11033–11045, 2013.

[44] D. J. Steigmann. Fluid films with curvature elasticity. *Archive for Rational Mechanics and Analysis*, 150(2):127–152, Dec 1999.

[45] W. Cai and T. C. Lubensky. Hydrodynamics and dynamic fluctuations of fluid membranes. *Phys. Rev. E*, 52:4251–4266, 1995.

[46] M. L. Henle, R. McGorty, A. B. Schofield, A. D. Dinsmore, and A. J. Levine. The effect of curvature and topology on membrane hydrodynamics. *EPL (Europhysics Letters)*, 84(4):48001–, 2008.

[47] Petia M. Vlahovska and Ruben Serral Gracia. Dynamics of a viscous vesicle in linear flows. *Phys. Rev. E*, 75(1):016313–, January 2007.

[48] Padmini Rangamani, Ashutosh Agrawal, Kranthi K. Mandadapu, George Oster, and David J. Steigmann. Interaction between surface shape and intra-surface viscous flow on lipid membranes. *Biomechanics and Modeling in Mechanobiology*, 12(4):833–845, Aug 2013.

[49] Markus Deserno. Fluid lipid membranes: From differential geometry to curvature stresses. *Membrane mechanochemistry: From the molecular to the cellular scale*, 185:11–45, January 2015.

[50] Amaresh Sahu, Roger A. Sauer, and Kranthi K. Mandadapu. Irreversible thermodynamics of curved lipid membranes. *Phys. Rev. E*, 96:042409, Oct 2017.

[51] Arash Yavari, Jerrold E. Marsden, and Michael Ortiz. On spatial and material covariant balance laws in elasticity. *Journal of Mathematical Physics*, 47(4):042903, 2006.

[52] Jemal Guven and Pablo Vázquez-Montejo. *The Geometry of Fluid Membranes: Variational Principles, Symmetries and Conservation Laws*, chapter 4, pages 167–219. Springer International Publishing, Cham, 2018.

[53] Marino Arroyo and Antonio DeSimone. Relaxation dynamics of fluid membranes. *Phys. Rev. E*, 79(3):031915–, March 2009.

[54] John B. Greer, Andrea L. Bertozzi, and Guillermo Sapiro. Fourth order partial differential equations on general geometries. *J. Comput. Phys.*, 216(1):216–246, July 2006.

[55] Sharif Elcott, Yiying Tong, Eva Kanso, Peter Schröder, and Mathieu Desbrun. Stable, circulation-preserving, simplicial fluids. *ACM Trans. Graph.*, 26(1), January 2007.

[56] Mathieu Desbrun Peter Schroder Fernando de Goes, Keenan Crane. Digital geometry processing with discrete exterior calculus. In *SIGGRAPH*, 2013.

[57] Robert I. Saye and James A. Sethian. Multiscale modeling of membrane rearrangement, drainage, and rupture in evolving foams. *Science*, 340(6133):720–724, 2013.

[58] Anil N. Hirani. *Discrete Exterior Calculus.* PhD thesis, Caltech, 2003.

[59] Mathieu Desbrun Peter Schroder Fernando de Goes, Keenan Crane. Digital geometry processing with discrete exterior calculus. In *SIGGRAPH*, 2013.

[60] Richard S. Falk Douglas N. Arnold and Ragnar Winther. Finite element exterior calculus: from hodge theory to numerical stability. *Bull. Amer. Math. Soc.*, 2010.

[61] Michael Holst Andrew Gillette and Yunrong Zhu. Finite element exterior calculus for evolution problems. *Journal of Computational Mathematics*, 2017.

[62] M. Desbrun, A. N. Hirani, and J. E. Marsden. Discrete exterior calculus for variational problems in computer vision and graphics. In *42nd IEEE International Conference on Decision and Control (IEEE Cat. No.03CH37475)*, volume 5, pages 4902–4907 Vol.5, 2003.

[63] Omri Azencot, Orestis Vantzos, Max Wardetzky, Martin Rumpf, and Mirela Ben-Chen. Functional thin films on surfaces. In *Proceedings of the 14th ACM SIGGRAPH / Eurographics Symposium on Computer Animation*, SCA '15, pages 137–146, New York, NY, USA, 2015. ACM.

[64] Ari Stern, Yiying Tong, Mathieu Desbrun, and Jerrold E. Marsden. Geometric computational electrodynamics with variational integrators and discrete differential forms. In Dong Eui Chang, Darryl D. Holm, George Patrick, and Tudor Ratiu, editors, *Geometry, Mechanics, and Dynamics: The Legacy of Jerry Marsden*, pages 437–475. Springer New York, New York, NY, 2015.

[65] Martin Michael Muller, Markus Deserno, and J. Guven. Interface-mediated interactions between particles: A geometrical approach. *Phys. Rev. E*, 72(6):061407–, December 2005.

[66] Roger A. Sauer, Thang X. Duong, Kranthi K. Mandadapu, and David J. Steigmann. A stabilized finite element formulation for liquid shells and its application to lipid bilayers. *Journal of Computational Physics*, 330:436 – 466, 2017.

[67] Arash Yavari. On geometric discretization of elasticity. *Journal of Mathematical Physics*, 49(2):022901, 2008.

[68] C. Lin and M.J. Perry. Shape description using surface triangulation. *In Proceedings, IEEE Workshop on Computer Vision: Representation and Control*, pages 38–43, 1982.

[69] Alan M. McIvor and Robert J. Valkenburg. A comparison of local surface geometry estimation methods. *Machine Vision and Applications*, 10(1):17–26, May 1997.

[70] E. M. Stokely and S. Y. Wu. Surface parametrization and curvature measurement of arbitrary 3-d objects: five practical methods. *IEEE Transactions on Pattern Analysis and Machine Intelligence*, 14(8):833–840, 1992.

[71] G. Taubin. Estimating the tensor of curvature of a surface from a polyhedral approximation. In *Proceedings of IEEE International Conference on Computer Vision*, pages 902–907, 1995.

[72] MELVIN LEOK MATHIEU DESBRUN, ANIL N. HIRANI and JERROLD E. MARSDEN. Discrete exterior calculus. *Technical Report*, 2003.

[73] D. Zorin. Curvature-based energy for simulation and variational modeling. In *International Conference on Shape Modeling and Applications 2005 (SMI' 05)*, pages 196–204, 2005.

[74] Chen-Hung Wu, Thomas G. Fai, Paul J. Atzberger, and Charles S. Peskin. Simulation of osmotic swelling by the stochastic immersed boundary method. *SIAM Journal on Scientific Computing*, 37(4):B660–B688, 2015.

[75] Kenneth A. Brakke. The surface evolver. *Experiment. Math.*, 1(2):141–165, 1992.

[76] Sharif Elcott and Peter Schröder. Building your own dec at home. In *ACM SIGGRAPH 2005 Courses*, SIGGRAPH '05, New York, NY, USA, 2005. ACM.

[77] Douglas N. Arnold, Richard S. Falk, and Ragnar Winther. Finite element exterior calculus, homological techniques, and applications. 15:1–155–, 2006.

[78] Y. Zhu A. Gilette, M. Holst. Finite element exterior calculus for evolution problems. *Journal of Computational Mathematics*, 2017.

[79] Pavel B. Bochev and James M. Hyman. Principles of mimetic discretizations of differential operators. In Douglas N. Arnold, Pavel B. Bochev, Richard B. Lehoucq, Roy A. Nicolaides, and Mikhail Shashkov, editors,

Compatible Spatial Discretizations, pages 89–119, New York, NY, 2006. Springer New York.

[80] R. Abraham, J.E. Marsden, and T.S. Ratiu. *Manifolds, Tensor Analysis, and Applications*. Number v. 75. Springer New York, 1988.

[81] Jurgen Jost. *Riemannian Geometry and Geometric Analysis*. Springer, 1991.

[82] Mamdouh S. Mohamed, Anil N. Hirani, and Ravi Samtaney. Discrete exterior calculus discretization of incompressible navier-stokes equations over surface simplicial meshes. *Journal of Computational Physics*, 312:175 – 191, 2016.

[83] Dzhelil Rufat, Gemma Mason, Patrick Mullen, and Mathieu Desbrun. The chain collocation method: A spectrally accurate calculus of forms. *Journal of Computational Physics*, 257, Part B:1352–1372, January 2014.

[84] Martin D Buhmann. *Radial basis functions: theory and implementations*, volume 12. Cambridge university press, 2003.

[85] Robert A Gingold and Joseph J Monaghan. Smoothed particle hydrodynamics: theory and application to non-spherical stars. *Monthly notices of the royal astronomical society*, 181(3):375–389, 1977.

[86] Peter Lancaster and Kes Salkauskas. Surfaces generated by moving least squares methods. *Mathematics of computation*, 37(155):141–158, 1981.

[87] Shingyu Leung, John Lowengrub, and Hongkai Zhao. A grid based particle method for solving partial differential equations on evolving surfaces and modeling high order geometrical motion. *Journal of Computational Physics*, 230(7):2540 – 2561, 2011.

[88] Jian Liang and Hongkai Zhao. Solving partial differential equations on point clouds. *SIAM Journal on Scientific Computing*, 35(3):A1461–A1486, 2013.

[89] Joerg Kuhnert Pratik Suchde. A fully lagrangian meshfree framework for pdes on evolving surfaces. *arXiv*, 2019.

[90] Colin B. Macdonald, Barry Merriman, and Steven J. Ruuth. Simple computation of reaction-diffusion processes on point clouds. *Proceedings of the National Academy of Sciences of the United States of America*, 110:9209–14, Jun 2013.

[91] Marino Arroyo Alejandro Torres-Sánchez, Daniel Santos-Oliván. Approximation of tensor fields on surfaces of arbitrary topology based on local monge parametrizations. *arXiv*, 2019.

[92] Natasha Flyer and Grady B Wright. Transport schemes on a sphere using radial basis functions. *Journal of Computational Physics*, 226(1):1059–1084, 2007.

[93] Natasha Flyer, Erik Lehto, Sébastien Blaise, Grady B Wright, and Amik St-Cyr. A guide to rbf-generated finite differences for nonlinear transport: Shallow water simulations on a sphere. *Journal of Computational Physics*, 231(11):4078–4095, 2012.

[94] Natasha Flyer and Grady B Wright. A radial basis function method for the shallow water equations on a sphere. *Proceedings of the Royal Society A: Mathematical, Physical and Engineering Sciences*, 465(2106):1949–1976, 2009.

[95] Bengt Fornberg and Erik Lehto. Stabilization of rbf-generated finite difference methods for convective pdes. *Journal of Computational Physics*, 230(6):2270–2285, 2011.

[96] Thomas-Peter Fries and Ted Belytschko. Convergence and stabilization of stress-point integration in mesh-free and particle methods. *International Journal for Numerical Methods in Engineering*, 74(7):1067–1087, 2008.

[97] Nathaniel Trask, Martin Maxey, Kyungjoo Kim, Mauro Perego, Michael L Parks, Kai Yang, and Jinchao Xu. A scalable consistent second-order sph

solver for unsteady low reynolds number flows. *Computer Methods in Applied Mechanics and Engineering*, 289:155–178, 2015.

[98] Holger Wendland. *Scattered data approximation*, volume 17. Cambridge university press, 2004.

[99] Robert Schaback. Error analysis of nodal meshless methods. *arXiv preprint arXiv:1612.07550*, 2016.

[100] Andriy Sokolov, Oleg Davydov, and Stefan Turek. Numerical study of the rbf-fd level set based method for partial differential equations on evolving-in-time surfaces. Technical report, Technical report, Fakultät für Mathematik, TU Dortmund, 2017.

[101] Pratik Suchde and Joerg Kuhnert. A meshfree generalized finite difference method for surface pdes. *arXiv preprint arXiv:1806.07193*, 2018.

[102] D. Mirzaei, R. Schaback, and M. Dehghan. On generalized moving least squares and diffuse derivatives. *IMA Journal of Numerical Analysis*, 32(3):983–1000, July 2012.

[103] E.H. Lieb and M. Loss. *Analysis*. American Mathematical Society, 2001.

[104] J.-D. Debus, M. Mendoza, S. Succi, and H. J. Herrmann. Energy dissipation in flows through curved spaces. *Scientific Reports*, 7:42350, February 2017.

[105] Donald Shepard. A two-dimensional interpolation function for irregularly-spaced data. In *Proceedings of the 1968 23rd ACM National Conference*, ACM '68, pages 517–524, New York, NY, USA, 1968. ACM.

[106] P. Lancaster and K. Salkauskas. Surfaces generated by moving least squares methods. *Math. Comp.*, 37:141–158, 1981.

[107] Hugues Hoppe, Tony DeRose, Tom Duchamp, John McDonald, and Werner Stuetzle. Surface reconstruction from unorganized points. *SIGGRAPH Comput. Graph.*, 26(2):71–78, July 1992.

[108] Nina Amenta and Yong Joo Kil. Defining point-set surfaces. In *ACM SIGGRAPH 2004 Papers*, SIGGRAPH '04, pages 264–270, New York, NY, USA, 2004. ACM.

[109] Paul Kuberry, Peter Bosler, and Nathaniel Trask. Compadre toolkit, February 2019.

[110] Whitney H. *Differentiable manifolds*, volume 37. Ann. of Math., 1936.

[111] Michael Spivak. *Calculus On Manifolds: A Modern Approach To Classical Theorems Of Advanced Calculus*. Westview Press, 1971.

[112] A.E. Green and R.S. Rivlin. On cauchy's equations of motion. *ZAMP*, 15:290–293, 1964.

[113] L.D. Landau, , and E.M. Lifshitz. Mechanics (third edition). In L.D. LANDAU, , and E.M. LIFSHITZ, editors, *Mechanics (Third Edition)*, pages iv –. Butterworth-Heinemann, Oxford, third edition edition, 1976.

[114] J. D. Steigmann. Fluid films with curvature elasticity. *Archive for Rational Mechanics and Analysis*, 150(2):127–152, 1999.

[115] K Seki, S Komura, and M Imai. Concentration fluctuations in binary fluid membranes. *Journal of Physics: Condensed Matter*, 19(7):072101, 2007.

[116] D. J. Acheson. *Elementary Fluid Dynamics*. Oxford Applied Mathematics and Computing Science Series, 1990.

[117] G. K. Batchelor. *An Introduction to Fluid Dynamics*. Cambridge Mathematical Library. Cambridge University Press, 2000.

[118] P. G. Saffman. Brownian motion in thin sheets of viscous fluid. *J. Fluid Mech.*, 73:593–602, 1976.

[119] H. Lamb. *Hydrodynamics*. University Press, 1895.

[120] A. J. Levine and F. C. MacKintosh. Dynamics of viscoelastic membranes. *Phys. Rev. E*, 66:061606, 2002.

[121] Yuri Bazilevs J. Austin Cottrell, Thomas J. R Hughes. *Isogeometric Analysis: Toward Integration of CAD and FEA*. Wiley, 2009.

[122] I.H. Sloan. Polynomial interpolation and hyperinterpolation over general regions. *Journal of Approximation Theory*, 83(2):238–254, 1995.

[123] Kendall Atkinson and Weimin Han. *Spherical Harmonics and Approximations on the Unit Sphere: An Introduction*. Springer, 2010.

[124] Robert S. Womersley and Ian H. Sloan. How good can polynomial interpolation on the sphere be? *Advances in Computational Mathematics*, 14(3):195–226, 2001.

[125] Ian H. Sloan and Robert S. Womersley. Constructive polynomial approximation on the sphere. *Journal of Approximation Theory*, 103(1):91–118, 2000.

[126] Manfred Reimer. Hyperinterpolation on the sphere at the minimal projection order. *Journal of Approximation Theory*, 104(2):272–286, 2000.

[127] Congpei An, Xiaojun Chen, Ian H. Sloan, and Robert S. Womersley. Regularized least squares approximations on the sphere using spherical designs. *SIAM Journal on Numerical Analysis*, 50(3):1513–1534, 2012.

[128] Nathanaël Schaeffer. Efficient spherical harmonic transforms aimed at pseudospectral numerical simulations. *Geochem. Geophys. Geosyst.*, 14(3):751–758, 2013.

[129] D.M. Healy, D.N. Rockmore, P.J. Kostelec, and S. Moore. Ffts for the2-sphere-improvements andvariations. *Journal of Fourier Analysis and Applications*, 9(4):341–385, 2003.

[130] J.R. Driscoll and D.M. Healy. Computing fourier transforms and convolutions on the 2-sphere. *Advances in Applied Mathematics*, 15(2):202–250, June 1994.

[131] Casper H. L. Beentjes. Quadrature on spherical surface. *Technical Report*, 2015.

[132] Robert S. Womersley. Efficient spherical designs with good geometric properties. *arXiv:1709.01624*, 2017.

[133] L. N. Trefethen and D. Bau. *Numerical Linear Algebra*. Society for Industrial and Applied Mathematics, 1997.

[134] G. Strang. *Linear Algebra and Its Applications*. Academic Press, Inc., 1980.

[135] Stefan Kunis and Daniel Potts. Fast spherical fourier algorithms. *Journal of Computational and Applied Mathematics*, 161(1):75–98, December 2003.

[136] Kerstin Hesse, Ian H. Sloan, and Robert S. Womersley. *Numerical Integration on the Sphere*, pages 1185–1219. Springer Berlin Heidelberg, Berlin, Heidelberg, 2010.

[137] Atkinson Kendall. Numerical integration on the sphere. *J. Austral. Math. Soc.*, (Series B) 23:332–347, 1982.

[138] J. J. Thomson. Xxiv. on the structure of the atom: an investigation of the stability and periods of oscillation of a number of corpuscles arranged at equal intervals around the circumference of a circle; with application of the results to the theory of atomic structure. *The London, Edinburgh, and Dublin Philosophical Magazine and Journal of Science*, 7(39):237–265, March 1904.

[139] Mamdouh S. Mohamed, Anil N. Hirani, and Ravi Samtaney. Comparison of discrete hodge star operators for surfaces. *Comput. Aided Des.*, 78(C):118–125, September 2016.

[140] Anil N. Hirani, Kaushik Kalyanaraman, and Evan B. VanderZee. Delaunay hodge star. *Computer-Aided Design*, 45(2):540 – 544, 2013. Solid and Physical Modeling 2012.

[141] Scott Ridgway Brenner, Susanne. *The Mathematical Theory of Finite Element Methods*. Springer, 2008.

[142] T. M. Shih. A procedure to debug computer programs. *International Journal for Numerical Methods in Engineering*, 21(6):1027–1037, 1985.

[143] K. Salari and P. Knupp. Code verification by the method of manufactured solutions. Technical Report SAND2000-1444, Sandia National Laboratories, 2000.

[144] Aaron Meurer, Christopher P. Smith, Mateusz Paprocki, Ondřej Čertík, Sergey B. Kirpichev, Matthew Rocklin, AMiT Kumar, Sergiu Ivanov, Jason K. Moore, Sartaj Singh, Thilina Rathnayake, Sean Vig, Brian E. Granger, Richard P. Muller, Francesco Bonazzi, Harsh Gupta, Shivam Vats, Fredrik Johansson, Fabian Pedregosa, Matthew J. Curry, Andy R. Terrel, Štěpán Roučka, Ashutosh Saboo, Isuru Fernando, Sumith Kulal, Robert Cimrman, and Anthony Scopatz. Sympy: symbolic computing in python. *PeerJ Computer Science*, 3:e103, January 2017.

[145] C. S. Peskin. The immersed boundary method. *Acta Numerica*, 11:479–517, 2002.

[146] Paul J. Atzberger. Stochastic eulerian lagrangian methods for fluid–structure interactions with thermal fluctuations. *Journal of Computational Physics*, 230(8):2821–2837, April 2011.

[147] P. J. Atzberger, P. R. Kramer, and C. S. Peskin. A stochastic immersed boundary method for fluid-structure dynamics at microscopic length scales. *Journal of Computational Physics*, 224(2):1255–1292–, 2007.

[148] Y. Wang, J. K. Sigurdsson, and P. J. Atzberger. Fluctuating hydrodynamics methods for dynamic coarse-grained implicit-solvent simulations in lammps. *SIAM Journal on Scientific Computing*, 38(5):S62–S77, 2016.

[149] H. von Helmholtz. Zur theorie der stationaren strome in reibenden flussigkeiten (the theory of stationary currents in shearing liquids). *Verh. Naturh.-Med. Ver. Heidelb,*, 11(223), 1868.

[150] I. M. Gelfand and S. V. Fomin. *Calculus of Variations*. Dover, 2000.

[151] P. Alliez, D. Cohen-Steiner, Y. Tong, and M. Desbrun. Voronoi-based variational reconstruction of unoriented point sets. In *Proceedings of the Fifth Eurographics Symposium on Geometry Processing*, SGP '07, pages 39–48, Aire-la-Ville, Switzerland, Switzerland, 2007. Eurographics Association.

[152] G. Monge. Application de l'analyse à la géométrie. 1807.

[153] Lawrence C Evans. Partial differential equations. second. vol. 19. *Graduate Studies in Mathematics. American Mathematical Society, Providence, RI*, 2010.

[154] Eric Bavier, Mark Hoemmen, Sivasankaran Rajamanickam, and Heidi Thornquist. Amesos2 and belos: Direct and iterative solvers for large sparse linear systems. *Scientific Programming*, 20(3), 2012.

[155] Andrey Prokopenko, Jonathan J. Hu, Tobias A. Wiesner, Christopher M. Siefert, and Raymond S. Tuminaro. MueLu user's guide 1.0. Technical Report SAND2014-18874, Sandia National Labs, 2014.

[156] Jonathan J. Hu, Andrey Prokopenko, Christopher M. Siefert, Raymond S. Tuminaro, and Tobias A. Wiesner. MueLu multigrid framework. `http://trilinos.org/packages/muelu`, 2014.

[157] Michael A. Heroux, Roscoe A. Bartlett, Vicki E. Howle, Robert J. Hoekstra, Jonathan J. Hu, Tamara G. Kolda, Richard B. Lehoucq, Kevin R. Long, Roger P. Pawlowski, Eric T. Phipps, Andrew G. Salinger, Heidi K. Thornquist, Ray S. Tuminaro, James M. Willenbring, Alan Williams, and Kendall S. Stanley. An overview of the trilinos project. *ACM Trans. Math. Softw.*, 31(3):397–423, September 2005.

[158] Per-Olof Persson and Gilbert Strang. A simple mesh generator in matlab. *SIAM Review*, 46(2):329–345, 2004.